INVESTIGATING IMPACT OF DESIGN MODIFICATIONS ON THE PERFORMANCE OF A SAVONIUS HYDROKINETIC TURBINE AT LOW SPEEDS

A THESIS SUBMITTED TO
THE GRADUATE SCHOOL OF NATURAL AND APPLIED SCIENCES
OF
MIDDLE EAST TECHNICAL UNIVERSITY

BY

DOĞA DERMAN ÇİÇEK

IN PARTIAL FULFILLMENT OF THE REQUIREMENTS
FOR
THE DEGREE OF MASTER OF SCIENCE
IN
CIVIL ENGINEERING

JANUARY 2024

Approval of the thesis:

INVESTIGATING IMPACT OF DESIGN MODIFICATIONS ON THE PERFORMANCE OF A SAVONIUS HYDROKINETIC TURBINE AT LOW SPEEDS

submitted by **DOĞA DERMAN ÇİÇEK** in partial fulfillment of the requirements for the degree of Master of Science in Civil Engineering, **Middle East Technical University** by,

Prof. Dr. Halil Kalıpçılar
Dean, **Graduate School of Natural and Applied Sciences** _____

Prof. Dr. Erdem Canbay
Head of the Department, **Civil Engineering** _____

Assoc. Prof. Dr. Elif Oğuz
Supervisor, **Civil Engineering, METU** _____

Assoc. Prof. Dr. Ng Cheng Yee
Co-Supervisor, **Civil Engineering,**
PETRONAS University of Technology (UTP) _____

Examining Committee Members:

Prof. Dr. A. Burcu Altan-Sakarya
Civil Engineering, METU _____

Assoc. Prof. Dr. Elif Oğuz
Civil Engineering, METU _____

Prof. Dr. Mete Köken
Civil Engineering, METU _____

Assoc. Prof. Dr. Nilay Sezer-Uzol
Aerospace Engineering, METU _____

Assist. Prof. Dr. Mehmet Adil Akgül
Civil Engineering, Turkish-German University _____

Date: 24.01.2024

I hereby declare that all information in this document has been obtained and presented in accordance with academic rules and ethical conduct. I also declare that, as required by these rules and conduct, I have fully cited and referenced all material and results that are not original to this work.

Name Last name :Çiçek, Doğa Derman

Signature :

ABSTRACT

INVESTIGATING IMPACT OF DESIGN MODIFICATIONS ON THE PERFORMANCE OF A SAVONIUS HYDROKINETIC TURBINE AT LOW SPEEDS

Çiçek, Doğa Derman
Master of Science, Civil Engineering
Supervisor: Assoc. Prof. Dr. Elif Oğuz
Co-Supervisor: Assoc. Prof. Dr. Ng Cheng Yee

January 2024, 159 pages

In recent decades, the global demand for energy has surged due to technological advancements and industrial expansion, resulting in a notable increase in greenhouse gas levels from increased fossil fuel consumption. To address these challenges, developed nations and academia are allocating more resources to projects exploring the efficient utilization of renewable energy. Hydroelectric power stands out due to its high energy density and predictability. Academic interest in harnessing current energy has grown, emphasizing water's superior energy potential compared to air. Hydrokinetic turbines offer a preferable alternative in scenarios where dam construction is impractical or unfavorable, as they eliminate the need for a reservoir. Turkey, surrounded by seas and abundant water sources, should investigate harnessing energy from its irrigation channels, rivers and currents. As the majority of Turkey's currents are slow, conventional hydrokinetic turbines with propeller blades struggle to operate efficiently. This thesis aims to address this challenge by investigating a horizontal-axis Savonius-type hydrokinetic turbine which, is specifically more efficient for slow channel streams than hydrokinetic turbines having propeller blades. The study employs numerical modeling and simulation programs to analyze the turbine's performance. The simulations are carried out by

using Ansys Fluent software. The research invetigates the impact of various design modifications, such as multi-stage configurations, turbine aspect ratio, and the adoption of twisted/helical blades, on the horizontal-axis Savonius hydrokinetic turbine's (SHT) efficiency.

Keywords: Savonius Hydrokinetic Turbine, Multi-stage Configurations, Aspect Ratio, Twisted/Helical Blades, Horizontal Axis

ÖZ

DÜŞÜK AKIŞ HIZLARINDA TASARIM MODİFİKASYONLARININ SAVONIUS HİDROKİNETİK TÜRBİNİN PERFORMANSINA ETKİSİNİN İNCELENMESİ

Çiçek, Doğa Derman
Yüksek Lisans, İnşaat Mühendisliği
Tez Yöneticisi: Doç. Dr. Elif Oğuz
Ortak Tez Yöneticisi: Doç. Dr. Ng Cheng Yee

Ocak 2024, 159 sayfa

Teknolojik gelişmeler ve endüstriyel genişleme nedeniyle küresel enerji talebi sol yıllarda artmıştır. Artan enerji talebi fosil yakıtlardan karşılanmıştır, bu durum sera gazı seviyelerinde dikkate değer bir artışa yol açmıştır. Bu artışla mücadele etmek için gelişmiş ülkeler ve akademik çevreler yenilenebilir enerjinin kullanımını arttırmayı amaçlayan projelere daha fazla ilgi göstermeye başlamıştır. Yenilenebilir enerji kaynakları arasında hidroelektrik yüksek enerji yoğunluğu ve öngörülebilirliğiyle ön plana çıkmaktadır. Hidrokinetik türbinler, baraj inşasının pratik olmadığı veya uygun olmadığı senaryolarda tercih edilebilir bir alternatif sunar, çünkü rezervuar inşası ihtiyacını ortadan kaldırırlar. Türkiye'nin çevresinin denizlerle çevrili olduğu ve sahip olduğu akarsu kaynakları göz ününe alındığında sulama kanallarından, nehirlerden ve deniz akıntılarından hidrokinetik enerji elde edilmesine yönelik araştırmalar yürütülmelidir. Türkiye'nin çoğunlukla yavaş akan akıntılara sahip olması, konvansiyonel hidrokinetik türbinlerin pervane bıçaklarıyla verimli bir şekilde çalışmasını zorlaştırmaktadır. Bu tezde yatay eksende

yerleştirilmiş Savonius tipi bir hidrokinetik türbin yavaş akıntı hızında test edilecektir. Çalışma, türbinin performansını analiz etmek için sayısal modelleme ve simülasyon programlarını kullanmaktadır. Simülasyonlar, Ansys Fluent yazılımı kullanılarak gerçekleştirilmektedir. Araştırma, çeşitli tasarım değişikliklerinin (çok aşamalı konfigürasyonların, türbin en-boy oranının ve eğri kanatların eklenmesinin) yatay eksende yerleştirilen Savonius hidrokinetik türbinin (SHT) verimliliği üzerindeki etkilerini inceleyerek türbin performansını artırmayı hedeflemektedir.

Anahtar Kelimeler: Savonius Hidrokinetik Türbin, Çok Aşamalı Tasarım, Türbin En/Boy Oranı, Eğri/Sarmal Kanat, Yatay Eksen

Dedication

ACKNOWLEDGMENTS

I owe a profound debt of gratitude to Assoc. Prof. Dr. Elif Oğuz, whose impact on my academic journey has been transformative. Assoc. Prof. Dr. Elif Oğuz played a pivotal role in introducing me to the academic world during my undergraduate studies. Our paths crossed when I participated in a undergraduate research program (CE STAR) under Assoc. Prof. Dr. Elif Oğuz 's supervision, an experience that proved to be truly life-changing. Under her guidance, I delved into the intricacies of academic research, broadening my understanding and sparking a passion for scholarly inquiry. It was through Dr. Oğuz's mentorship that I not only gained valuable research skills but also developed a profound appreciation for the rigors and rewards of academic exploration. Her commitment to fostering intellectual curiosity and academic excellence laid the foundation for my continued journey in academia. I am forever grateful to Dr. Elif Oğuz for opening the door to the academic realm and for being a mentor whose influence extends far beyond the boundaries of a classroom. This thesis stands as a testament to the profound impact of her guidance on my academic growth and aspirations.

In the pursuit of this academic milestone, I am profoundly grateful to have the unwavering support and inspiration of my incredible girlfriend, Denizay Onol. Denizay has been my steadfast companion, providing endless encouragement, understanding, and patience throughout the entire journey of researching and writing this thesis. Her belief in my abilities and her genuine joy in my achievements have been a constant source of motivation. Her presence has infused warmth into the often solitary process of thesis work. To Denizay Onol, your unwavering support has made this academic endeavor not just a solitary pursuit but a shared triumph.

My heartfelt gratitude goes to the cornerstones of my life - my parents, Asker Çiçek and Öznur Çiçek. In the journey of completing this thesis, their unwavering support, boundless love, and enduring encouragement have been my constant companions.

Special appreciation is extended to my mother, Öznur Çiçek, a philosophy teacher, and my greatest supporter. Beyond being a loving parent, her wisdom and passion for learning have profoundly influenced my academic journey. Her role goes beyond the typical parent-child relationship, shaping not only this thesis but also my broader outlook on life.

I would like to present my special thanks and fellowship to my friends from METU Hydromechanics Engineering Division, Dr. Emre Haspolat, Dr. Serkan Gökmener, for all their support, kind friendship. Additionally, I want to express my appreciation to my office roommate, Berhan Melek, whose support and friendship have not only made the workplace more enjoyable but have also created a conducive atmosphere for productivity.

This study was supported by “Orta Doğu Teknik Üniversitesi (ODTÜ) Bilimsel Araştırma Projeleri (BAP) Koordinasyon Birimi”. (Project No. GAP-303-2022-10895).

TABLE OF CONTENTS

ABSTRACT v

ÖZ vii

ACKNOWLEDGMENTS x

TABLE OF CONTENTS xii

LIST OF TABLES xvi

LIST OF FIGURES xvii

LIST OF ABBREVIATIONS xxi

LIST OF SYMBOLS xxii

CHAPTERS

1 INTRODUCTION 1

1.1 Hydrokinetic Turbines 7

2 LITERATURE REVIEW 11

2.1 Design Principles and Working Mechanism of Savonius Turbines 12

2.2 Optimization Studies on The Savonius Hydrokinetic Turbines 14

2.2.1 Effect of Overlap Ratio and Gap Ratio on the Performance of the Savonius Hydrokinetic Turbines 15

2.2.2 Effect of Number of Blades on the Performance of the Savonius Hydrokinetic Turbine 16

2.3 Effect of Aspect Ratio on the Performance of Savonius Hydrokinetic Turbine … 18

2.3.1 Literature on Savonius Wind Turbines (SWT) 18

2.3.2 Literature on Savonius Hydrokinetic Turbine (SHT) 20
2.3.3 Summary of the Literature on Impact of AR on the Performance of Savonius Turbine 21
2.4 Effect of Multi-stage Configurations on the Performance of Savonius Hydrokinetic Turbine 24
2.4.1 Literature on Multi-stage Configurations of Savonius Hydrokinetic Turbine (SHT) 25
2.4.2 Literature on Multi-stage Configurations of Savonius Wind Turbine (SWT) …..... 28
2.4.3 Summary of Literature on Impact of Multi-stage Configurations on the Performance of Savonius Turbine 29
2.5 Effect of Adoptation of Twisted Blades on the Performance of SHTs 30
2.6 Numerical Modeling of the Savonius Turbines 33
2.6.1 The Flow Field around the Savonius Turbines 33
2.6.2 Literature Review on the Numerical Modeling of the Savonius Turbines …..... 35
3 METHODOLOGY 39
3.1 Introduction 39
3.2 Performance Evaluation Parameters 40
3.3 Governing Equations 42
3.3.1 Navier-Stokes Equations for Incompressible Flow 42
3.3.2 Reynolds-Averaged-Navier-Stokes (RANS) Equations for Incompressible Flow 42
3.4 Turbulence Model 44
3.4.1 SST k-ω Turbulence Model 45

3.5 Used Dynamic Mesh Model: Sliding Mesh Model 47
4 NUMERICAL SETUP 49
4.1 Experimental Work Carried Out By (Talukdar et al., 2018) 50
4.1.1 Experimental Setup 51
4.1.2 Design Parameters of the Two-Semicircular Bladed Turbine 52
4.2 Geometry Generation and Meshing 54
4.3 Obtaining Inlet Velocity Distribution 60
4.4 Numerical Model Development of Turbine Simulations 63
4.4.1 Mesh Independence Study 64
4.4.2 Time Step Independence Study 66
4.5 Validation of the Numerical Model of Turbine 68
5 TEST CASE DEFINITIONS 73
5.1 Test Cases: Aspect Ratio 74
5.2 Test Cases: Turbine Stacking 75
5.3 Test cases: Blade Twist Angle 76
6 RESULTS 79
6.1 Horizontal Orientation of Savonius Turbine 79
6.2 Performance Characteristics of the Horizontally Positioned Savonius Turbine … 82
6.2.1 Self-starting Characteristic of the Benchmark Model of Savonius Turbine … 82
6.2.2 Rotational Performance of the Benchmark Model 89
6.3 Evolution of the Flow Field 92
6.4 Results: Aspect Ratio 98

6.4.1 Performance Analysis of the AR Configurations 98
6.4.2 Evolution of Flow Field around AR Configurations 104
6.5 Results Multi-stage..... 113
6.5.1 Performance Analysis of Two-stage SHTs..... 114
6.5.2 Performance Analysis of Three-stage SHTs..... 120
6.5.3 Performance Comparison of Single-stage, Two-stage, Three-stage Turbines …..... 126
6.5.4 Evolution of the flow field around multistage turbines 129
6.6 Results: Helical Blades..... 138
6.6.1 Performance Analysis of Helical Blade Profiles 139
6.6.2 Evolution of the flow field around helical turbines 142
7 CONCLUSION.....149
REFERENCES 151

LIST OF TABLES

TABLES

Table 2.1 Summary of Experimental Studies on AR 22
Table 4.1 Design Parameters of Two-bladed Turbine (Talukdar et al., 2018)..... 53
Table 4.2 Generated Meshes 65
Table 4.3 Resulting C_T and C_P Values of the Meshes in Mesh Independence Study 65
Table 4.4 Resulting C_T Values of Time Step Independence Study 67
Table 4.5 Comparison of Numerical and Experimental Results 70
Table 5.1 Aspect Ratio Test Cases Turbine Specifications..... 74
Table 5.2 Two-stage Test Cases Turbine Specifications..... 76
Table 5.3 Three-stage Test Cases Turbine Specifications..... 76
Table 5.4 Blade Twist Angle Test Cases..... 77
Table 6.1 Comparison of Resulting C_T for the Alternative Placements of SHT 81
Table 6.2 Comparison of Resulting C_P for the Alternative Placements of SHT 81
Table 6.3 Comparison of Vertical Axis Turbine and Horizontal Axis Turbine, C_P 92

LIST OF FIGURES

FIGURES

Figure 1.1. Power Densities of Water Flow and Wind (Yuce & Muratoglu, 2015). 3
Figure 1.2. SeaFlow Project (2003) (at left), SeaGen S (2009) (at right), (Fundy, 2008) 4
Figure 1.3. Deployment of HGE's turbine (*Hydro Green Energy*, n.d.)..... 5
Figure 1.4. Waterotor's turbine design examples small size version and large size version (*Products | Waterotor Energy Technologies*, n.d.) 5
Figure 1.5. Axial-flow Turbines (Vermaak et al., 2014) 7
Figure 1.6. Cross-flow turbine designs (Vermaak et al., 2014)..... 8
Figure 2.1. Standard Savonius Turbine Design (Maldar et al., 2020) 12
Figure 2.2. Geometric Parameters of a Savonius turbine (Badrul Salleh et al., 2019; Maldar et al., 2020)..... 13
Figure 2.3. Studied SHTs in (Thiyagaraj et al., 2016)..... 17
Figure 2.4. Developed Design in Study of (Kumar & Saini, 2016a)..... 26
Figure 2.5. Investigated SHT variants in the study of (Kumar et al., 2020)..... 28
Figure 2.6. Flow visualization for a SWT at different azimuth angles (Murai et al., 2007) 34
Figure 4.1. Experimental Setup (Talukdar et al., 2018)..... 51
Figure 4.2. Open channel used in experiments and the used channel section (at left) by (Talukdar et al., 2018)..... 52
Figure 4.3. Two-bladed SHT Design (Talukdar et al., 2018) 53
Figure 4.4. CAD Model of the flume..... 54
Figure 4.5. Generated Mesh of the Channel 55
Figure 4.6. Generated Inflation Layer of the Channel..... 55
Figure 4.7. CAD Model of Rotational Domain 56
Figure 4.8. CAD Model of Static Domain..... 57
Figure 4.9. Generated Mesh of Rotational Domain..... 58
Figure 4.10. Inflation Layer around Shaft and Blades..... 59

Figure 4.11. Generated Mesh of the Static Domain 60
Figure 4.12. Generated Mesh of the Static Domain near Rotational Zone 60
Figure 4.13. Horizontal Velocity Component Distribution 61
Figure 4.14. Vertical Velocity Component Distribution 62
Figure 4.15. Mesh Independence Study 66
Figure 4.16. Time Step Independence Study 67
Figure 4.17. Boundary conditions of the numerical model 69
Figure 4.18. Comparison of C_T values 70
Figure 4.19. Comparison of C_P values 71
Figure 6.1. Alternative Horizontal Placement of SHT 80
Figure 6.2. Static Torque Analysis of the Horizontally Positioned SHT 83
Figure 6.3. Comparison of Static Torque Coefficients 84
Figure 6.4. Velocity Contours at Azimuth Angles of a) 135 and b) 150 86
Figure 6.5. Pressure contour at Azimuth Angles of a) 135 and b) 150 87
Figure 6.6. C_P Generation Curve of the Horizontally Positioned SHT 89
Figure 6.7. C_T Generation Curve of the Horizontally Positioned SHT 90
Figure 6.8. C_T Generation over a Single Rotation of the Horizontally Positioned SHT 91
Figure 6.9. Pressure contour (Top) and Velocity contour (Bottom) at 0° 93
Figure 6.10. Pressure contour (Top) and Velocity contour (Bottom) at 45° 94
Figure 6.11. Pressure contour (top) and Velocity contour (bottom) at 90° 96
Figure 6.12. Pressure contour (top) and Velocity contour (bottom) at 135° 97
Figure 6.13. C_T vs. TSR curve of the AR configurations 99
Figure 6.14. Highest C_{TS}s obtained by the AR configurations at 0.6 TSR 100
Figure 6.15. C_P vs TSR curve of the AR configurations 101
Figure 6.16. Highest C_{PS}s obtained by the AR configurations at 0.9 TSR 102
Figure 6.17. Torque generated by the AR configurations in a single rotation 103
Figure 6.18. Pressure contours at the mid-sections of AR1.2, AR1.4, AR1.6 and AR1.8 at TSR 0.6 106

Figure 6.19. Pressure contours and streamlines presented on horizontal section of AR1.0, AR1.2, AR1.4 and AR1.6 108
Figure 6.20. 3D streamlines presented near mid-sections of AR1.0 and AR1.6 .. 110
Figure 6.21. 3D streamlines presented at 10 cm away from the endplates of AR1.0 and AR1.6 112
Figure 6.22. C_T vs. TSR curves of two-stage configurations 115
Figure 6.23. C_T vs. phase difference angle curves of two-stage configurations ... 116
Figure 6.24. C_P vs. TSR curves of two-stage configurations 117
Figure 6.25. Highest C_{PS} obtained by the two-stage configurations at 0.9 TSR .. 118
Figure 6.26. Torque generated by the two-stage configurations in a single rotation 119
Figure 6.27. Standard deviation of torque generated by the two-stage configurations 120
Figure 6.28. C_T vs. TSR curves of the three-stage configurations 121
Figure 6.29. C_P vs. TSR curves of the three-stage configurations 122
Figure 6.30. Highest C_{PS} obtained by the three-stage configurations at 0.9 TSR 123
Figure 6.31. Torque generated by the three-stage configurations in a single rotation 124
Figure 6.32. Standard deviation of torque generated by the three-stage configurations 125
Figure 6.33. C_T vs. TSR curves of 1S-SHT-PD0°-AR1.0, 2S-SHT-PD90° and 3S-SHT-PD60° 126
Figure 6.34. C_P vs. TSR curves of 1S-SHT-PD0°-AR1.0, 2S-SHT-PD90° and 3S-SHT-PD60° 127
Figure 6.35. Torque generated by 1S-SHT-PD0°-AR1.0, 2S-SHT-PD90° and 3S-SHT-PD60° in a single rotation 128
Figure 6.36. Torque generated by 3S-SHT-PD60° and its stages in a single rotation 129
Figure 6.37. Pressure contours at mid-sections of 1S-SHT-PD0°-AR1.0, 1S-SHT-PD0°-AR2.85 and stages of 3S-SHT-PD60° at 20° and 110° of rotation 131

Figure 6.38. Pressure contours at mid-sections of 1S-SHT-PD0°-AR1.0, 1S-SHT-PD0°-AR1.9 and stages of 2S-SHT-PD90° at 20° and 110° of rotation 135
Figure 6.39. Pressure contours and streamlines in front of the advancing blades of 2S-SHT-PD90° and 3S-SHT-PD60° 137
Figure 6.40. C_T vs. TSR curves of HSHT configurations 139
Figure 6.41. C_T vs. blade twist angle curves of HSHT configurations 140
Figure 6.42. C_P vs. TSR curves of HSHT configurations 141
Figure 6.43. Torque generated by HSHT configurations over a single rotation ... 142
Figure 6.44. Pressure contours along the length of TWST0°, TWST45° and TWST90° at 20° of rotation 144
Figure 6.45. Pressure contours along the length of TWST0°, TWST45° and TWST90° at 120° of rotation 146
Figure 6.46. Pressure distribution over the blade surfaces of TWST0°, TWST45° and TWST90° at 90° of rotation..... 147
Figure 6.47. Velocity field over the blade surfaces of TWST0°, TWST45° and TWST90° at 90° of rotation 148

LIST OF ABBREVIATIONS

ABBREVIATIONS

AR : Aspect Ratio

CFD : Computational Fluid Dynamics

FDM : Finite Difference Method

FEM : Finite Element Method

FVM : Finite Volume Method

OR : Overlap Ratio

RANS : Reynolds-Averaged-Navier-Stokes

SHT : Savonius Hydrokinetic Turbine

SST : Shear Stress Transport

ST : Savonius Turbine

SWT : Savonius Wind Turbine

TSR : Tip Speed Ratio

LIST OF SYMBOLS

A_{ref}	: Reference Area of SHT
C_P	: Power Coefficient
C_T	: Torque Coefficient
D_T	: Turbine Diameter
g	: Gravitational Acceleration
H_T	: Turbine Height
k	: Turbulence Kinetic Energy
P	: Pressure
r	: Turbine Radius
Re	: Reynold's Number
t	: Time
T_{out}	: Output Torque
u_i	: Velocity Component
$\bar{u}_i$	: Time Averaged Component of Velocity Vector
u_i'	: Fluctuating Component of Velocity Vector
V_0	: Inflow Velocity
x_i	: Position Component in Cartesian Coordinate System
μ	: Dynamic Viscosity
ρ	: Density of Working Fluid
ω	: Specific Rate of Dissipation of k
ω_0	: Angular Velocity of SHT (rad/sec)

CHAPTER 1

INTRODUCTION

Over time, the need for energy has grown as a result of industrialization and technological advances. As of 2018, according to International Energy Agency (IEA) worldwide electricity demand has experienced a significant increase of 75% compared to the year 2000. Furthermore, it is projected to continue to increase by an additional 58% by the year 2040(IEA, 2019). The increase in energy demand has been met by the increase in utilization of fossil fuels without considering the long-term sustainability of this practice. According to International Panel on Climate Change Climate 2014 Report, the utilization of fossil fuels has led to a significant rise in the concentrations of CO_2, CH_4, and NO_x gases in the atmosphere, with an approximate increase of 40%, 150%, and 20% correspondingly, compared to pre-industrial revolution values (IPCC, 2014). Due to the increase in greenhouse gases (GHGs) levels in the atmosphere, the world surface temperature had a 1.09 °C increase in the period of 2011-2020 compared to the period of 1850-1900 (IPCC, 2023). The temperature rise over land was 1.59 °C, which is higher than the increase over the ocean, which was 0.88 °C (IPCC, 2023). In Turkey, GHG emissions also have consistently increased over the years. Between 2000 and 2013, Turkey's GHG emissions showed a growth of 47.7% (Şahin et al., 2019) and between 2013 and 2021, Turkey's GHG emissions show an increase of 28.2%(TUİK, 2023). Moreover, the per capita total greenhouse gas emissions in Turkey were estimated at 4 tons of CO_2 equivalent in 1990, 6.3 tons of CO_2 equivalent in 2020, and 6.7 tons of CO_2 equivalent in 2021 (TUİK, 2023). According to the findings of IPCC, if the current trend of increasing GHG emissions persists, Turkey is expected to see a rise in annual average temperatures ranging from +2.5 to +4 degrees Celsius by the year 2070(IPCC, 2014; Şahin et al., 2019).

The world has shifted its focus towards renewable energy sources to reduce the use of fossil fuels and mitigate their harmful effects. In line with these global developments, Turkey should follow suit, promoting the widespread adoption of renewable energy sources to protect against the destructive impact of climate change.

Hydropower stands out when compared to other renewable energy sources because of the fact that 75% of the Earth's surface is covered by water, making it more abundant and predictable (Kougias et al., 2019). Hydroelectric applications can be divided into two main categories: hydrostatic and hydrokinetic applications. In hydrostatic applications, electricity is produced by harnessing the potential energy difference between the constructed reservoir and the installed turbines. On the other hand, in hydrokinetic applications, the kinetic energy carried by flowing water is converted into electricity by turbines. Hydrokinetic turbine applications require less space since they do not necessitate the construction of dams, and their intervention in the natural flow of channels is comparatively minimal. Therefore, the adverse environmental effects they pose are relatively limited.

The abundantly available hydrokinetic power potential around the world represents the least utilized and most extensively available renewable energy resource. The energy concentration of hydrokinetic resources is much higher than that of wind because water is approximately 800 times denser than air as shown in Figure 1.1. Moreover, tidal regimes, ocean currents and river currents are more predictable than wind regimes and are continuously available compared to solar energy. Therefore, the utilization of hydrokinetic power is a key solution for overcoming climate crises. Researchers and government agencies have investigated the potential of hydrokinetic power. According to (Ridgill et al., 2021, 2022), the global riverine hydrokinetic resource is estimated to contain 1.642±0.003 TWh of energy. The United States (US) Department of Energy (DOE) also sponsored a series of resource estimation studies to analyze the countrywide potential of hydrokinetic energy. It was reported that the theoretical wave energy potential, tidal current energy potential, ocean current energy potential and river current energy potential are estimated as 1594-2640 TWh/year, 445 TWh/year, 200 TWh/year and 1381 TWh/year, respectively. The

total theoretical hydrokinetic energy resource is estimated to be 3620-4666 TWh/year. The extractable technical resource is determined as 1285 – 1846 TWh/year, which corresponds to 31.6-45.2% of the annual energy production of the US (U.S Department of Energy, 2015).

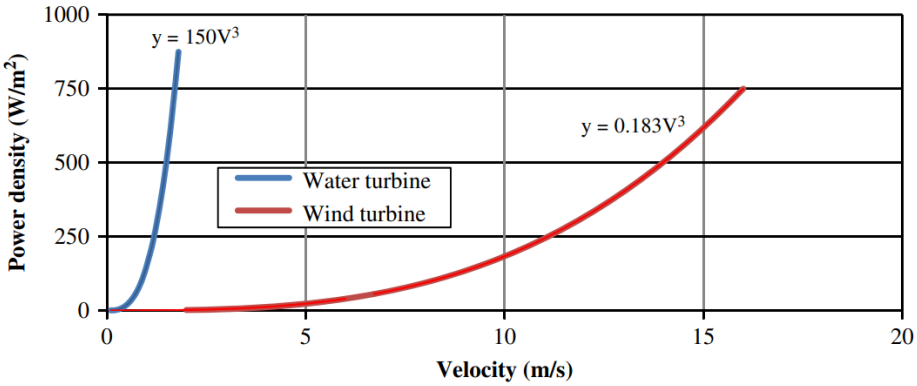


Figure 1.1. Power Densities of Water Flow and Wind (Yuce & Muratoglu, 2015)

Governments and companies, particularly those in coastal regions with strong tidal currents and ocean waves, took preliminary steps toward harnessing the potential of hydrokinetic resources in the early 2000s. Several prototypes were tested during the early 2000s. The prototype marine current turbine SeaGen SeaFlow was deployed off the coast of Lynmonth, United Kingdom, in 2003 by Marine Current Turbines, Ltd. Following the success of the prototype, Marine Current Turbines Ltd. installed the world's first commercial-scale grid-connected tidal current turbine, SeaGen S (Douglas et al., 2008). Both Seagen S and SeaFlow are shown Figure 1.2.



Figure 1.2. SeaFlow Project (2003) (at left), SeaGen S (2009) (at right), (Fundy, 2008)

In 2009, the Hydro Green Energy (HGE) company installed the first US-licensed commercial, grid-connected hydrokinetic project on the Mississippi River. The company placed two 100 kW rotor blade turbines, as shown in Figure 1.3, downstream of an existing run-of-river type conventional hydropower plant. The turbines are designed and optimized for yielding energy from slow river currents where the flow velocities downstream of the conventional hydropower plant vary between 1-3.5 m/s. After a successful demonstration of the effectiveness of this system, HGE obtained a license to developing a 5.25 MW plant downstream of Braddock Dam, Pennsylvania. In addition, the company currently obtains 11 preliminary licenses for other dams across the US (*Hydro Green Energy*, n.d.; POWERMAG, 2009)



Figure 1.3. Deployment of HGE's turbine (*Hydro Green Energy*, n.d.)

The Waterotor company is developing crossflow hydrokinetic turbines to address the problems associated with axial turbines. The company has developed a number of turbines having different sizes that mainly use the drag force exerted on the blades. The latest turbine of the company was tested, and a power coefficient of 55% was achieved. Moreover, the developed design can harness energy from water currents at a speed as low as 0.9 m/s (*Products | Waterotor Energy Technologies*, n.d.). The turbine developed by Waterotor is shown in Figure 1.4.



Figure 1.4. Waterotor's turbine design examples small size version and large size version (*Products | Waterotor Energy Technologies*, n.d.)

The given examples present a few developed hydrokinetic turbine designs, but they show the adaptivity and scalability of the hydrokinetic turbine technology. This technology can provide a solution for rural regions with small-scale applications on rivers and irrigation channels, such as Waterotor's solutions, and can also yield higher energy generation for cities, such as applications similar to HGE and Marine Currents Turbine Ltd. Several other devices are also tested and deployed such as Sabella D03, Clean Current Turbine, Hammerfest Strom (HS1000), Atlantis Resource (AR 1000), DCNS-OpenHydro turbin, Voith Hydro HyTide turbine, ORPC OCGen®, Scotrenewables tidal turbine (Maldar et al., 2022; Zhou et al., 2017).

In 2022, 34.6% of Turkey's electricity production was obtained from coal, 22.2% from natural gas, 20.6% from hydro energy, 10.8% from wind, 4.7% from solar, 3.3% from geothermal energy, and 3.7% from other sources (T.C. Enerji ve Tabii Kaynaklar Bakanlığı, 2023). A total of 56.8% of Turkey's annual energy production is obtained from fossil fuels which are mainly imported from other countries. Dependency on imported fossil fuels negatively impacts Turkey's economy. Considering recent geopolitical developments, the importance of energy independence for sovereign countries has been underlined. Further utilization of renewable energy resources will help Turkey to consolidate its energy independence. Turkey has generated 39.6% of its energy from renewable sources, half of which came from hydropower in 2022. This demonstrates the importance of hydropower production in the national energy grid. Turkey can improve and increase both the capacity and capabilities of existing hydropower plants without building new dams by developing similar solutions such as the HGE system to harness hydrokinetic energy downstream of these plants. Although there is no available country-wide estimation of hydrokinetic energy potential, Turkey is expected to have high hydrokinetic potential since it has an 8483 km shoreline (Simav & Şeker, 2013) and the annual runoff on Turkey's river is estimated to be 183 billion m^3 according to (*Devlet Su İşleri Genel Müdürlüğü*, n.d.).

1.1 Hydrokinetic Turbines

Hydrokinetic turbines can be broadly classified into axial-flow turbines and cross-flow turbines. For axial-flow turbines, the rotor axis is parallel to flow direction. Axial-flow turbines are illustrated in Figure 1.5 with various mooring configurations. Also, some commercial examples of axial-flow hydrokinetic turbines are presented in Figure 1.2 and Figure 1.3.

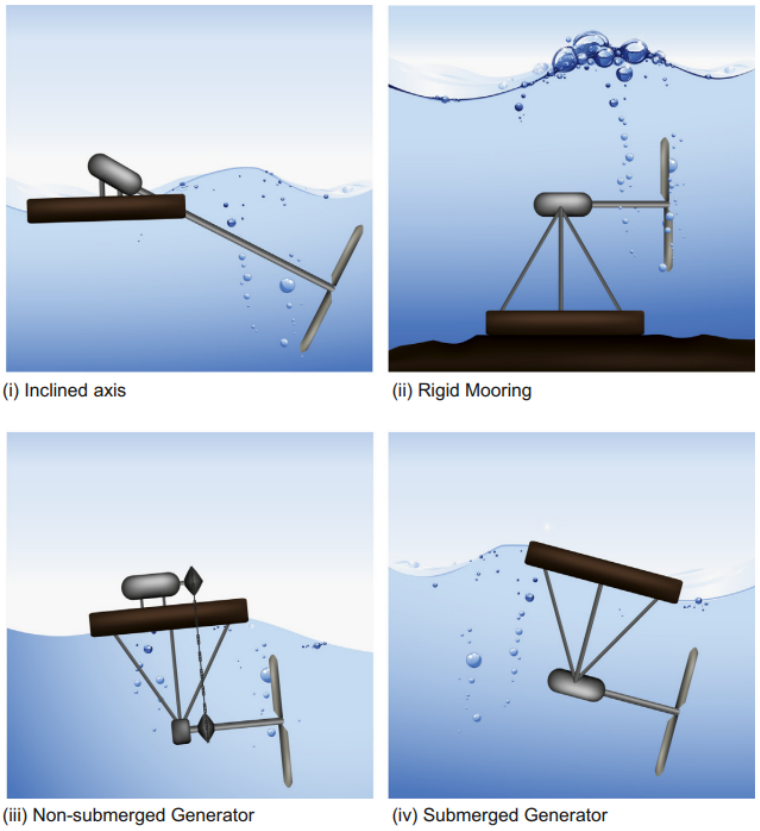


Figure 1.5. Axial-flow Turbines (Vermaak et al., 2014)

The axial-flow turbine blades are formed like propeller blades and resemble airfoil sections. This design enables the blades to produce lift as the fluid flows over airfoil profile, similar to how airplane wings generate lift in the air. These types of turbines

can be efficiently and economically utilized in waters deeper than 2000 m, where the speed exceeds 2 m/s (Rahimian et al., 2018; Subhra Mukherji et al., 2011).

For cross-flow turbines, the rotor axis is perpendicular to flow directions. The cross-flows turbines can further be classified into vertical-axis turbines and horizontal-axis (in-plane axis) turbines. The vertical-axis cross-flow turbines have a rotational axis perpendicular to the free surface whereas, the horizontal-axis turbines have a rotational axis parallel to the free surface. Various cross-flow turbine designs are presented in Figure 1.6. A commercial version of the cross-flow hydrokinetic turbine is also illustrated in Figure 1.4.

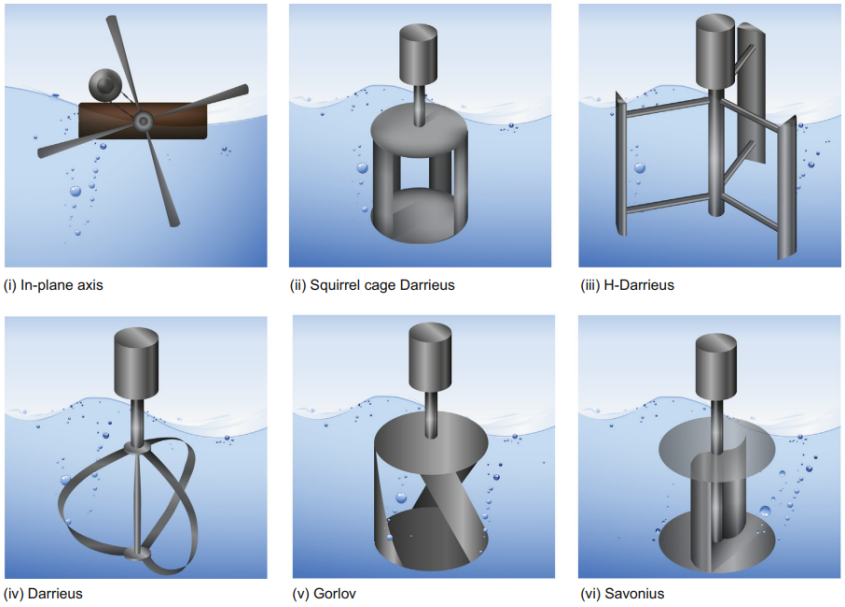


Figure 1.6. Cross-flow turbine designs (Vermaak et al., 2014)

Compared to axial-flow turbines, the cross-flow turbines have employed a wide range of different designs as shown in Figure 1.6. The blades of cross-flow turbines can utilize lift force or drag force depending on the design. The Darrieus type and Gorlov type cross-flow turbines are lift-based configurations while, the Savonius type is a drag-based configuration of cross-flow turbines.

This thesis focuses on a Savonius type hydrokinetic turbine, a distinct variant of cross-flow hydrokinetic turbines. It specifically addresses applications in both riverine and artificial channel settings, where slow and shallow water flows predominate. Whether in natural rivers or artificial channels, the unidirectional flow presents an advantageous scenario for the horizontal-axis placement of Savonius Turbines (STs). This orientation, leveraging the width of the channel, aims to enhance the turbine's sweep area by elongating it, a design strategy not practically feasible with the commonly employed vertical alignment in shallow water flows. Notably, the only commercially scaled horizontally aligned cross-flow turbine designed for channel flows is the turbine by Waterotor Energy Technologies, as shown in Figure 1.4.

The subsequent chapter will undertake a comprehensive literature review, concentrating on optimization studies relevant to Savonius Hydrokinetic Turbines (SHTs). It will also represent the design intricacies and operational principles inherent to Savonius turbines to establish a groundwork for understanding the interactions between fluid flows and SHTs.

Following the introduction, the methodology employed in this thesis will be introduced in Section 3, encompassing the governing equations of the utilized CFD simulations. Subsequently, a detailed presentation of the numerical model development will be provided in Section 4. The ensuing sections will present and discuss the findings of the thesis in detail.

CHAPTER 2

LITERATURE REVIEW

This chapter presents the literature review on Savonius Hydrokinetic Turbines (SHTs). The aim of the literature review is to conduct a comprehensive study of the prior research and advancements in the subject of Savonius Turbines (STs) with special focus on hydrokinetic applications.

In this thesis, several key design factors concerning SHTs will be numerically investigated. These key design factors include the aspect ratio (AR) of SHTs, multi-stage configurations of SHTs, and the adaptation of twisted blades in SHTs. Existing literature on each of these design factors will be thoroughly investigated in the following sections within this chapter.

The sections start with an introduction to the conventional ST design and the underlying working principles of STs. Subsequently, the inherent benefits and drawbacks of STs will be presented to establish a foundational understanding.

The literature review adopts a dual approach. Firstly, a thorough literature review, with a focus on hydrokinetic applications, will present the effects of optimization parameters that are different from the specific design factors discussed in this thesis. Secondly, the subsequent sections will provide an in-depth review of the existing literature, considering both wind and hydrokinetic applications, specifically focusing on each of the design factors: aspect ratio, multi-stage configurations, and the adaptation of twisted blades. Each of these design factors will be given dedicated subsections to facilitate a detailed analysis and synthesis of insights from both application field of STs. Lastly, the literature related to numerical modeling of the STs will be presented considering appropriate choice of turbulence model and numerical discretization method.

2.1 Design Principles and Working Mechanism of Savonius Turbines

The standard ST is designed by Sigurd Johannes Savonius in 1920s to harness energy from wind flow (Savonius et al., 1931). Basic design of a ST is illustrated in Figure 2.1.

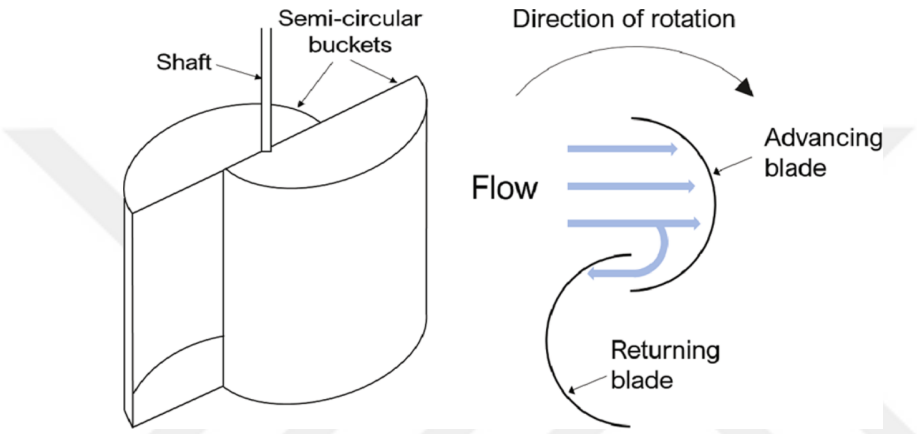
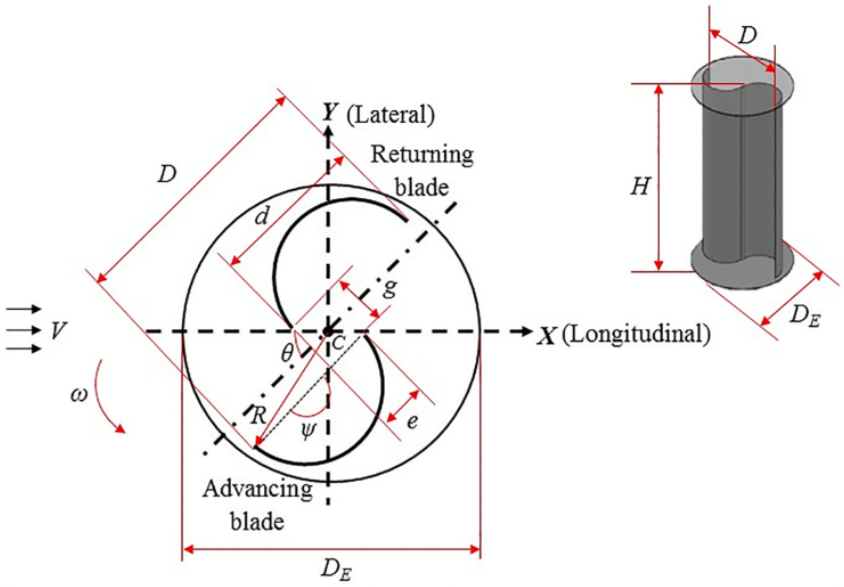


Figure 2.1. Standard Savonius Turbine Design (Maldar et al., 2020)

As seen in Figure 2.1, a ST basically consists of two semi-circular buckets facing each other attached to opposite sides of the central shaft. Due to the simple geometry of semicircular blades, the fabrication process of a ST is less complex compared to the lift-based turbines consisting of propeller type blades. Geometrical parameters of the ST design are illustrated in Figure 2.2.



C	Center of turbine	V	Freestream velocity (m/s)
D	Diameter of turbine (m)	θ	Turbine rotor angle (°)
D_E	End plate diameter (m)	ω	Angular velocity of turbine (rad/s)
d	Diameter of blade (m)	ψ	Blade arc angle (°)
e	Overlap distance (m)	AR	Aspect ratio [H/D]
g	Gap distance (m)	ER	End plate ratio [D_E/D]
H	Height of turbine (m)	GR	Gap ratio [g/d]
R	Radius of turbine (m)	OR	Overlap ratio [e/d]

Figure 2.2. Geometric Parameters of a Savonius turbine (Badrul Salleh et al., 2019; Maldar et al., 2020)

The working mechanism of a ST relies on the variation of drag force between advancing blade and returning blade and the variation of pressure difference between concave side and convex side of blades. The term "advancing blade" refers to a blade with its concave side oriented toward the incoming flow, while a "returning blade" is characterized by its convex side facing the flow as shown in Figure 2.1. The incoming flow hits both the concave side of the advancing blade and the convex side of the returning blade. As a result, a positive torque generated by advancing blade and a negative torque generated by the returning blade. The drag coefficient of the convex side is lower than of the concave side; therefore, the turbine experiences net positive torque which enables the rotation of ST.

The STs have several benefits including simple design, easy manufacturing and low noise emission during operation phase (Badrul Salleh et al., 2019; Kumar & Saini, 2016c; Maldar et al., 2020; Yadav et al., 2023). Moreover, STs exhibit a better starting characteristic in terms of initial torque at low speeds compared to lift-based turbines(Kumar & Saini, 2016c; Maldar et al., 2020; Modi & Fernando, 1989; Yadav et al., 2023). On the other hand, the major drawbacks of the ST design are poor efficiency and large torque fluctuations during power generation compared to axial-flow turbines (Badrul Salleh et al., 2019; Kumar & Saini, 2016c; Maldar et al., 2020).

2.2 Optimization Studies on The Savonius Hydrokinetic Turbines

The optimization studies for Savonius Hydrokinetic Turbines (SHTs) predominantly revolve around the geometric parameters presented in Figure 2.2. These efforts are specifically aimed at overcoming the inherent limitations observed in traditional Savonius Turbine (ST) designs. This section is dedicated specifically to the hydrokinetic applications of STs. Notably, this thesis will separately introduce optimization studies related to aspect ratio (AR) of SHTs, multi-stage configurations of SHTs, and the incorporation of twisted blades in SHTs. Each of these aspects will be addressed in dedicated sections, providing a focused exploration of their individual impacts on turbine performance. Therefore, this section will elaborate on optimization parameters distinct from those linked to Aspect Ratio (AR), multi-stage configurations, and twisted blades. The subsequent subsections will present the literature discussing the impact of the overlap ratio (OR), gap ratio (GR), and the number of blades in SHTs on their performances.

2.2.1 Effect of Overlap Ratio and Gap Ratio on the Performance of the Savonius Hydrokinetic Turbines

This section investigates the impact of overlap ratio and gap ratio on the performance of SHTs. Both the overlap ratio and the gap ratio define the amount of space between the inner tips of the blades in SHTs, which significantly influences its performance. The overlap ratio is defined as the proportion of overlapping distance between inner tips of the blades to the diameter of the turbine as shown in Figure 2.2. On the other hand, the overlap ratio is described as the ratio of amount of gap between inner turbine tips to the diameter of the turbine as also presented in Figure 2.2.

As described in Section 2.1, when the incoming flow strikes the convex side of the returning blade, negative torque is generated by the returning blade. This negative torque arises from the pressure difference between the convex side and the concave side of the returning blade. A higher-pressure zone occurs over the convex side of the returning blade while, a significantly lower-pressure zone occurs concave side of the returning blade since this side is shielded from water flow. The existence of a gap or overlapping distance between blades creates a gateway. This gateway enables the redirection of a portion of the incoming flow from the concave side of the advancing blade towards the concave side of the returning blade as shown in Figure 2.1. This redirection reduces the pressure difference between the convex and concave sides of the returning blades. Consequently, the negative torque generated by the returning blades reduces, resulting in an improvement in SHT performance.

(Yaakob et al., 2010) conducted a numerical study to investigate the optimum OR for a two-stage SHT having 90° phase difference. The researchers investigated OR values ranging from 0.10 to 0.60. The findings show that the two-stage SHT achieved highest performance with an OR of 0.21. In a subsequent study, (Yaakob et al., 2013) employed the same two-stage SHT design to experimentally identify the optimal OR. In this study, OR values ranging from 0.1 to 0.3 are investigated. The results of this study confirmed earlier findings of the numerical study. Consequently, the studied two stage SHT exhibited the highest torque for 0.21 OR.

In a numerical study, (Yao et al., 2019) investigated the impact of OR on the efficiency of a SHT. The researcher tested OR values of 0, 0.15 and 0.30 for tip-speed-ratios (TSRs) ranging from 0.6 to 1.2. The finding shows that the SHT having an OR of 0.15 exhibits superior performance for all TSRs among the studied variations. The maximum power-coefficient (C_P) achieved at 0.15 OR is 18.8% and 22.1% higher than the maximum C_P attained at ORs of 0 and 0.30, respectively.

(Kerikous & Thévenin, 2020) carried out a comprehensive numerical study to optimize OR and AR of a SHT. The researchers used Star-CCM to conduct CFD simulations and the optimization process is performed by OPAL++ based on the obtained simulation results. The maximum power output is attained at OR of 0.161 and GR of 0.033. Notably, the optimized design achieved 8% higher C_P than the original design.

2.2.2 Effect of Number of Blades on the Performance of the Savonius Hydrokinetic Turbine

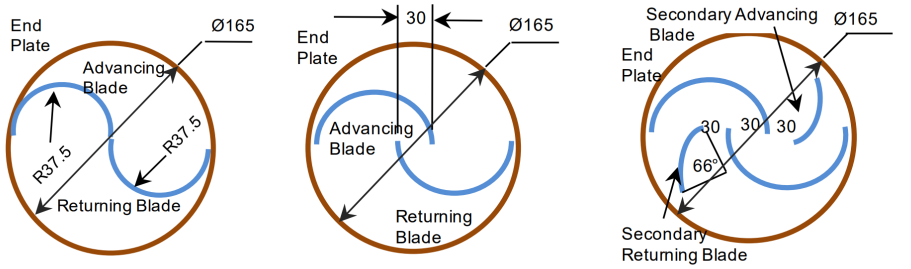
This section presents the studies focusing on the influence of number of blades adopted in SHTs on their performance.

The number of blades utilized in SHTs has a substantial impact on the efficiency of SHTs. The increase in number of blades can reduce the torque fluctuations experienced during the power generation process since higher blade count enhances the uniform spread of generated torque during rotation. However, the literature indicates that SHTs having two blades generally perform better compared to their counterparts having more blades than two.

(Yao et al., 2019) carried out a numerical study to compare the performances of SHTs having 2, 3 and 4 blades at TSR values ranging from 0.6 to 1.2. Among the studied turbines, the SHT having two blades demonstrated superior performance for all TSRs. The two-bladed SHT achieved maximum C_P of 0.228 at 0.9 TSR which is

57.2% and 178% more than the highest C_{PS} produced by three-bladed and four-bladed SHTs, respectively.

(Thiyagaraj et al., 2016) proposed a modified SHT having four blades which is consist of two primary blades and two secondary smaller blades. In an experimental study conducted by (Thiyagaraj et al., 2016), the performance of proposed four-bladed turbine is compared to the two-bladed SHTs having an OR of 0 and 0.2. The highest efficiency s is achieved as 19% by the modified four-bladed SHT at 0.5 TSR. The designs of the four-bladed SHT and the two-bladed SHTs are presented in Figure 2.3.



(a) 0 overlap Savonius (b) 0.2 Overlap (c)Modified four blade Savonius

Figure 2.3. Studied SHTs in (Thiyagaraj et al., 2016)

Additionally, (Talukdar et al., 2018) conducted a comparative analysis of the performances of a three-bladed SHT and two-bladed SHTs with semi-circular and elliptical blade profiles. Further details and findings of this research are presented in Section 4.1. Notably, the two-bladed SHT with semi-circular blade profiles achieved a 64% higher C_P than the three-bladed SHT.

2.3 Effect of Aspect Ratio on the Performance of Savonius Hydrokinetic Turbine

The aspect ratio (AR) of Savonius turbines is crucial as it helps to determine their hydrodynamic performance and overall efficiency. It has a substantial influence on the flow patterns and pressure distributions over the turbine blades which determine the turbine's energy conversion capabilities. In general, a larger aspect ratio results in a higher power coefficient. However, each turbine design has an optimum aspect ratio, and further increasing the aspect ratio beyond this point will yield negligible or only marginal additional performance gains. The ideal aspect ratio of a Savonius turbine design is determined by a number of elements, including blade shape, blade angle, flow medium, and flow speed.

The effect of aspect ratio on Savonius turbine performance has primarily been investigated in the context of wind energy applications. However, the growing interest in hydrokinetic applications has revealed a considerable gap in the existing literature. This section aims to present the current literature on the effect of AR on the performance of Savonius turbines by considering both wind energy and hydrokinetic applications. First, the existing literature on effect of AR on the performance of Savonius Wind Turbines (SWTs) will be presented. Subsequently, attention will be directed to the available literature examining the effects of AR on the performance of Savonius Hydrokinetic Turbines (SHTs). Finally, the findings synthesized from the presented literature will be summarized and discussed.

2.3.1 Literature on Savonius Wind Turbines (SWT)

(Alexander & Holownia, 1978) conducted wind tunnel tests on a SWT to determine the effect of different ARs, ORs, blade numbers and adding endplates on the efficiency of the turbine. The wind tunnel tests were conducted at varying wind speeds ranging from 6 m/s to 9 m/s. The ARs investigated during the tests were 1.2, 2.4, 3.6, and 4.8. According to the study, the efficiency of SWT improved gradually

with blade AR up to the maximum value of 4.8. The maximum power coefficient of 0.25 is obtained for AR of 4.8. (Kamoji et al., 2009a) conducted wind tunnel tests on a SWT with a modified blade geometry. In this study, researchers investigated the combined effect of OR, AR, blade arc angle and Reynolds number (Re) on the performance of studied modified blade geometry. Wind tunnel tests regarding the aspect ratio were carried out Re of 120,000 and 150,000 with varying aspect ratios of 0.60, 0.70, 0.77, and 1.00. This study found that a modified SWT with an AR of 0.70 performed better, reaching power coefficients of 0.19 and 0.21 at the corresponding Re. Additionally, this configuration exhibited higher starting torque values. (Kamoji et al., 2009b) also carried out a similar study for a SWT equipped with helical blades. Similar to the previous study of (Kamoji et al., 2009a), wind tunnel tests were carried out at Re of 120,000 and 150,000 with varying aspect ratios of 0.88, 0.93 and 1.17. The result of the study indicates that helical Savonius turbine with 0.93 AR generated higher power coefficient (0.165) at TSR 0.7. (Mahmoud et al., 2012) studied the effect of OR, AR, number of stages on the efficiency of a SWT. They conducted wind tunnel experiments with varying wind speeds between 6 m/s and 12 m/s for SWTs with changing ARs from 0.5 to 5. Their investigation showed that the power coefficient is increased with the increasing AR and wind speed. The highest power coefficient is obtained as 0.14 for AR of 5. (Roy & Saha, 2013a) also considered the effect of OR and AR as important factors effecting the performance of a SWT. They conducted wind tunnel experiments at speeds varying from 5 m/s to 10 m/s to investigate the efficiency of SWTs with ARs of 0.60, 0.70, 0.80, 0.90, and 1.00. The study concludes that the highest total power output is obtained at an AR of 1.00 due to larger projectile area, however, the highest efficiency is obtained at an AR of 0.80. The power coefficient of the turbine with AR 0.80 is 0.178, which is 15% higher than of the turbine with AR 1.00. (Torres et al., 2022) conducted a numerical study aiming optimization of the geometric design parameters of a SWT. Researchers suggested a design optimization method that employs two mathematical optimization model to determine the SWT layout which achieves the best aerodynamic performance. The first model is the Response Surface (RS) Model

which creates a mathematical model of the link between the design parameters and the turbine's aerodynamic performance. The RS is built from the results of CFD simulations of various turbine designs. The second approach is a multi-objective genetic algorithm (MOGA), which seeks the ideal SWT design by simultaneously optimizing various objectives such as power coefficient maximization and drag coefficient minimization. The MOGA use the RS to direct the search and choose the ideal SWT design. For the design optimization process, combine effect of the AR, OR and twist angle was considered. Effects of different ARs ranging from 5 to 9 on the efficiency are investigated. The resulting optimum SWT layout consist of 174.05˚ twisted blades with an AR of 8.38 and an overlap ratio of 0.08.

2.3.2 Literature on Savonius Hydrokinetic Turbine (SHT)

In the case of hydrokinetic applications of the Savonius turbine, studies examining the effect of the AR on the turbine performance are notably limited when compared to the wind energy applications. It is critical to re-examine the influence of AR on SHT performance, given the significant changes in working fluid and flow parameters. In wind energy applications, airflow is primarily generated by the pressure differences in the atmosphere and the static pressure variations on the blade geometry is negligible due to low density of the air. On the other hand, freestream water flows are governed by the gravity and the static pressure distribution on the blade can vary greatly in contrast to wind applications. Therefore, the static pressure variation is especially important for the vertical axis Savonius turbines.

(Mabrouki et al., 2014) performed an experimental study to investigate the hydrodynamic performance of two SHTs with different AR of 1.05 and 0.53. The tests were conducted in a square shaped closed conduit. According to the findings of the study, the SHT with AR of 0.53 outperformed the longer one by generating higher dynamic torque and power. In fact, the shorter SHT achieved a power coefficient of 0.19, while the longer SHT only managed to achieve a coefficient of 0.047. (Patel et al., 2017) carried out a comprehensive experimental study to

investigate the effect of OR and AR on the performance of a SHT. The conducted investigation comprised two phases. Firstly, the study examined the effect of adding endplates to the SHT, which significantly increased its overall performance. Secondly, the impact of various OR and AR values are investigated in 3 distinct canals. In this study, the turbine diameter remained constant; therefore, the height of the turbine is adjusted to achieve the desired AR values in contrast to other presented experimental studies in this part. These three canals were used to accommodate the increased turbine height. The outcome of the study revealed that an optimal OR of approximately 0.11 resulted in a power coefficient of 0.25. Furthermore, the findings indicated that as the AR increased while maintaining a constant overlap ratio (0.11), the power coefficient also exhibited an increase up to an AR of 1.8. Beyond an AR of 1.8, the coefficient of power remained constant and marginal changes observed.

2.3.3 Summary of the Literature on Impact of AR on the Performance of Savonius Turbine

The studies presented in the literature have yielded conflicting results with respect to the optimal AR of Savonius turbines. It is worth noting that the numerical investigations consistently demonstrate a positive correlation between greater AR values and improved turbine performance. However, the results from the experimental studies considered in this review have shown conflicting conclusions. A summary of the experimental studies is provided in Table 2.1, to facilitate a more comprehensive discussion regarding these divergent results.

Table 2.1 Summary of Experimental Studies on AR

Study	Fluid	C_P	AR	Constant Parameter
(Alexander & Holownia, 1978)	Air	0.250	4.80	H
(Kamoji et al., 2009a)	Air	0.210	0.70	H
(Kamoji et al., 2009b)	Air	0.165	0.93	H
(Mahmoud et al., 2012)	Air	0.140	5.00	H
(Mabrouki et al., 2014)	Water	0.190	0.53	D
(Patel et al., 2017)	Water		1.80	D

The AR is influenced by the diameter (D) and height (H) of the turbine. The relationship between AR, D, and H is defined by the below given relation.

$$AR = \frac{H}{D} \qquad \text{(Eqn. 1)}$$

AR is directly proportional to H and inversely proportional to D. In experimental testing, one of these parameters is kept constant, while the other one is manipulated to obtain the desired ARs. The choice of constant parameter is determined by practical considerations mainly related to the dimensions of the available channels. When the channel height is the limiting factor, the turbine's height (H) is held constant and the turbine's diameter is adjusted to achieve desired ARs. Increasing the diameter results in lower AR values but it also increases the blockage ratio in the channel.

The higher blockage ratio, especially for drag based turbines, re-directs the fluid flow to turbine blades and artificially inflates the measured power output. As observed in the Table 2.1, the studies considered H as the constant parameter generally achieved higher performances at AR values lower than 1.0, except for the studies of (Alexander & Holownia, 1978) and (Mahmoud et al., 2012). This can be attributed to the experimental methodology utilized in the studies conducted by Alexander and

(Alexander & Holownia, 1978), as well as by (Mahmoud et al., 2012). Notably, (Alexander & Holownia, 1978) employed a blockage ratio correction method to consider blockage effects on their preliminary results before publishing their findings. Additionally, (Mahmoud et al., 2012) used an open circuit wind tunnel in their experiments, where accelerated airflow directed toward the turbine test rig. In this setup, the test rig does not have enclosing walls around the turbine body, therefore the aforementioned effect of blockage ratio on the observed power output did not occur.

In cases where D is held constant, the blockage ratio is constant since the turbine and flow depth is extended. Therefore, both numerical and experimental investigations conclude that the performance of Savonius Turbine increases with an increase in AR when the turbine D is kept constant, except for the study conducted by (Mabrouki et al., 2014). While (Mabrouki et al., 2014) reported superior performance for the shorter turbine, the authors also highlight that the test channel used may not be suitable for the testing of the longer turbine.

The studies presented in this section exclusively consider vertical-axis turbines where the rotational axis of the turbine is vertical. Regarding hydrokinetic applications, only (Patel et al., 2017) provides explanation about the performance improvement associated with increased AR. They attribute this performance improvement to the increase hydrostatic pressure along the turbine height. There is a gap in the literature concerning the effect of AR on the performance of Savonius turbines for horizontal axis flow conditions. Additionally, there is a need to explain the underlying mechanism of AR's impact on performance for horizontal-axis conditions where the hydrostatic pressure changes along the turbine's diameter are negligible. Therefore, this thesis will investigate the impact of AR on the performance of Savonius hydrokinetic turbines with horizontal placement to address these research gaps.

2.4 Effect of Multi-stage Configurations on the Performance of Savonius Hydrokinetic Turbine

The goal of this section is to investigate the existing literature regarding the advantages of utilizing multi-stage configurations in Savonius Hydrokinetic turbines. This review aims to provide insight into their potential to improve power generation of the Savonius turbines.

The utilization of multi-stage configurations in SHT offers a high potential of achieving enhanced energy harvesting and power production capabilities. The arrangements of multi-stage configurations have a substantial impact on the power generation characteristics of the turbine. As discussed in Section 2.3, increased turbine length or height provides higher efficiency. Also, a higher AR results in larger swap area for a single turbine which improves overall economy by reducing number of additional required components (generators, cables, supporting structures etc.) for unit area. However, it should be noted that higher AR values cause larger torque fluctuations and a higher bending moment over the blades. The presence of torque fluctuations may present difficulties in the mechanical elements and electrical systems combined with the SHT. The combination of multiple Savonius turbines can effectively reduce torque fluctuations. Moreover, the multi-stage designs help to distribute the mechanical loads over several stages. Therefore, a multi-stage design can provide smoother power generation and enhance the reliability of the whole system.

The optimum design of the multi-stage Savonius turbine relies on several key factors: the number of stages, the effective AR, and the phase differences between them. In this context, the term "effective AR" is used to refer to the aspect ratio of each stage.

The literature on the influence of multi-stage configurations on the performance of SHTs will be presented in this section. Following that, the studies examined the effect of multi-staging on the performance of SWTs will be introduced. Finally, a

summary of the findings derived from the presented literature on both SHTs and SWTs will be provided.

2.4.1 Literature on Multi-stage Configurations of Savonius Hydrokinetic Turbine (SHT)

(Nakajima et al., 2008) conducted an experimental investigation to examine the influence of double staging on the performance of small-scale SHT. The effective ARs of the single staged turbine and the double staged turbine are reported as 2.4 and 1.2, respectively. However, it is essential to clarify that these ARs were derived based on the blade diameter. In contrast, the method employed in this thesis calculates ARs based on the rotor diameter, yielding AR values of 1.48 and 0.74 for the tested turbines as defined in Eqn. 1. In the experiments, two double staged turbines with phase differences of 0° and 90° and one single staged turbine are tested. The results indicate that the double staged turbine with a 90° phase difference achieved 10% higher C_p than the single staged turbine. Moreover, the double staged turbine with a 0° phase difference experienced a slight reduction in power generation which is attributed to the presence of the intermediate plate.

(Golecha et al., 2011) experimentally investigated the effect of deflector plates on the performance of SHTs featuring multiple stages and phase differences. The study incorporated various turbine configurations such as a single stage turbine, double-stage turbines with phase differences of 0° and 90° and a three-stage turbine with 60° phase difference. The overall AR of the tested turbines remained constant at 0.7. Consequently, the effective AR of the double-stage turbines and the three-stage turbine were reduced to 0.35 and 0.23 respectively. The findings of this study show that the single-staged turbine without deflector plate achieved a maximum C_p of 0.14 which is 7.69% and 60.92% more than the Cp values of the double-stage turbine with 90° phase difference and the three-stage turbine, respectively. Additionally, the double-stage turbine with 90° phase difference exhibited 8.33% higher C_p than its counterpart with a 0° phase difference. The addition of the deflector plates resulted

in a positive effect on the power generation across all-tested turbine configurations. The single-stage turbine with deflector plate exhibited the most enhancement with a 50% increase in C_p.

In two separate numerical studies, Kumar and Saini examined the impact of the multi-staging on the power generation of SHT (Kumar & Saini, 2016b, 2016a). In their first study, (Kumar & Saini, 2016a) analyzed the power generation of both single-stage and multi-stage SHTs equipped with twisted blades. The researchers utilized ANSYS Fluent software to conduct CFD simulations. The investigation involved the examination of three turbine configurations, namely a single-stage turbine, a double-stage turbine, and a three-stage turbine. These configurations were differentiated by varying AR of 1.58, 0.77, and 0.52, respectively. The simulations were conducted exclusively at a TSR of 0.7. The results of these simulations show that, among the tested configurations, the doubled-stage turbine achieved the highest C_p of 0.23. In their subsequent study, (Kumar & Saini, 2016b) proposed a multi-stage configuration consisting of stages with varying diameters and heights. The conceptual design for this configuration is presented in Figure 2.4. The dimensions of the stages are determined considering the vertical profile of a fully developed turbulent open channel flow which is characterized by 2.20 m/s freestream flow velocity. The proposed design attained a maximum C_p of 0.32 at TSR of 0.8.

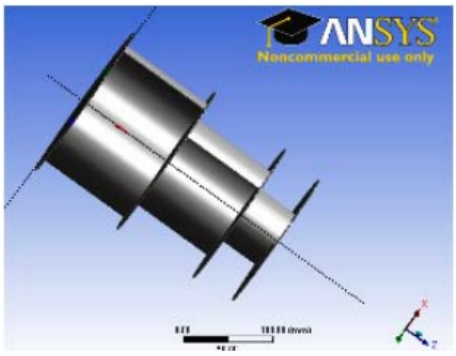


Figure 2.4. Developed Design in Study of (Kumar & Saini, 2016b)

Prabowoputra et al. conducted two comprehensive numerical studies to examine the impact of multi-stage designs on the performance of SHTs. These studies, documented in two separate papers (Mahesa Prabowoputra et al., 2020; Prabowoputra et al., 2021), were conducted with the aim of getting a thorough understanding of the complex dynamics of SHTs with diverse blade designs and stage arrangements. Both of these studies utilized a standardized SHT design, which included a rotor diameter (D) of 110 mm and a consistent AR of 1. The inlet velocity of 0.8 m/s remained constant throughout the simulations. In the first study, (Mahesa Prabowoputra et al., 2020) investigated the impact of multi-staging on the performance of SHTs under the horizontal axis conditions. This study examined the performance of single stage turbine, two stage turbine and three-stage turbine by considering varying phase differences. For the horizontal axis conditions, the three-stage turbine with 120º phase difference demonstrated the best performance by reaching a maximum C_p of 0.197. In contrast, the two-stage and three-stage turbines without any phase difference showed inferior performance compared to the single-stage turbine. In the second study conducted by (Prabowoputra et al., 2021), a comprehensive analysis was undertaken to compare vertical axis SHTs in three separate configurations, namely single-stage, double-stage, and three-stage. The SHTs were equipped with two different blade configurations, consisting of two blades and three blades. Additionally, the research examined various phase differences. The implementation of multi-stage setups reduced the effective aspect ratio to 0.5 and 0.3 for the two-stage and three-stage SHTs, respectively. The results of this investigation revealed differences in performance depending on the blade number of turbines. In the case of the two-blade configurations, both two-stage SHT with 90º phase difference and three-stage SHT with 60º phase difference exhibit better performance than the single stage SHT. On the other hand, in configurations with three blades, the single-stage SHT showed superior performance compared to the two-stage and three-stage variants. Overall, the single-stage SHT with three blades showed the best performance among the variants. The three-stage SHT and

two-stage SHT achieved the maximum C_p values at phase differences of the 60º and 90º, respectively.

(Kumar et al., 2020) carried out a comprehensive numerical study to investigate the impact of multi-stage configurations on the efficiency of a SHT with modified blade profiles. The studied SHTs consist of 12.5º twisted modified blades. The double-stage SHT and the three-stage SHT has phase differences of 90º and 120º, respectively. The researchers compared the performance of the single-stage SHT with an AR of 1.51, double-stage SHT with an effective AR of 0.76 and three-stage SHT with an effective AR of 0.50 under flows with various Re numbers. The findings of the study highlight that the increase of Re resulted in elevated maximum C_p for all tested SHT variants. The double-stage SHT exhibits the best performance over all tested Re numbers. The modified blade profile and the generated variants in this study illustrated in Figure 2.5.

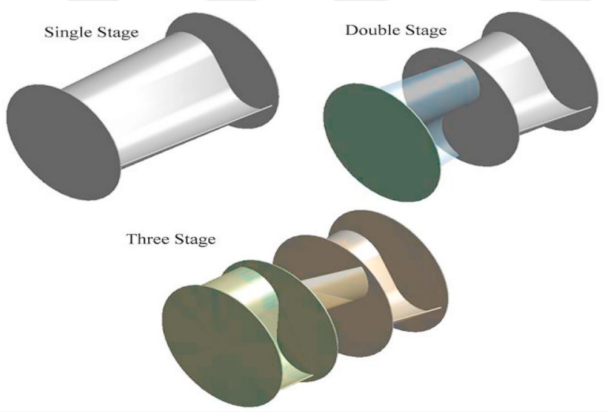


Figure 2.5. Investigated SHT variants in the study of (Kumar et al., 2020)

2.4.2 Literature on Multi-stage Configurations of Savonius Wind Turbine (SWT)

(Frikha et al., 2016) investigated the performance of SWTs having 1 to 5 stages with a constant effective AR of 0.23 under 3 m/s wind speed. Researchers conducted both experimental and numerical studies for this investigation. Their findings show that

the increase in the number of stages leads to improved performance and the highest C_p generated was 0.132 for the 5-stage turbine. (Saad et al., 2021) conducted a numerical study to investigate the performance of SWTs with stages of 1 to 4 and AR of 1 to 4. The researchers kept the effective AR as 1 for each stage and modeled single-stage SWTs corresponded to the overall AR of multi-stage configurations. The findings of this study show that multi-stage SWTs exhibit superior performance than the single stage counterparts. The highest Cp is obtained as 0.261 for the 4-staged SWT. Additionally, (Saad et al., 2022) carried out a comprehensive numerical study to investigate the effect of effective AR of the stages on the performance of several multi-stage SWTs. The researchers modeled SWTs with stage numbers ranging from 1 to 4, each consisting of stages with effective AR values of 0.50, 0.75, 1.0, 1.25, and 1.50. According to their results, an increased number of stages resulted in enhanced performance for all the studied effective ARs. Moreover, a reduced effective AR led to diminished performance for all the studied stage numbers. For example, when the stage's aspect ratio is increased from 0.5 to 1.5 for the 4-stage rotor, the power coefficient rises from 0.183 to 0.23.

2.4.3 Summary of Literature on Impact of Multi-stage Configurations on the Performance of Savonius Turbine

The existing literature on the effects of multi-stage designs on the performance of SHTs is limited to the studies discussed in section 2.4.1. When these studies are considered as a whole, the research on multi-stage configurations is conducted by maintaining a constant AR for the turbine. Then, the additional stages are created by dividing the turbine into sub-stages which results in a reduced effective AR for the sub-stages. The reduced effective AR leads to diminishing performance; therefore, many of these studies tend to favor single or two-stage configurations. In contrast, the studies presented in section 2.4.2 employed a different approach to examine the influence of multi-staging for the SWTs. Instead of decreasing the effective AR of the stages, the turbine’s AR is increased to achieve the same effective AR for each

stage. Unlike the studies conducted on SHTs, these studies, whether maintaining a constant or increased effective ARs, favor multi-stage configurations that consist of two or more stages.

The literature review highlights that the effective AR is one of the key parameters which determine the performance of the multi-stage configuration. When the effective AR is maintained as a constant value or increased, the performance of multi-stage configurations tends to improve with an increasing number of stages. On the contrary, when the effective AR is reduced below 0.5-0.6, the performance of the proposed multi-stage configuration tends to deteriorate. Notably, this literature review underscores a crucial gap in the existing research on the subject, the necessity of maintaining effective AR around 1.0 for assessing the performance of multi-stage configurations of SHTs. This gap is investigated as one of the specific test cases within the scope of this thesis. The research aims to contribute to the understanding of multi-stage configurations in SHTs, by maintaining an effective AR around 1.0 in the assessment of multi-stage configurations.

2.5 Effect of Adoptation of Twisted Blades on the Performance of SHTs

This section provides an overview of the existing literature focused on examining the influence of utilizing twisted, or helical, blades in SHTs and their impact on performance.

The integration of twisted blades in SHTs presents a considerable potential for enhancing power production capacity of SHTs. The twisted blades provide a continuous phase difference along the height or length of the turbine. Therefore, the adaptation of twisted blades suggests potential for reduced torque fluctuation similar to the effect observed in multi-stage configurations of SHTs. This reduction can help to improve efficiency and stability of the turbine. The literature review of optimization studies on the adaptation of twisted blades in SHTs are presented below.

(Zullah et al., 2010) conducted a numerical study to evaluate the performance of a SHT utilized in an oscillating water column (OWC) for wave energy conversion. The researchers tested three different models of the SHT, each with 3 blades and distinct twisted blade angles of 0°, 15°, and 30°. According to the results, the turbine having 30° twisted blades achieved the highest total efficiency of 12.64% which is 6.4% higher than the turbine without twisted blades.

(Kumar & Saini, 2017a) carried out a numerical study to evaluate the impact of applied blade twist angles of 0°, 12.5° and 25° on the performance of a two-semicircular-bladed SHT with an AR of 1.58 and an OR of 0. The researchers tested these twist angles under varying inlet velocities ranging from 0.5 to 2 m/s to observe the effect of Re on the model's performance. The findings of this study showed that the turbine with 12.5° twisted blades generated the highest C_p of 0.39 at 0.9 TSR under 2 m/s flow velocity. Moreover, the increase in Re resulted in increased power generation for all the studied twist angles. In a subsequent study, (Kumar & Saini, 2017b) investigated the effect of blade arc angle and blade shape factor on the performance of the SHT having 12.5° twisted blades. The same test conditions utilized in previous study are applied for the testing of new configuration. The results showed that the SHT with a 150° arc angle and a shape factor of 0.6, combined with 12.5° twisted blades, generated a maximum Cp of 0.426, which is 9.23% higher than the semicircular-bladed counterpart. (Hadi et al., 2019) conducted an experimental investigation to examine the effect of twisted blades on the performance of SHT in a water pipe. The studied turbine has an AR of 1 and an 82 mm diameter without any overlap. Tests are conducted for 4 different discharges, which are 0.0029 m^3/s, 0.0057 m^3/s, 0.0081 m^3/s, 0.0119 m^3/s. Blade twist angles of 0°, 12.5°, 30°, 45° and 60° are tested under these conditions. According to the findings of this study, the turbine having 60° twisted blades showed superior performance up to 0.0081 m^3/s discharge. However, the turbine without twisted blades exhibits higher performance at 0.0119 m^3/s discharge.

(Mosbahi et al., 2019) carried out an extensive study incorporating both experimental investigation and numerical investigation to examine the effect of a new deflector

system on the performance of three-bladed SHT. The researchers tested the performance of the three-bladed SHT with 30° twisted blades in an irrigation channel under 0.86 m/s flow velocity. Then, the data obtained was used to validate the numerical model developed for the optimization of the proposed deflector system. The results showed that three-bladed SHT without deflector system generated a C_p of 0.125 at TSR 0.7 and the proposed deflector system increased the generated C_p by 12%. In a separate publication, (Mosbahi et al., 2021) utilized same 30° twisted blades for a two-bladed SHT configuration, tested under the same experimental conditions. Moreover, the same proposed deflector system was also re-optimized for the two-bladed version. The results highlight that two-bladed configuration without a deflector system generated a C_p of 0.166 at a TSR 0.78 which is 32.8% higher than the three-bladed counterpart. Furthermore, the deflector system further increased the performance of two-bladed SHT by 17.5%. (Nag & Sarkar, 2020) conducted a comprehensive study integrating both experimental and numerical investigations to compare the performance of a conventional SHT, a modified SHT having an overlap and larger shaft diameter and a helical SHT having a blade arc angle of 124° and a 90° blade twist angle. The rotor diameters and ARs of the turbines were kept constant. The experimental tests were carried out in a rectangular open channel with a 1 m/s freestream flow velocity. Moreover, the researchers also placed a converging-diverging duct with a constant duct angle of 29° to observe the impact of this duct on the performance of the tested turbine variations. The result of the experimental study was used to validate the developed numerical model. Then, the numerical model utilized to extent the studied freestream velocity to 2 m /s and 3 m/s and the studied duct angles to 20°-32°. According to the findings, the helical SHT showed superior performance among the studied configurations, achieving a maximum power generation of 1.58 W at 1 m/s freestream velocity without duct which is 9.7% higher than of conventional one. Moreover, the helical SHT with duct generated 26% and 48% higher power than the conventional SHT with duct and conventional SHT without duct, respectively.

The existing literature regarding the performance of SHTs having twisted blades are limited to the studies presented. Among these studies, only two have specifically focused on the blade twist angles, which are covering a limited range of angles (Hadi et al., 2019; Kumar & Saini, 2017a). While the existing studies offer valuable insights into blade twist angles, the literature have limitations in terms of the range of angles investigated for SHTs. Recognizing this gap, the research presented in this thesis attempts to fill this existing gap in literature by methodologically investigating a wide range of twist angles. Through this extended exploration of twist angles, the research aims to contribute a more comprehensive understanding of the impact of blade twist on the performance of SHTs, thus filling an existing gap in the literature.

2.6 Numerical Modeling of the Savonius Turbines

This subsection will explain the turbulent characteristic of the flow field around the STs. Also, the studies on the numerical modeling of the STs will be introduced by specifically focusing on appropriate choose of the turbulence models and discretization techniques for numerical simulations of the STs.

2.6.1 The Flow Field around the Savonius Turbines

The successive numerical modeling of STs depend on accurate solution of the flow field around them. In the literature, many researchers employed techniques such as particle image velocimetry (PIV) or particle tracking velocimetry (PTV) to visualize the velocity field within and around the turbine (Dobrev & Massouh, 2011; Fujisawa, 1996; Fujisawa & Gotoh, 1992; Murai et al., 2007; Shigetomi et al., 2011). The findings of these studies showed that the flow field around a ST typically exhibits inherent turbulence. In Figure 2.6, the flow field around a SWT is illustrated at several rotational positions.

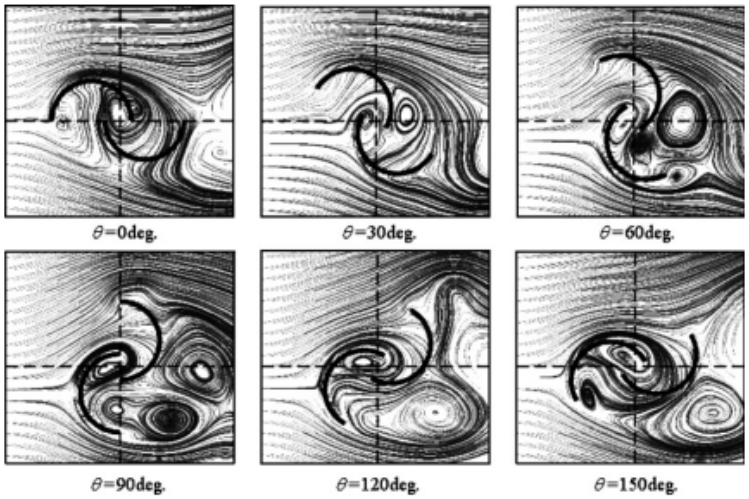


Figure 2.6. Flow visualization for a SWT at different azimuth angles (Murai et al., 2007)

Several factors contribute to the formation of turbulence flow around STs. Firstly, the blades of a Savonius turbine have a unique shape that naturally creates turbulence in the flow. When the fluid flow encounters the concave side or the convex side of the blade, the flow naturally conforms to its shape, inducing a turbulent wake behind the blades. Moreover, the flow field over the convex side of the returning blade and the concave side of the advancing blade are inherently different from each other as can be clearly observed in Figure 6.11 and Figure 6.10. As a result, the pressure field in front of the advancing blade and the returning blade are different, which enables the rotation of the turbine. This imbalance in the pressure fields introduces fluctuations in the flow, thereby contributing to formation of turbulence. Secondly, the rotation of the ST further amplifies these effects since both rotational position and the direction of the blades changes continuously. Furthermore, the blades of a ST are susceptible to vortex shedding due to their shape and their rotation. The periodically formed vortices in front of the concave side of the blades and at the tips are shed from the trailing edge of the blades with rotation of the ST.

2.6.2 Literature Review on the Numerical Modeling of the Savonius Turbines

In computational fluid dynamics simulations, accurately predicting the turbulent flow patterns surrounding the STs depends on the appropriate selection of the numerical discretization method and the turbulence model.

Numerical discretization methods are used in CFD simulations to approximate and solve the partial differential governing equations of fluid flow by transforming them in to discrete forms. Two commonly employed numerical discretization methods in 3D CFD simulations are the finite volume method (FVM) and the finite element method (FEM). It is noteworthy that, in comparison to FVM, the FEM method is more susceptible to used mesh type and the quality of mesh elements (Jeong & Seong, 2014). Furthermore, the computational expense associated with FEM is higher than the FVM (Jeong & Seong, 2014). Additionally, FEM codes typically rely on structured meshes while, the FVM codes can handle both unstructured and structured meshes (Alom et al., 2021; Jeong & Seong, 2014; Roy & Saha, 2013b). Because of the complex geometry of the STs, a FVM code that can be handle unstructured mesh is more suitable for the 3D CFD simulation of STs. In fact, all the numerical studies presented in the Chapter 2 uses a FVM code for CFD simulations of STs.

There are several CFD software options based on FVM such as ANSYS Fluent, ANSYS CFX, STAR-CCM+ and OpenFOAM. ANSYS Fluent stands out due to its widespread preference over other options and its extensive range of turbulence model choices. Furthermore, ANSYS Fluent can utilize both unstructured and structured mesh. Therefore, a vast majority of the studies presented in the Chapter 2 use ANSYS Fluent to conduct CFD simulations.

The choice of turbulence model is another important aspect of achieving successful CFD simulations of the STs. The turbulence models are essential tools for CFD simulations to capture complex and chaotic behavior of turbulent flows around the

STs. In literature, several studies have undertaken comparative analyses to assess the performance of different turbulence models concerning their predictive accuracy in describing the flow field and performance characteristics of STs.

(Dobrev & Massouh, 2011) conducted an experimental and numerical investigation to determine the accuracy of Shear Stress Transport (SST) k-ω turbulence model and a hybrid Detach Eddy Simulations (DES) with SST k-ω. For the SST k-ω turbulence model, both 2D and 3D simulations were carried out. In experiments, a two-bladed SWT was tested under wind velocity ranging from 9 m/s to 15 m/s using PIV. The findings showed that the DES-SST k-ω model demonstrated better alignment with experimental results. On the other hand, the computational cost of DES-SST k-ω model is significantly higher than SST k-ω model. Notably, the 3D simulations with the SST k-ω model exhibited better agreement with experimental findings compared to 2D simulations.

(Nasef et al., 2013) conducted a numerical investigation to compare various turbulent models: RNG k-ε, Realizable k-ε, Standard k-ε, SST k-ω, against static torque coefficients derived from two distinct experimental studies. The SST k-ω model exhibited highest accuracy in line with the outcomes of both experimental studies.

(Ferrari et al., 2017) conducted both 2D and 3D CFD simulations utilizing Spalart-Allmaras (SA), Realizable k-ε, SST k-ω turbulence models. The results of the simulations were compared to an experimental data obtained from existing literature. The results show that 2D simulations tented to significantly overestimate the turbine performance compared to 3D simulations and experimental data. The SST k-ω showed better agreement with the numerical data compared to other models.

(Alom et al., 2021) conducted 2D simulations to determine the appropriate turbulence model for capturing the complex physics of turbulent flow around a SWT. The 2D CFD simulations were conducted by utilizing Transition SST (TSST), Standard k-ε, Realizable k-ε, RNG k-ε, Standard k-ω and SST k-ω. The findings show that the SST k-ω exhibited the lowest deviation from the experimental data.

The literature review presented in this section highlights the flexibility of FVM based software in mesh generation for ST geometries. ANSYS Fluent emerges as a popular choice among researchers engaged in CFD simulations of STs due to the aforementioned benefits. Moreover, SST k-ω proves capable of capturing complex and chaotic nature of turbulent flow around the STs. Therefore, this thesis will utilize ANSYS Fluent software with the SST k-ω turbulence model in its CFD simulations.

CHAPTER 3

METHODOLOGY

In this section, the methodology employed in this thesis will be introduced along with its objectives. The performance evaluation parameters, utilized to assess the performance of test cases, will be defined. The governing equations, solved in the simulations, will be presented, incorporating the chosen turbulence model. Furthermore, the implementation of a dynamic mesh technique to simulate the rotation of the Savonius Hydrokinetic Turbine (SHT) will be outlined.

3.1 Introduction

This study aims to analyze Savonius-type drag-based hydrokinetic turbines using numerical methods. As discussed in Section 2.1, Savonius turbines possess unique blade geometries that rely on drag forces and viscous forces to extract energy from flowing water bodies. Due to the unequal movement and asymmetrical shape of the returning and advancing blades, Savonius-type turbine blades deviate from the streamlined shape commonly associated with propeller-bladed turbine types. The asymmetrical movement of the two blades influences the streamlines, causing them to move in the opposite direction when impacted by the returning blade. Moreover, it is essential to fully solve the viscous effects on convex side of the returning blade, in order to estimate negative torque on the turbine. Considering the flow characteristics around the Savonius-type blades, CFD is employed for the proposed numerical simulations over potential flow codes/theory. By using CFD, the methodology of this thesis enables a detailed analysis of the transient hydrodynamic characteristics of the Savonius turbine design. CFD allows for an accurate prediction of the flow patterns, velocity distributions, pressure distributions, and turbulence characteristics around the turbine blades. This accuracy is crucial for understanding

the interaction between the curved blades and the flow, including flow separation, vortex shedding, and enhanced drag effects. Furthermore, the effect of several different design parameters on the performance of the chosen turbine is analyzed in this thesis. CFD provides flexibility in modeling different operating conditions and changing design parameters such as aspect ratio, blade numbers, compared to the experimental methods that require re-construction of the test setup and turbine body for every test case. CFD facilitates the evaluation of the Savonius turbine design parameters by providing detailed quantitative data on the impact of different design modifications on the flow behavior and performance metrics.

For the numerical simulations, both the 2022 and 2023 editions of the Ansys Fluent software are used. The inclusion of both editions was necessary as a new version was released during this study to ensure access to the latest features and capabilities offered by Ansys Fluent.

In the next section, the performance evaluation parameters will be introduced. Subsequently, the governing equations for the CFD simulations will be discussed. Following that, attention will be given to the resolution of the turbulence closure problem. Finally, the introduction of the employed dynamic mesh model will be presented.

3.2 Performance Evaluation Parameters

The performance of the turbine is evaluated based on two parameters: the torque coefficient (C_T) and the power coefficient (C_P). The C_P represents the ratio of the power extracted by turbine to the total available power of the water flow through the turbine's projectile area. The power coefficient is calculated using the following formula:

$$C_P = \frac{P_{ext}}{P_{av}} = \frac{T_{out} \times \omega}{\frac{1}{2}\rho V_0^3 A_{ref}} \qquad \text{(Eqn. 2)}$$

where V_0 is the inflow velocity and ρ is the density of the fluid medium. A_{ref} represents the projectile area of the turbine perpendicular to inflow direction, which is defined as product of the height of the turbine (H_T) and the diameter of the turbine (D_T). ω is the rotational velocity of the rotating turbine. T_{out} is the torque extracted by the turbine which is determined by numerically integrating the pressure and shear terms over the turbine walls around the rotational axis. In Ansys Fluent, this integration is performed for each boundary layer cells by allowing the calculation of the net torque for each time step of the simulation.

Similarly, the C_T is defined as the ratio of the torque extracted by the turbine to the total available torque of the water flow through the turbine's projectile area. The torque coefficient is calculated as follows:

$$C_T = \frac{T_{out}}{\frac{1}{2}\rho V_0^2 A_{ref} r} \quad \text{(Eqn. 3)}$$

A common practice is to present obtained power and torque coefficients over the tip-speed-ratio (TSR) to generate characteristic power generation curves and torque generation curves of SHTs. Both the power and torque generation curves provide valuable insights into the turbine's performance at different operating conditions, allowing for the identification of the optimal operational range and the maximum power output. The TSR is defined as the ratio of the blade tip speed to the inflow velocity.

$$TSR = \frac{\omega_0 \times r}{V_0} \quad \text{(Eqn. 4)}$$

3.3 Governing Equations

In this study, the governing equation for the CFD simulations is Reynolds-Averaged-Navier-Stokes (RANS) equations. This section will introduce the derivation of RANS equation from Navier-Stokes Equations.

3.3.1 Navier-Stokes Equations for Incompressible Flow

The conservation of mass, momentum, and energy in flow field is described by the Navier-Stokes equations. These equations are derived by applying the principles of mass and momentum conservation to a control volume within the fluid domain i.e., mesh cells. The general form of the Navier-Stokes equations for incompresible flow is expressed as follows:

$$Continuity\ Equation: \frac{\partial u_i}{\partial x_i} = 0 \qquad \text{(Eqn. 5)}$$

$$Momentum\ Equation: \rho \frac{\partial u_i}{\partial t} + \rho \frac{\partial u_i}{\partial x_j} = -\frac{\partial P}{\partial x_i} + \mu \frac{\partial^2 u_i}{\partial x_j \partial x_j} \qquad \text{(Eqn. 6)}$$

Here, ρ is the density of the fluid, u is the velocity vector, P is the pressure, μ is the dynamic viscosity, g is the acceleration due to gravity, x is the position component in Cartesian Coordinate System.

3.3.2 Reynolds-Averaged-Navier-Stokes (RANS) Equations for Incompressible Flow

The flow field in this study is characterized by turbulence. The Navier-Stokes Equations are theoretically applicable for both laminar and turbulent flow regimes. However, in the case of the turbulent flow, directly solving the Navier-Stokes Equations for all scales of turbulence is computationally infeasible since, resolving

all scales requires a computational grid with extremely high resolution. Instead, a statistical approach known as Reynolds Averaging is employed to handle turbulent flow characteristics. This approach involves decomposing the flow variables into time- averaged mean and fluctuating components.

By applying Reynolds decomposition to the flow variables (u_i, P), the following expressions are obtained:

$$u_i = \bar{u}_i + u_i' \quad \text{(Eqn. 7)}$$

$$P = \bar{P} + P' \quad \text{(Eqn. 8)}$$

Substituting these decomposed variables (Eqn. 7 and Eqn. 8) into the Navier -Stokes Equations (Eqn. 5 and Eqn. 6) results in a set of equations that separate the mean and fluctuating components. By taking the Reynolds average (i.e time-average) of these equations, Reynold-Averaged- Navier-Stokes Equations are obtained and presented as folows:

$$\frac{\partial \bar{u}_i}{\partial x_i} = 0 \quad \text{(Eqn. 9)}$$

$$\rho \frac{\partial \bar{u}_i}{\partial t} + \rho \bar{u}_j \frac{\partial \bar{u}_j}{\partial x_j} = -\frac{\partial \bar{P}}{\partial x_i} + \frac{\partial}{\partial x_j}\left[\mu\left(\frac{\partial \bar{u}_i}{x_j} + \frac{\partial \bar{u}_j}{\partial x_i}\right) - \rho\overline{u_\iota' u_j'}\right] \quad \text{(Eqn. 10)}$$

where the $\mu\left(\frac{\partial \bar{u}_i}{x_j} + \frac{\partial \bar{u}_j}{\partial x_i}\right)$ terms represents the viscous stress terms $((\tau_{i,j})_{laminar})$ associated with the mean flow, while $-\rho\overline{u_\iota' u_j'}$ represents the Reynolds Stress terms $((\tau_{i,j})_{turbulent})$ associated with the turbulent fluctuations.

The Reynolds stress terms, represented by$-\rho\overline{u_\iota' u_j'}$, form a tensor known as the Reynolds stress tensor and result in additional nine unknowns. It represents the correlation between the fluctuating velocity components. Due to these additional unknowns, turbulence models are used to approximate and model the Reynolds

Stress terms. These models introduce additional equations and closure assumptions to estimate the turbulent quantities. In addition, the selection of a turbulence model is influenced by the particular flow conditions, desired level of precision, and computational resources at hand. These factors will be explored further in Section 3.4.

By employing the Reynolds-averaged Navier-Stokes (RANS) equations for the numerical simulations, this study aims to efficiently simulate turbulent flows while capturing the dominant turbulence characteristics without the need to resolve all scales of turbulence. Also, RANS simulations provide valuable insights into the flow patterns, velocity distributions, pressure distributions, and turbulence characteristics around the hydrokinetic turbine blades. This information is essential for understanding the performance and behavior of the turbine under various turbulent flow conditions.

3.4 Turbulence Model

As explained in Section 3.3.2, the application of Reynolds-averaging to Navier-Stokes Equations introduces additional unknowns called Reynolds stresses ($(\tau_{i,j})_{turbulent}$). In order to effectively solve the system of equations and facilitate computational analysis, turbulence models are required. These models offer expressions or equations that can be used to estimate $(\tau_{i,j})_{turbulent}$, by utilizing the known mean flow variables.

Based on the literature review presented in Section 2.6.2 regarding the choice of turbulence models for SHTs, the SST k-ω turbulence model will be employed in the CFD simulations conducted in this thesis. Therefore, this section will provide description of SST k-ω model.

3.4.1 SST k-ω Turbulence Model

The SST k-omega turbulence model is a commonly employed two-equation model in CFD for simulating turbulent flows. This model integrates components from the k-ε model and the k-ω model and produces precise predictions for a broad spectrum of flow conditions.

The k-ε model has proven to be highly effective in a wide range of flow scenarios (Avva et al., 1990). However, this model has several recognized limitations especially in its responsiveness to adverse pressure gradients (Avva et al., 1990; Menter, 1992, 1994), which is a significant drawback for simulations involving SHTs. In cases where flow separations are present, the model inaccurately predicts excessively high shear-stress levels, resulting in the delay or complete prevention of separation (Avva et al., 1990; Menter, 1992, 1994).

To handle drawbacks of the k-ε turbulence model in predicting flow separations, an alternative turbulence model k-ω was introduced by (Wilcox & Rubesin, 1980). Although the k-ω turbulence model was significantly better in predicting flow separation and solving boundary layer than the k-ε, its results in freestream region was significantly susceptible to freestream values (Menter, 1992, 1994).

In an effort to overcome the shortcomings of both turbulence models and leverage their respective strengths, (Menter, 1992, 1994) introduced the Baseline k-ω model. This model combines both the k-ω and the k-ε models using a blending function. In this model, the blending function enables the Baseline k-ω model to utilize the k-ω model for boundary layer region and the k-ε model for the freestream region. (Menter, 1992, 1994) further improved by integrating a shear stress transport equation to accommodate the transport effect of turbulence stresses. The resulting model was named as SST k-ω turbulence model.

The transport equations adopted from the Baseline k-ω model for the SST k-ω turbulence model in ANSYS Fluent are formulated as follows (ANSYS, 2023):

$$\frac{\partial(\rho k)}{\partial t}+\frac{\partial(\rho k u_i)}{\partial x_i} = \frac{\partial}{\partial x_j}\left(\left(\mu+\frac{\mu_t}{\sigma_k}\right)\frac{\partial k}{\partial x_j}\right)+\rho\overline{u'}_i\overline{u'}_j\frac{\partial u_j}{\partial x_i}-\beta^*\rho k\omega \quad \text{(Eqn. 11)}$$

$$\frac{\partial(\rho\omega)}{\partial t}+\frac{\partial(\rho\omega u_i)}{\partial x_i} = \frac{\partial}{\partial x_j}\left(\left(\mu+\frac{\mu_t}{\sigma_\omega}\right)\frac{\partial\omega}{\partial x_j}\right)+2(1-F_1)\frac{\rho}{\sigma_{\omega,2}\omega}\frac{\partial k}{\partial x_j}\frac{\partial\omega}{\partial x_j} +\alpha\frac{\omega}{k}\rho\overline{u'}_i\overline{u'}_j-\beta^*\rho\omega^2 \quad \text{(Eqn. 12)}$$

where F_1 is the blending function which controls the gradual change between the k-ε and the k-ω models depending on the distance from the boundary layer. The blending function is formulated as

$$F_1 = tanh\left[min\left(max\left(\frac{\sqrt{k}}{0.09\omega y},\frac{500\mu}{\rho y^2\omega}\right),\left(\frac{4\rho k}{\sigma_{\omega,2}D_\omega y^2}\right)\right)\right] \quad \text{(Eqn. 13)}$$

where D_ω is defined as

$$D_\omega = \max\left[\left(2\rho\frac{1}{\sigma_{\omega,2}}\frac{1}{\omega}\frac{\partial k}{\partial x_j}\frac{\partial\omega}{\partial x_j}\right),(10^{-10})\right] \quad \text{(Eqn. 14)}$$

The modified turbulent viscosity modeling, incorporating transport of shear stresses, in the SST k-ω turbulence model defined as

$$\mu_t = \frac{\rho k}{\omega}\frac{1}{max\left[\frac{1}{\alpha^*},\frac{SF_2}{a_1\omega}\right]} \quad \text{(Eqn. 15)}$$

$$F_2 = tanh\left[max\left(\left(2\frac{\sqrt{k}}{0.09\omega y}\right),\left(\frac{500\mu}{\rho y^2 \omega}\right)\right)\right] \qquad \text{(Eqn. 16)}$$

3.5 Used Dynamic Mesh Model: Sliding Mesh Model

Traditional CFD simulations use a fixed mesh and examine fluid flow in a fixed reference frame. However, when a part of the structure is rotating or translating as in a turning hydrokinetic turbine, a dynamic mesh model is required to correctly represent the flow behavior. The Sliding Mesh model is a dynamic mesh model in Ansys Fluent used to simulate fluid-structure interactions in domains with rotating or translating parts.

To use the Sliding Mesh Model, individual meshes are created for fixed regions and rotating regions. Within the created mesh, sliding/moving zones are assigned to identify the location where movement occurs. In the contact region of these fixed and rotating zones, non-conformal interfaces are created by Ansys Fluent to transfer information between these zones. Specific boundary conditions are established for the moving zones to describe the rotation or transition of the studied structure. The Sliding Mesh Model employs an unsteady approach that handles the rotation/translation of the mesh in time through small incremental steps. In each time step, the solver considers the movement of translating or rotating components and updates the position and orientation of the sliding zones. The mesh interfaces are also constantly updated during each time step to maintain the connectivity of the fixed and the moving zones. Then, the data transfer between the fixed and the moving zones are accomplished by employing interpolation methods which consider the overlapping portions of the mesh faces on the defined interface zones.

CHAPTER 4

NUMERICAL SETUP

This chapter outlines the detailed framework and procedures adopted to develop and validate the numerical model. The developed model aims to establish a strong foundation for accurate and reliable findings. The integration of experimental data obtained from a comprehensive study provides the foundation of this numerical model by guaranteeing that the model is in accordance with real-world flow circumstances.

The experimental work of (Talukdar et al., 2018) is used to validate the developed numerical model. Moreover, two key investigations are carried out to improve the accuracy of the numerical model and the computational efficiency: Time-step Independency Study and Mesh Independency Study. The optimal grid resolution and time-step that ensures consistent and convergent results are determined. Moreover, the flume used in the experiments is separately modelled to obtain velocity distribution in the channel. This obtained velocity distribution is then applied as an inlet condition for the turbine simulations, reducing computational time significantly.

In this chapter, firstly, the experimental work carried out by (Talukdar et al., 2018) will be introduced. Subsequently, the processes of geometry creation and meshing, based on the experimental setup described in the aforementioned study, will be explained. Following that, the explanation of obtaining the inlet velocity for CFD simulations will be introduced based on the flume geometry utilized in the experiments by (Talukdar et al., 2018). Subsequent sections will cover the introduction of the numerical model development for SHT simulations, including mesh independence and time-step independence studies. Lastly, a comparative analysis will be presented, comparing the results of the numerical model with the experimental work conducted by (Talukdar et al., 2018).

4.1 Experimental Work Carried Out By (Talukdar et al., 2018)

(Talukdar et al., 2018) carried out an extensive experimental and numerical analysis on a Savonius turbine to determine the effect of elliptical blade shape, different immersion levels, number of blades on the performance of a SHT. The researchers used the experimental results to evaluate the performance of the studied SHT, while the numerical studies are used to understand and visualize the flow field around the turbine for different conditions.

Two-bladed and three-bladed SHTs are tested under same conditions to evaluate the effect of increased number of blades on the performance of the turbine. The results of the tests indicate that the two-bladed design shows superior performance compare to the three-bladed one. The maximum braking load for the two-bladed design is 1.18 Nm while the three-bladed design only achieves 0.91 Nm. Also, two-bladed and three-bladed models achieved a maximum power coefficient of 0.28 and 0.17 respectively, occurring at their optimal TSR of 0.89 and 0.71.

A Savonius turbine with elliptical blades that have 144 mm chord length and 47.5˚ sectional cut angle is constructed to investigate the effect of elliptical blade shape on the performance of the turbine. Elliptical bladed turbine achieved power coefficient of 0.20 at TSR of 0.77.

The effect of immersion level on the performance is investigated for an elliptical-bladed turbine, a two-bladed turbine and a three-bladed turbine at 100%, 80% and 60% immersion levels. According to the result of the study, large performance losses were observed with decreased immersion level. As the immersion level decreases from 100% to 60%, the power coefficient values of the three-bladed semicircular, two-bladed semicircular, and two-bladed elliptical SHTs experience reductions of 70%, 75%, and 90%, respectively. Similarly, a change in immersion level from 100% to 80% leads to power coefficient drops of 58.8%, 64.2%, and 80% for the three-bladed semicircular, two-bladed semicircular, and two-bladed elliptical turbines, respectively.

The results of two-semicircular-bladed SHT used to validate and develop the numerical model utilized in this thesis. The experimental setup and the design of two-semicircular SHT turbine is detailed in the following sections.

4.1.1 Experimental Setup

The experimental setup employed by (Talukdar et al., 2018) consists of a support structure housing the vertically placed SHT and a pulley system connected to two spring balances. The experimental setup is presented in Figure 4.1. The turbine was placed in the open channel; then it was let to spin without any load. The spring balances were used to progressively apply mechanical stresses on the braking pulley.

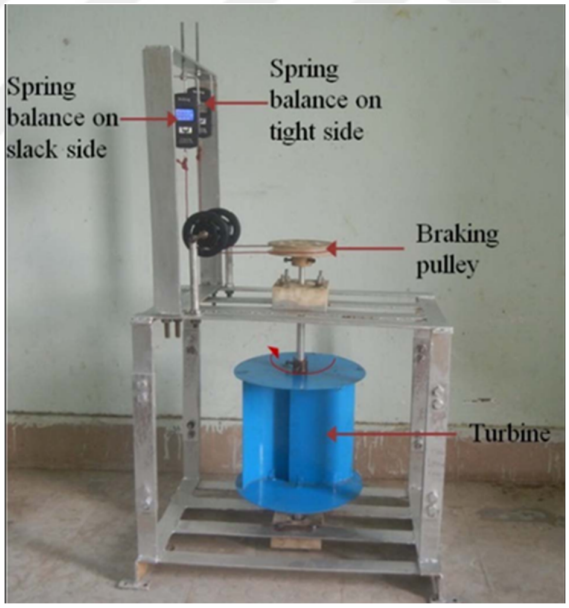


Figure 4.1. Experimental Setup (Talukdar et al., 2018)

The experiments are carried out in an open channel at IIT Guwahati's water treatment plant where the flume is made of cement walls. The flume is showed in Figure 4.2. The channel is 1 m wide and 0.9 m in height. The experiments are carried out at the converging portion of the channel under the 0.8 m/s flow velocity. The converging portion is 0.58m wide and also showed in Figure 4.2.



Figure 4.2. Open channel used in experiments and the used channel section (at left) by (Talukdar et al., 2018)

The authors specified that the precision of measuring TSR is within ± 1.5%, and the precision of determining C_P is within ±2.12%, based on the accuracy of the measurement devices.

4.1.2 Design Parameters of the Two-Semicircular Bladed Turbine

The two-bladed turbine investigated by (Talukdar et al., 2018) has a height of 250 mm. Mild steel sheets are used to fabricate the 1.3 mm thick semicircular blades. Each blade is formed to have a chord length of 144 mm. Then, these blades are attached to a 16 mm central shaft with an overlap ratio of 0.15, resulting in a turbine with a diameter of 250 mm. Additionally, endplates having a 277.2 mm diameter are placed at the bottom and top of the turbine. The thickness of the endplates is not specified. The turbine geometry is presented in Figure 4.3 and the design parameters are listed in Table 4.1.

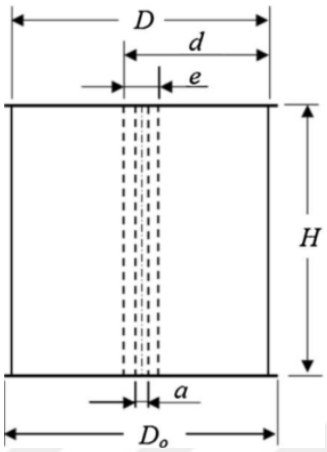


Figure 4.3. Two-bladed SHT Design (Talukdar et al., 2018)

Table 4.1 Design Parameters of Two-bladed Turbine (Talukdar et al., 2018)

Parameters	Value	Unit
Height of the turbine (H)	250	mm
Diameter of the turbine (D)	250	mm
Diameter of the blade (d)	144	mm
Central shaft (a)	16	mm
Endplate Diameter (D_{plate})	277.2	mm
Overlap Ratio (e/D)	0.15	-

4.2 Geometry Generation and Meshing

Ansys SpaceClaim 3D modeling software is used to create CAD models used in the Ansys Fluent simulations. Ansys SpaceClaim is preferred due to its comprehensive direct modeling capabilities and its ability to directly communicate with Ansys Fluent. Ansys Meshing software is used to mesh the created 3D models.

3D CAD model of the channel domain is created to match the provided cross-sectional dimensions of the experimental channel. The length of the channel domain is modeled as 5 m in order to obtain the fully developed velocity distribution at the outlet section. The model of the experimental channel is showed in Figure 4.4.

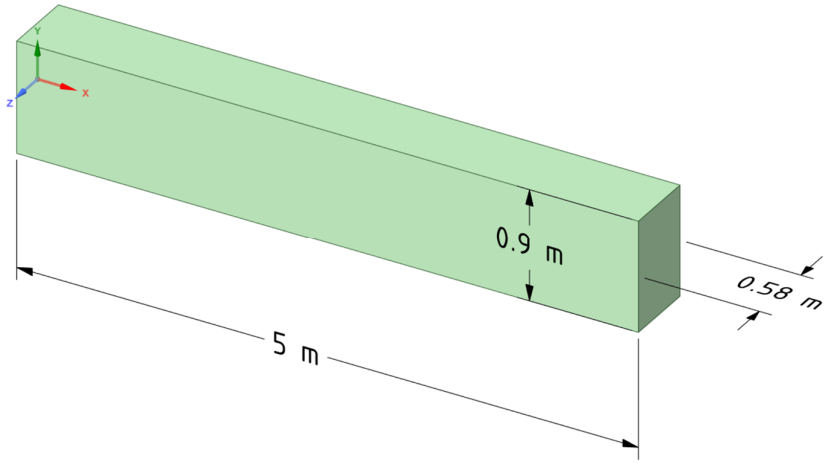


Figure 4.4. CAD Model of the flume

The channel model is then meshed by using the Ansys Meshing software. Structured hex meshes are used due to the simple geometry of this model. A mesh size of 0.013 m is determined sufficient for the structured hex meshes. The wall boundaries of the model need special treatment to solve the higher shears exposed by the no-slip walls. Moreover, wall roughness model of Icing Model is utilized to represent the roughness of the cemented walls of the flume. Therefore, 20 inflation layers of total thickness of 5 mm applied on wall regions. Overall, the created mesh of the flume

consists of 2604525 mesh elements. The generated mesh of the channel and the generated inflation layers are showed in Figure 4.5 and Figure 4.6, respectively.

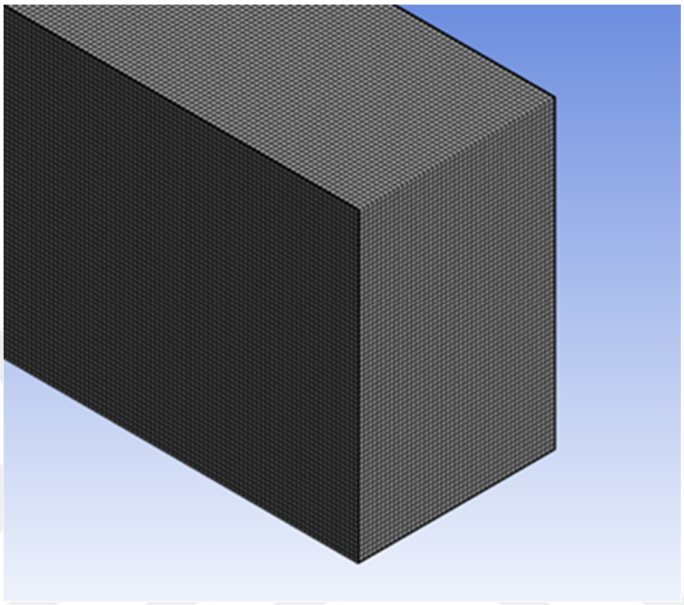


Figure 4.5. Generated Mesh of the Channel

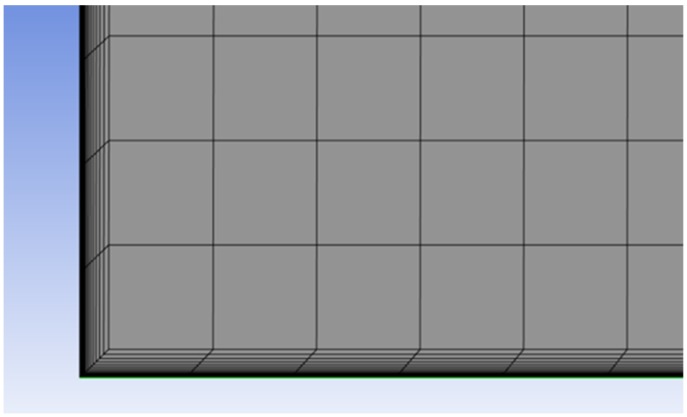


Figure 4.6. Generated Inflation Layer of the Channel

Two separate domains are generated for the turbine simulations. Firstly, a cylindrical domain named as Rotational Domain is generated to house the turbine geometry and be able to reflect the rotation of the turbine. Secondly, a rectangular prism domain named as Static Domain is generated. The rotational domain diameter is determined

as 1.5$D_{turbine}$ and the height is determined as 300 mm. The turbine geometry is created separately and extruded from the middle of the rotational domain. The turbine geometry is modeled to match the provided turbine parameters at Table 4.1. However, the thickness of the endplates was not provided by (Talukdar et al., 2018) as discussed in section 4.1.2, it is assumed as 3 mm in the modeling process by considering 1.3 mm blade thickness. The Rotational Domain is presented in Figure 4.7.

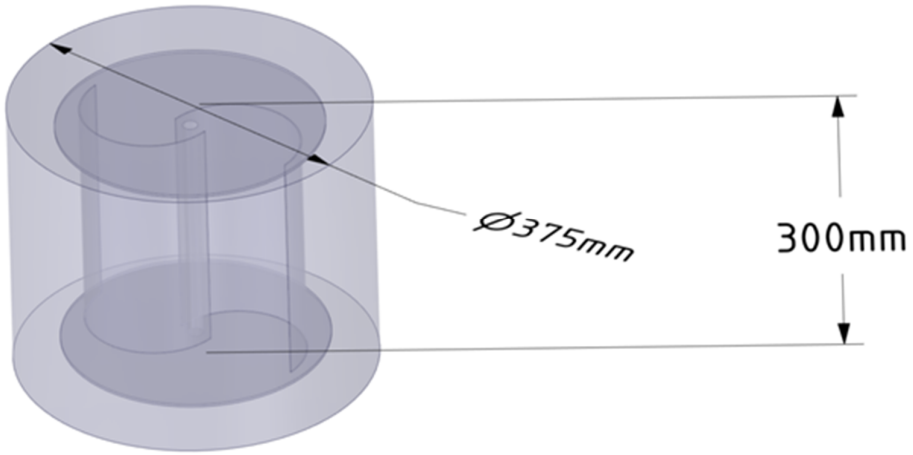


Figure 4.7. CAD Model of Rotational Domain

The static domain is modeled to have a matching cylindrical void to house the Rotational domain at the origin. The side boundaries of the Static Domain are positioned at a distance of 2.5$D_{turbine}$ from the turbine. The inlet is placed at 3D away from the turbine and the outlet is placed at 5$D_{turbine}$ from the turbine. The bottom and top boundaries are positioned 165 mm away from the turbine. The Static Domain is represented in Figure 4.8.

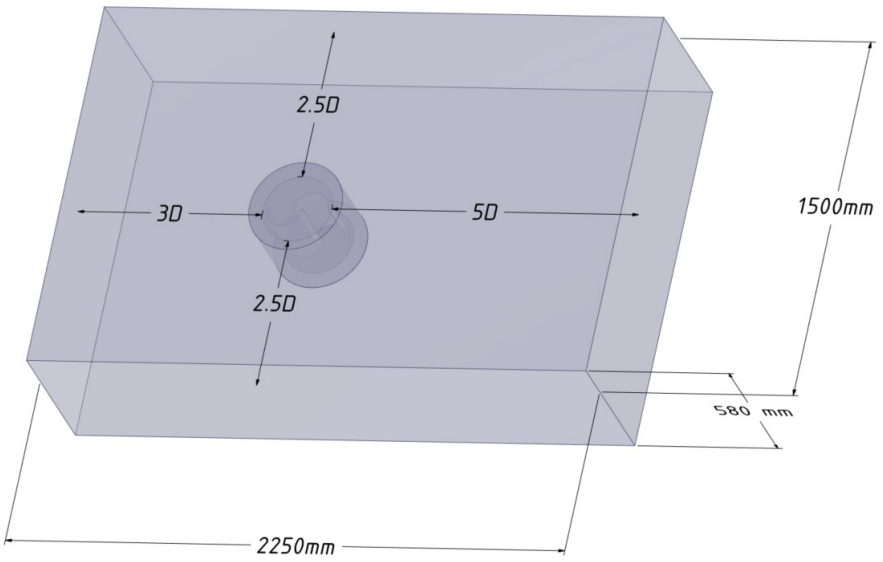


Figure 4.8. CAD Model of Static Domain

The meshing of the Rotational Domain is challenging compared to the channel domain due to the existing curvature of the turbine blades and the small thickness of the blade profiles. Therefore, unstructured tetra/pyramid mesh elements are used along with hex elements. Ansys Mesher provides a number of mesh methods for the meshing process. Along these methods, the MultiZone method is used for the Rotational Domain. The MultiZone method automatically separates the geometry into mappable zones and free zones. Mappable zones are the surfaces where the MultiZone algorithm creates a structured surface mesh to grow on. When the algorithm completely meshes all surfaces of the geometry, it starts to grow mesh cells over the surface meshes to fill the enclosed volume with mesh elements. Due to the existing complex geometry between the surfaces of the Rotational Domain, the enclosed volume is filled with unstructured tetra elements. The blade surfaces and shaft surface are defined as no-slip walls. Therefore, an inflation layer is defined by providing total thickness of the layer. Thus, the algorithm creates a secondary volume for the thickness of the inflation layer, then it fills this volume with structured hex elements. Although the MultiZone method is computationally more expensive

compared to other provided meshing methods, it provides high quality meshes. Moreover, various size controls are applied to the Rotational Domain. Face sizing control is applied over the blade surfaces and the outer cylindrical face to ensure capturing the flow physics over the blades and coherent data transfer between the Rotational Domain and the Static Domain. Sizing methods are not defined for the side circular faces of the Rotational Domain since, the end plates of the turbine limit the flow interactions in these regions. Body sizing control is used to control the sizes of the volume meshes. Generated mesh structure for the Rotational Domain and the inflation layers around the shaft and blade surfaces are presented in Figure 4.9 and Figure 4.10.

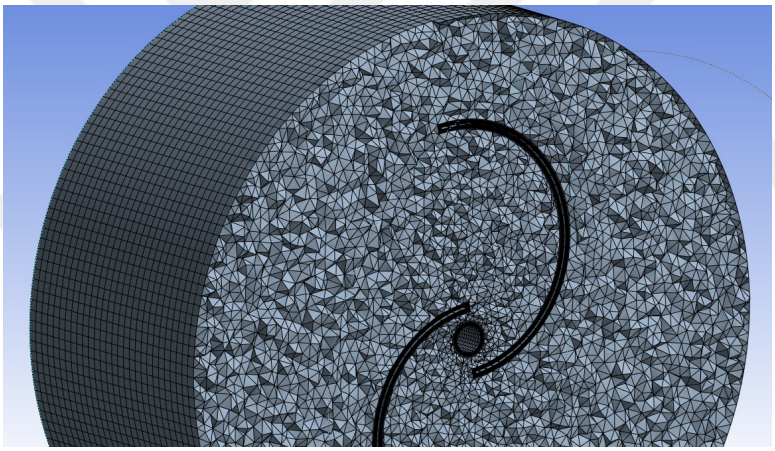


Figure 4.9. Generated Mesh of Rotational Domain

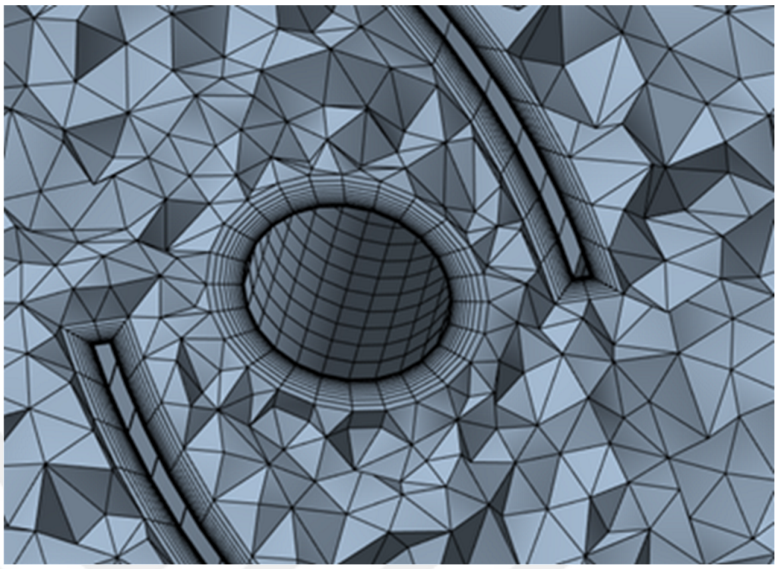


Figure 4.10. Inflation Layer around Shaft and Blades

As seen in Figure 4.10, the surfaces of the blades and shaft are mapped by structured surface mesh, then the algorithm creates layers of structured hex mesh elements up to the thickness of the inflation layer. The void between the inflation layer and the outer surface of the cylindrical domain is then filled by unstructured tetra mesh elements. A mesh growth rate of 1.2 is used for the volume mesh generation.

The Static Domain is meshed by unstructured tetra mesh elements. A face sizing control is applied to the cylindrical face of the inner void and a body sizing control is applied to the whole static domain to control volume mesh generation. The side circular faces of the inner void are not subjected to a mesh sizing method similar to the Rotational Domain. The meshed Static Domain is shown in Figure 4.11. The applied face sizing control on the cylindrical inner face of the Rotational Domain can be observed in Figure 4.12.

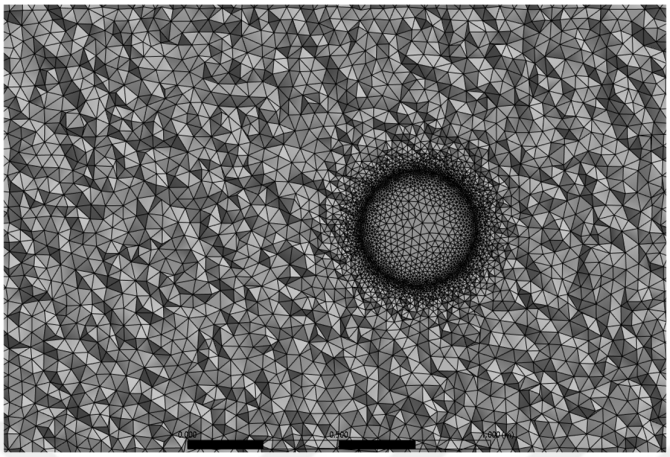


Figure 4.11. Generated Mesh of the Static Domain

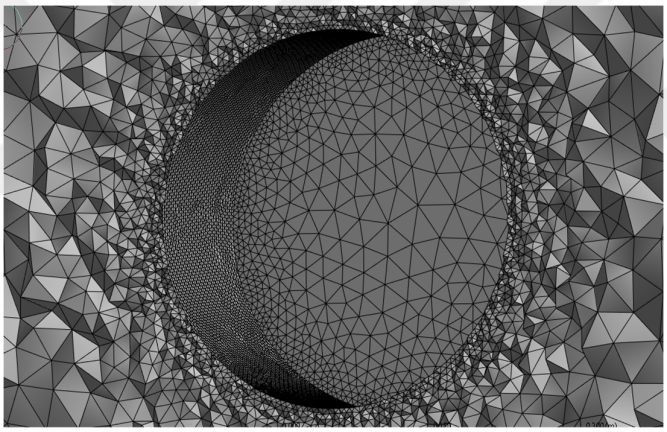


Figure 4.12. Generated Mesh of the Static Domain near Rotational Zone

4.3 Obtaining Inlet Velocity Distribution

The geometry generation and meshing process of the flume is discussed in section 4.2. Pressure-Based solver is used for the steady state simulations of the channel. Coupled scheme is selected as a solution method for the RANS equations due to the robust stability of this scheme for steady state calculations. Top boundary of the channel domain is modelled as symmetry-boundary to simulate a free surface. Side and bottom boundaries of the domain are assigned as stationary no-slip wall. A 0.5 mm evenly distributed wall roughness is applied on the no-slip wall boundaries by

utilizing the Icing Model. The inflation layer over the no-slip wall boundaries is modeled up to 10 times the assigned wall roughness to ensure robustness of the Icing Model. SST k-Ω turbulence model is used to solve viscous sublayer. Therefore, y+ is kept as 1. 0.8 m/s flow velocity is applied at the velocity inlet boundary and gauge pressure of 0 Pa is defined over the pressure outlet boundary. After 20 iterations of the simulation, the velocity distribution at the outlet section is assigned to the inlet section to improve the convergence of the simulation.

The horizontal velocity distribution along the width of the channel at mid-depth and the vertical velocity distribution along the height of the channel at the mid-section is determined. The resulting velocity distributions at the outlet section are presented in Figure 4.13 and Figure 4.14.

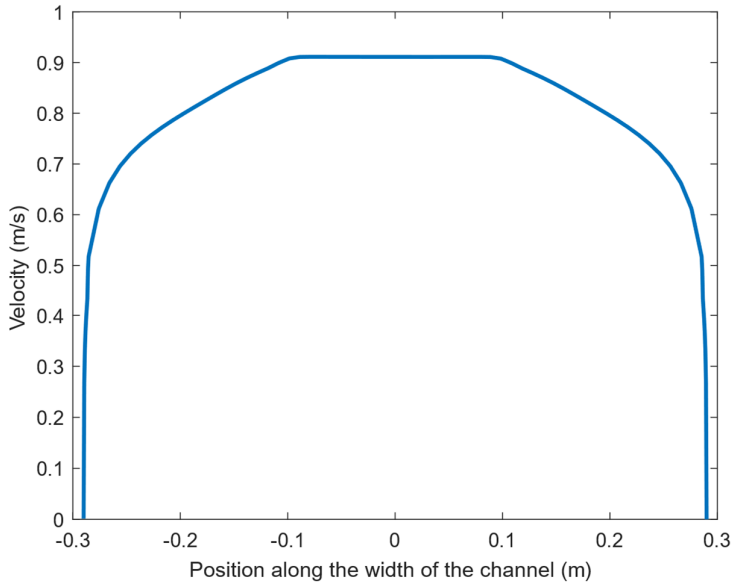


Figure 4.13. Horizontal Velocity Component Distribution

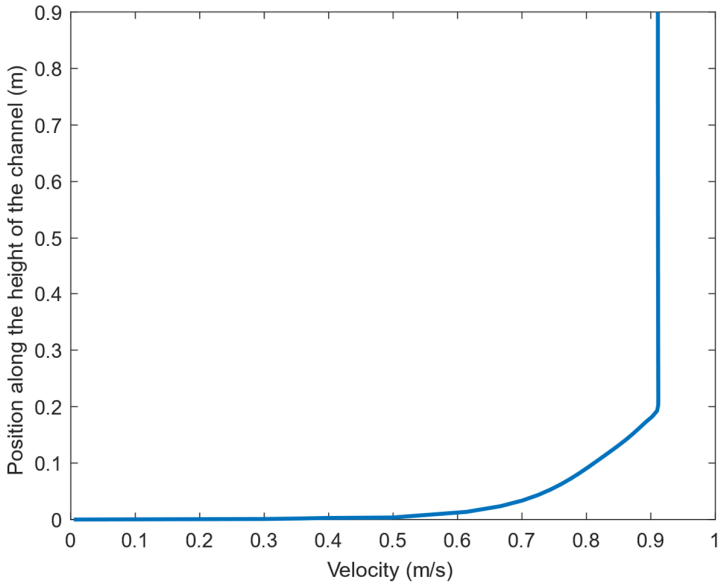


Figure 4.14. Vertical Velocity Component Distribution

The turbine studied in the experimental work of (Talukdar et al., 2018) was placed at the mid depth of the channel. As illustrated in Figure 4.14, the vertical velocity distribution along the height of the channel exhibits a consistent uniformity due to the substantial distance of the bottom wall boundary. In contrast, the side boundaries have a strong influence on the horizontal velocity distribution along the width of the channel, as seen in the Figure 4.13. Therefore, the horizontal velocity distribution is used to define inlet condition for the simulations of the turbine geometry. This approach significantly reduces computational time by eliminating the need to simulate the entire flume for each turbine simulation. Moreover, adopting this velocity distribution as the inlet condition enables the utilization of symmetry boundaries for both the side and bottom faces of the domain; consequently, the inflation layers over the no-slip boundaries are removed. As a result, this refinement helps to reduce mesh number and mesh complexity.

4.4 Numerical Model Development of Turbine Simulations

The transient CFD simulations are used to capture complex flow interactions around the rotating Savonius turbine as discussed in Section 3. The successful numerical model development of the turbine simulations consists of determining the adequate time discretization interval and the grid resolution. Furthermore, the developed numerical model aims to achieve optimal utilization of the available computational resources to ensure a balance between accuracy and efficiency. In order to achieve this balance, a mesh independency study and a time-step independency study are carried out for the development of SHT numerical model.

The transient (i.e. unsteady-state) CFD simulations advances over time-steps; the solution evolves from previous state with each time step. The initial values assigned to the computational domain provide a starting point for the simulations to evolve over time. As a result, the initialization of the computational domain has a significant influence on both the stepwise convergence and overall convergence of a transient CFD simulation. A well-initialized simulation converges faster and more smoothly since the beginning circumstances close to the actual flow conditions. Therefore, the steady-state simulations are conducted for every model before the transient ones and the obtained flow field is used as initial condition for the transient ones. In the steady-state simulations, the moving reference frame modelling option of Ansys Fluent is used to reflect the rotation of the turbine. When the moving reference frame modelling is applied to the rotational domain, RANS equations are modified to include the extra acceleration components caused by the defined rotational motion.

Pressure-Based solver with absolute velocity formulation is chosen for both the steady-state simulations and the transient simulations. Gravitational acceleration is included in RANS equations. As a solution method, Coupled Solver is utilized for the steady-state simulations due to stability of this scheme for the steady state calculations. In the preliminary analysis, utilization of both the Semi-Implicit Method for Pressure Linked Equations (SIMPLE) Solver and the Coupled Solver for the transient simulations are explored. Although the Coupled Solver algorithm

consume more random-access memory (RAM), it achieves convergence faster than the SIMPLE Solver. Therefore, the Coupled Solver is also used for the transient simulations.

In the next sub-sections, Mesh Independence Study and Time-Step Independency Study will be discussed in detail. The obtained adequate mesh sizes and the time interval will be used to validate the numerical model against the experimentally obtained performance data.

4.4.1 Mesh Independence Study

A mesh independence study is one of the key investigations performed in CFD simulations. It aims to determine the influence of grid resolution changes on the simulation results. In this study, the mesh density, especially in the Rotational Domain and the contact region, is systematically increased while the simulation settings discussed in Section 4.4 are kept constant. By gradually increasing the mesh density, this study attempts to determine a level of mesh refinement, which further decrease in mesh sizes has no effect on the converged simulation results. By achieving this level of mesh refinement, this study shows the reliability of the simulations while determining the optimal grid resolution.

Mesh generation for this study is carried out according to the procedure defined in Section 4.2. Six different meshes are generated by gradually decreasing the mesh sizes. The generated meshes are presented in Table 4.2 with the applied mesh sizing controls.

Table 4.2 Generated Meshes

	Blade Surface	Contact Surfaces	Rotational Domain	Static Domain	No. Mesh element
Mesh 1	8.8 mm	8.0 mm	5.2 cm	10.0 cm	917180
Mesh 2	7.0 mm	6.8 mm	4.0 cm	8.0 cm	1246698
Mesh 3	6.5 mm	6.0 mm	3.0 cm	4.0 cm	1495481
Mesh 4	6.2 mm	5.9 mm	2.7 cm	5.0 cm	1562229
Mesh 5	5.7 mm	5.7 mm	2.7 cm	4.0 cm	1726518
Mesh 6	5.2 mm	5.4 mm	2.5 cm	3.8 cm	2279930

The simulations regarding this study are conducted at a TSR of 0.6. The adequate time-step selection is crucial for the success of these simulations. The time-step independence study will be carried after the determination of the optimal grid resolution. Therefore, the time-step that corresponds to 1 degree of rotation of the turbine is selected for the simulations based on the observations made in the literature review. The time-step that corresponds to 1 degree of rotation is 0.004545 sec. Although, y+ of 1 is tried to achieve for all generated meshes, it was not possible to attain this resolution in inflation layer without increasing the growth factor beyond 1.2. Increasing the growth factor beyond this value introduces additional stability problems. Thus, enhanced wall function is utilized for the coarser meshes: Mesh 1 and Mesh 2. The simulation results regarding the generated meshes are presented in Table 4.3 and Figure 4.15. The "Relative Error" column in Table 4.3 presents the discrepancy between the outcomes of consequent mesh refinements levels.

Table 4.3 Resulting C_T and C_P Values of the Meshes in Mesh Independence Study

	C_T	C_P	Relative Error (%)
Mesh 1	0.356	0.214	
Mesh 2	0.340	0.204	4.440
Mesh 3	0.346	0.208	1.827
Mesh 4	0.344	0.207	0.595
Mesh 5	0.344	0.207	0.000
Mesh 6	0.344	0.207	0.000

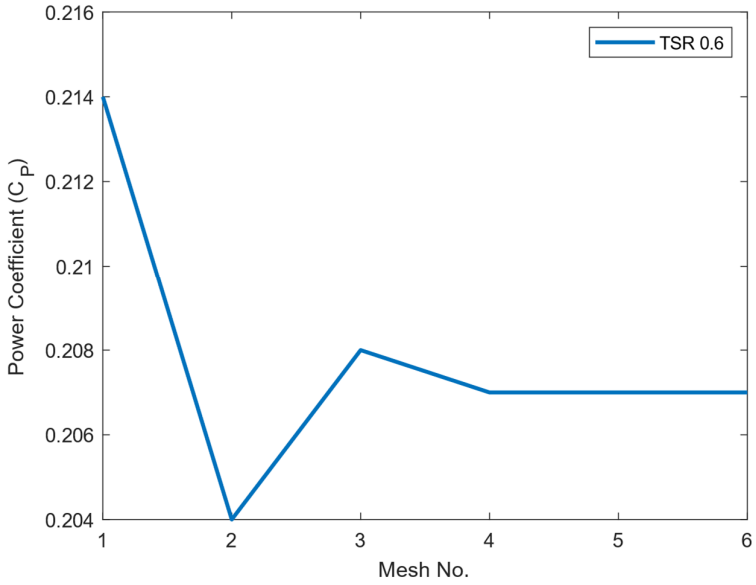


Figure 4.15. Mesh Independence Study

As seen in Table 4.3 and Figure 4.15, further mesh refinement after Mesh 4 does not have an impact on the simulation results. Mesh 4 represents the threshold that indicates the simulation has reached a state of convergence in terms of grid resolution. Therefore, mesh metrics of Mesh 4 are determined as optimal grid sizes and utilized for the simulations regarding the test cases and the validation study. Moreover, the results showed that the simulations reached a quasi-steady state at the 4th rotation of the turbine in terms of energy yield. Thus, adequate number of rotations is decided as 5 for the test case simulations.

4.4.2 Time Step Independence Study

The time step independence study aims to establish an optimal time step size that achieves both precision in results and optimal utilization of computational resources. The time step is critical in capturing transient flow characteristics especially in CFD simulations that involve rotating components such as Savonius Turbines. In such

simulations, complex and rapidly changing flow interactions arise due to the rotation of the blades.

By gradually decreasing the time step size, a value of time step that strikes the right balance is identified. This assures that the simulation output is accurate, represents the transitory dynamics, and computationally efficient. In the performed simulations, the simulations parameters other than the time step size were held constant. The simulations were carried out for a TSR of 0.71. The time step was defined in relation to the degree of rotation of the turbine, reflecting the rotation angle covered in each time step. The results obtained regarding the C_T are presented in Table 4.4 and Figure 4.16. The "Relative Error" column in Table 4.4 presents the difference between the results of successive time-step refinements.

Table 4.4 Resulting C_T Values of Time Step Independence Study

Time Step	Actual Time (sec)	C_T	Relative Error (%)
3º	0.011687	0.356	
2º	0.007792	0.334	6.179
1º	0.003896	0.326	2.365
0.5º	0.001948	0.326	0.000

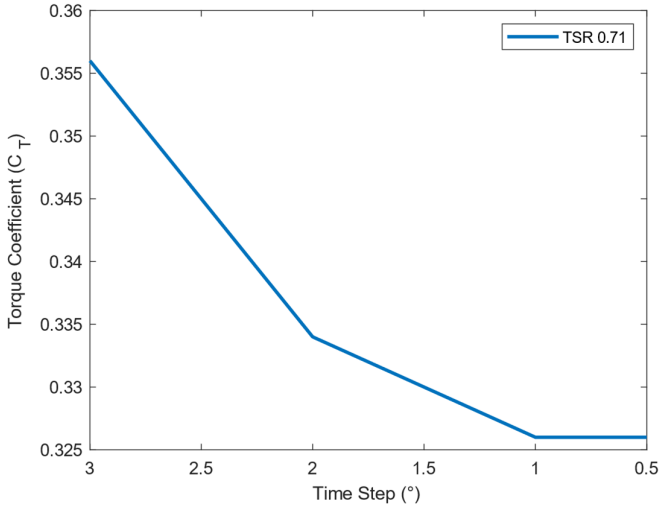


Figure 4.16. Time Step Independence Study

The results indicate that reducing the time step below 1 degree had minimal impact on the simulation outcomes. Therefore, a time step of 1 degree was selected as the optimal choice for the subsequent simulations regarding the test cases and the validation study. This 1-degree time step represents the point where the simulations reached convergence in terms of time discretization. This choice ensures a balanced approach that captures transient dynamics while effectively utilizing computational resources.

4.5 Validation of the Numerical Model of Turbine

This section undertakes a comparison of the simulation results with the experimental data offered by Talukdar et al. (2018) in their publication. The comprehensive description of the experimental study conducted by (Talukdar et al. (2018)) was presented in Section 4.1. This comparison aims to ensure the accuracy, reliability and predictive capabilities of the developed numerical model. The main focus of this thesis is to investigate the performance of the Savonius turbine under various design modifications. Therefore, this validation study employs two important performance parameters: the torque coefficient and the power coefficient to ensure robustness of the comparison.

The numerical model parameters that have been determined and discussed remain constant throughout the validation study simulations. The boundary conditions applied on the outer faces of the numerical domain is shown in Figure 4.17.

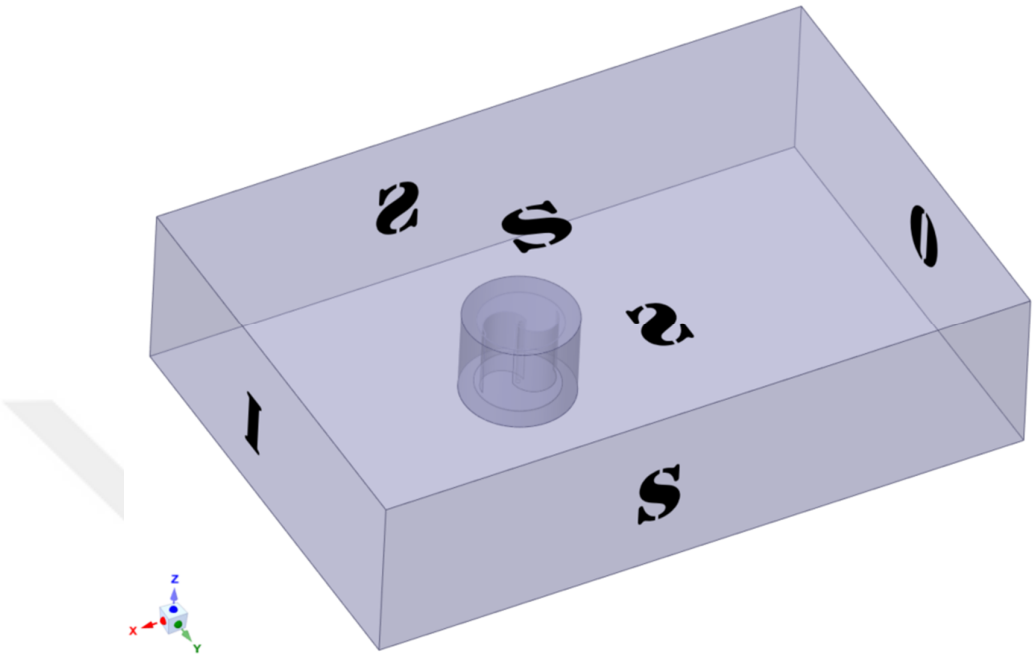


Figure 4.17. Boundary conditions of the numerical model

The top, bottom and lateral boundaries of the numerical domain are treated as symmetry boundaries. Additionally, the inlet and outlet sections are defined as presented in Figure 4.17. The pressure-outlet condition is specified at the outlet boundary as gauge pressure. Simultaneously, the velocity inlet condition is established by utilizing the acquired velocity distribution along the inlet boundary. The gravitational acceleration is set in the negative z-direction to account for the vertical orientation of the turbine in experiments conducted by Talukdar et al. (2018). The numerically obtained results are presented in tabular form in Table 4.5 to facilitate a direct comparison with the experimentally acquired values. The “Error” column in Table 4.5 presents the difference between the results numerical and experimental results.

Table 4.5 Comparison of Numerical and Experimental Results

	Experimental Results		Numerical Results		Error (%)	
TSR	C_T	C_P	C_T	C_P	ε_T	ε_P
0.6	0.3667	0.2200	0.3443	0.2065	6.1	6.1
0.71	0.3521	0.2500	0.3262	0.2315	7.4	7.4
0.8	0.3173	0.2530	0.3041	0.2433	4.2	3.8
0.91	0.2670	0.2430	0.2705	0.2462	1.3	1.3
0.98	0.2449	0.2400	0.2500	0.2450	2.1	2.1
1.1	0.1545	0.1700	0.1481	0.1629	4.2	4.2

The highest relative error observed between the simulation results and the corresponding experimental data is 7.4% at a TSR of 0.71. In contrast, the lowest relative error is measured as 1.3% at a TSR of 0.91. Overall, the results of the developed numerical model demonstrate good alignment with the experimental data, considering the specified precision of ±2.13% in determining C_P in the experiments, as reported by Talukdar et al. (2018). This observation highlights the model's ability to accurately replicate the complex flow patterns surrounding the Savonius turbine. Moreover, the graphical representations of simulation results are shown in Figures Figure 4.18 and Figure 4.19 with the 2D simulation findings obtained by of (Talukdar et al. (2018)).

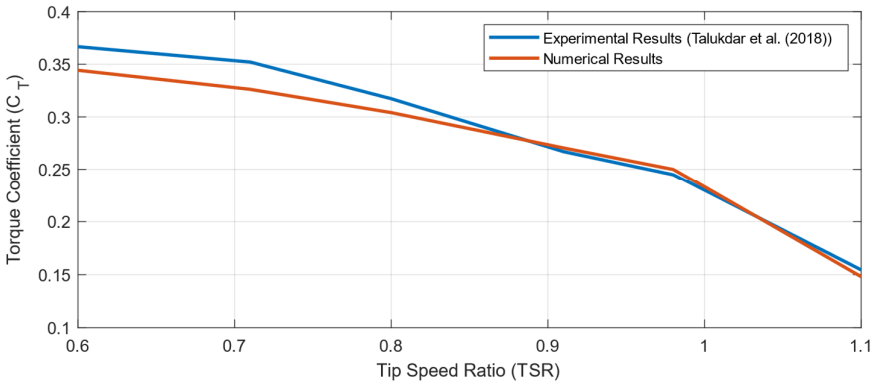


Figure 4.18. Comparison of C_T values

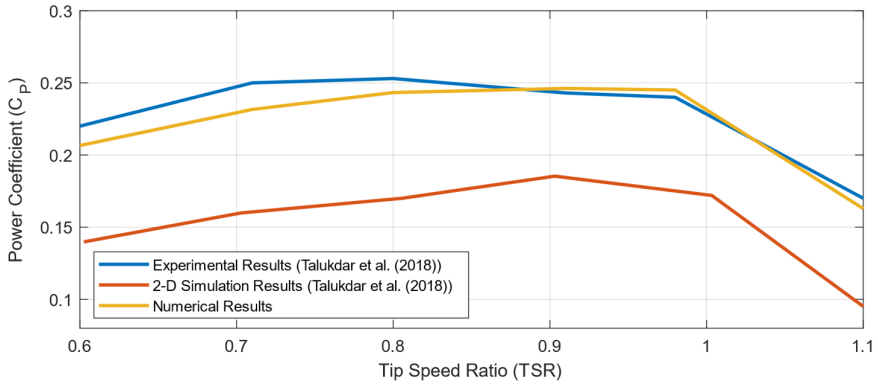


Figure 4.19. Comparison of C_P values

Figure 4.18 and Figure 4.19 also confirm that the simulation is quite reliable in predicting the performance characteristics across a spectrum of TSR values. Additionally, it is noteworthy that the developed numerical model surpasses the predictive capabilities of the 2D simulations conducted by Talukdar et al. (2018). This aspect further increases the model's credibility and underscores its strength in capturing the intricate flow dynamics with high precision.

These results show the developed CFD model is a reliable and accurate tool for forecasting the behavior of the studied SHT model in terms of performance characteristics under various TSR values.

CHAPTER 5

TEST CASE DEFINITIONS

This chapter provides a detailed description of the various test cases that have been developed to evaluate the performance of the Savonius turbine. The test cases have been prepared to cover a wide range of important factors. These parameters include various aspect ratios, varying turbine stacking configurations with distinct phase angles, and a range of blade twist angles. This study seeks to investigate the impact of design adjustments on the overall efficiency of the turbine by carrying out CFD simulations. By conducting these test cases, an extensive understanding of the behavior of the Savonius turbine under various conditions will be acquired, thereby contributing to a full assessment of its operational dynamics and design modifications.

Although the same mesh metrics are used for the newly generated geometries of the test cases, the geometry generation procedure is adapted to incorporate desired design modifications. It is important to point out that the main goal of this thesis is to evaluate the efficiency of the Savonius turbine in river environments. Therefore, the gravitational acceleration is designated in negative y-direction to account for the horizontal orientation of the turbine for all test cases. To ensure consistency with the validation case, identical boundary conditions and simulation configurations are applied throughout all cases.

The following subsections will provide a detailed description of the design modifications undertaken for each test case. Each test case described in these subsections received a unique name due to significant number of the test cases.

5.1 Test Cases: Aspect Ratio

Test cases are formulated to investigate the effect of AR on turbine performance. The turbine model utilized in this study originally has an AR of 1. As discussed in Section 2.3, the expected trend for the efficiency of the Savonius turbine designs is to increase as the AR is increased. Therefore, the AR of the studied turbine design is systematically increased up to a point where the performance increase has reached a stagnation point or exhibit diminishing performance returns compared to increasing AR. The turbine AR is progressively increased by increments of 0.1 up to the maximum AR of 1.9. The aspect ratio is a function of both the diameter and the length of the turbine. In this study, the turbine diameter remains constant and the turbine length is adjusted to achieve the desired AR. To accommodate the extended turbine length, the dimensions of the numerical domain are extended in the horizontal direction by maintaining the 165 mm gap between the endplates of the turbine and the lateral boundaries of the numerical domain. The generated turbine geometries for this test case are detailed in Table 5.1 along with their corresponding design parameters and assigned Test IDs.

Table 5.1 Aspect Ratio Test Cases Turbine Specifications

Test ID	AR	Diameter (mm)	Length (mm)
AR1.0	1.0	250	250
AR1.1	1.1	250	275
AR1.2	1.2	250	300
AR1.3	1.3	250	325
AR1.4	1.4	250	350
AR1.5	1.5	250	375
AR1.6	1.6	250	400
AR1.7	1.7	250	425
AR1.8	1.8	250	450
AR1.9	1.9	250	475

5.2 Test Cases: Turbine Stacking

The goal of these test cases is to study the influence of multi-stage configurations, with variations in phase differences, on the efficiency of the turbine. For multi-stage configurations, both two-stage and three-stage configurations are generated. The AR of the stages are selected as 0.95. Consequently, the ARs of the two-stage configurations and the three-stage configurations are 1.90 and 2.85, respectively. To implement the multi-stage setup, a 3 mm thick middle plate, matching the dimensions of the endplates, is inserted between stages. For the two-stage configurations, phase difference variations ranging from 15° to 90° with increments of 15° are modeled and analyzed. In the case of three-stage configurations, phase differences ranging from 15° to 60° having 15° increments are modeled and analyzed. In order to determine performance comparisons, single-stage counterparts of the two-stage and three-stage turbines are included in the analysis. These single-stage turbines have ARs matching the corresponding multi-stage configurations (AR 1.9 for the two-stage counterpart and AR 2.85 for the three-stage counterpart). Similar to the aspect ratio test case, the distances between the boundaries of turbine's geometry and the boundaries of the numerical domain is constant for this test case as well.

Table 5.2 and Table 5.3 provide detailed information on the generated turbine geometries for multi-stage configurations, including their corresponding design parameters and test IDs. To illustrate the test IDs, the two-stage Savonius Hydrokinetic Turbine having a phase difference of 60° is designated as 2S-SHT-PD60°. It is important to note that the presented phase difference angle of 0° in Table 5.2 and Table 5.3 represents the single-stage counterpart of the relevant multi-stage configuration which serves as a baseline for comparison. The single-stage counterparts of two-stage configuration and three-stage configuration are named as 1S-SHT-PD0°-AR1.9 and 1S-SHT-PD0°-AR2.85.

Table 5.2 Two-stage Test Cases Turbine Specifications

Test ID	Phase Difference	No. Stages	$AR_{turbine}$	AR_{stage}	D (mm)	L (mm)
1S-SHT-PD0°-AR1.9	0 º	1	1.9	-	250	475
2S-SHT-PD15°	15 º	2	1.9	0.95	250	475
2S-SHT-PD30°	30 º	2	1.9	0.95	250	475
2S-SHT-PD45°	45 º	2	1.9	0.95	250	475
2S-SHT-PD60°	60 º	2	1.9	0.95	250	475
2S-SHT-PD75°	75 º	2	1.9	0.95	250	475
2S-SHT-PD90°	90 º	2	1.9	0.95	250	475

Table 5.3 Three-stage Test Cases Turbine Specifications

Name	Phase Difference	No. Stage	$AR_{turbine}$	AR_{stage}	D (mm)	L (mm)
1S-SHT-PD0°-AR2.85	0 º	1	2.85	0.95	250	712.5
3S-SHT-PD15°	15 º	3	2.85	0.95	250	712.5
3S-SHT-PD30°	30 º	3	2.85	0.95	250	712.5
3S-SHT-PD45°	45 º	3	2.85	0.95	250	712.5
3S-SHT-PD60°	60 º	3	2.85	0.95	250	712.5

5.3 Test cases: Blade Twist Angle

These test cases aim to examine the effect of adaptation of twisted blades in the studied SHT on its performance. For these test cases, geometric parameters of the Rotational Domain and Static Domain remained constant. Only the blade geometry of the SHT has changed and other design factors have been kept constant. A helical path is defined depending on the specific blade twist angles. Then, the blade cross-section of the studied SHT swept around this path to generate twisted blades. In Table 5.4, details of the turbines having twisted blades are presented.

Table 5.4 Blade Twist Angle Test Cases

Name	Twist angle	*D* (mm)	*L* (mm)
TWST0°	0 º	250	712.5
TWST15°	15 º	250	712.5
TWST30°	30 º	250	712.5
TWST45°	45 º	250	712.5
TWST60°	60 º	250	712.5
TWST75°	75 º	250	712.5
TWST90°	90 º	250	712.5

CHAPTER 6

RESULTS

This chapter outlines the findings obtained in the scope of this thesis. Before discussing the findings on the test cases, preliminary analyses of the studied model is presented to provide context for understanding both the flow field around the SHT and the subsequent test case results.

The initial part of this analysis discusses the reasons for choosing the horizontal orientation of the turbine. This sets the groundwork for discussions on the static and dynamic performance of the turbine at choosen orientation. Then, the flow field around the SHT will be examined by using pressure contours and velocity contours at specific angles.

Following this, the findings from each test case will be discussed in their dedicated sections. This approach aims to provide a clear and detailed exploration of the results obtained throughout the research.

6.1 Horizontal Orientation of Savonius Turbine

The horizontal orientation of the Savonius turbines offers two different options for turbine placement, differing from the vertical placement. In the vertical alignment, both the advancing and returning blades experience same hydrostatic pressure variation along their surfaces. However, in horizontal configuration, the rotational direction might lead to the exposure of either the returning or advancing blade to higher or lower hydrostatic pressure zones, depending on the direction of the rotation. In Figure 6.1, the possible turbine placements and the associated hydrostatic pressure distributions are shown.

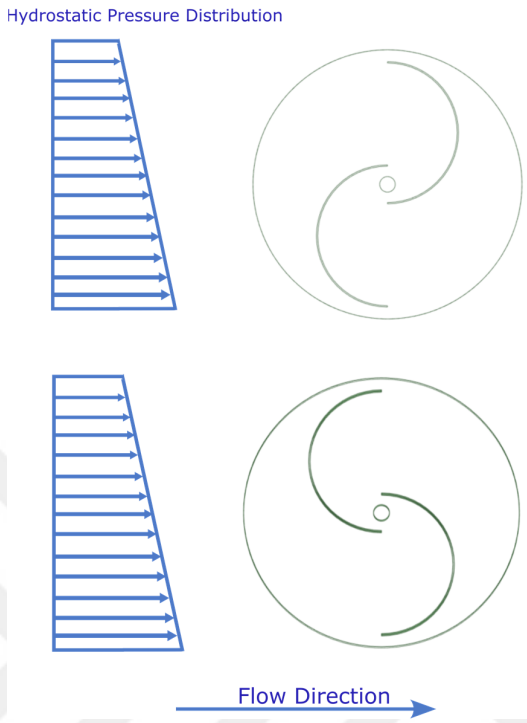


Figure 6.1. Alternative Horizontal Placement of SHT

As seen in Figure 6.1, a horizontal axis Savonius Turbine can rotate in both counterclockwise and clockwise directions for the given flow direction. In a clockwise rotation, the returning blade is subjected to a higher hydrostatic pressure zone. In contrast, the advancing blade is exposed to a higher hydrostatic pressure zone in a counterclockwise rotation. It is important to analyze both rotational directions to determine the favorable placement for horizontal orientation.

The validated numerical model was run for both directions to assess the favorable placement for horizontal orientation. The gravitational acceleration was set in the negative y-direction to account for the horizontal orientation of the turbine. The C_T values obtained are presented in Table 6.1 and obtained C_P values are presented in Table 6.2. The "Higher Pressure" column in both tables corresponds to results of the rotational direction where the advancing blade experiences higher hydrostatic pressure, while the "Lower Pressure" column represents results of the rotational direction where the advancing blade is in a lower hydrostatic pressure zone.

Table 6.1 Comparison of Resulting C_T for the Alternative Placements of SHT

TSR	High Pressure	Lower Pressure	Difference (%)
0.6	0.3443	0.3438	0.1281
0.7	0.3269	0.3266	0.1157
0.8	0.3002	0.3003	-0.0245
0.9	0.2710	0.2696	0.5214
1	0.2413	0.2405	0.3072
1.1	0.1477	0.1478	-0.0719

Table 6.2 Comparison of Resulting C_P for the Alternative Placements of SHT

TSR	High Pressure	Lower Pressure	Difference (%)
0.6	0.2066	0.2063	0.1281
0.7	0.2289	0.2286	0.1157
0.8	0.2402	0.2402	-0.0245
0.9	0.2439	0.2426	0.5214
1	0.2413	0.2405	0.3072
1.1	0.1625	0.1626	-0.0719

While some minor performance losses are observed for the TSR of 0.8 and 1.1, overall, the turbine exhibited slightly better torque and power generation performance when the rotation of the turbine is arranged to place advancing blade into higher hydrostatic pressure zone, according to the findings presented in Table 6.1 and Table 6.2. The highest performance improvement is observed on TSR of 0.9 as 0.52%. Even though this performance improvement is quite small, configuring the turbine to place the returning blade in the higher-pressure zone offers an effortless improvement in torque generation and power generation capacity. Additionally, the turbine model studied has a diameter of only 25 cm which results in very low-pressure variation across the diameter. Therefore, this effect may lead to more significant performance improvements for turbines with larger diameters.

Based on the findings presented in Table 6.1 and Table 6.2, the rotational direction of the turbine is arranged to place the advancing blade in the higher hydrostatic pressure zone for all remaining simulations in this thesis.

6.2 Performance Characteristics of the Horizontally Positioned Savonius Turbine

The performance characteristics of the validated model under horizontal axis flow condition is presented in this section. Based on the preliminary analysis regarding the horizontal placement of the Savonius turbine, the Savonius turbine is positioned horizontally to locate the advancing blade in the higher hydrostatic pressure zone. In order to examine the self-starting capability of the studied model, the developed numerical model was run for stationary positions at azimuthal angles range from 0º to 180º by 15º increments. For these simulations, unsteady simulations was employed to capture dynamic and transient behaviors. Furthermore, the numerical model was run for TSR values of 0.6, 0.7, 0.8, 0.9, 1.0 and 1.1 to analyze the turbine's rotational performance.

6.2.1 Self-starting Characteristic of the Benchmark Model of Savonius Turbine

The results of the conducted static torque analysis are presented Figure 6.2. The average static torque co-efficient ($C_{T,static}$) is calculated based on Eqn. 3. Although Eqn. 3 is defined for the calculation of C_T over the rotation of the turbine, it is also applicable for the static case by substituting T_{out} in Eqn. 3 with the obtained torque values.

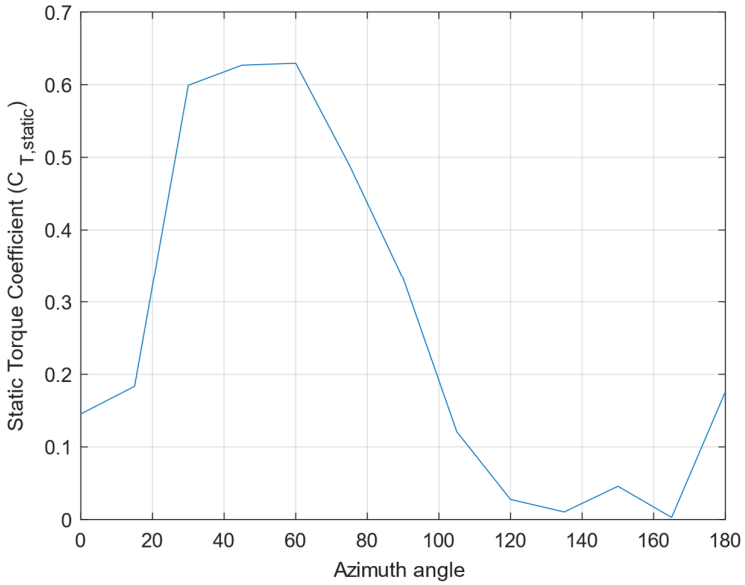


Figure 6.2. Static Torque Analysis of the Horizontally Positioned SHT

The distribution of the $C_{T,\,static}$ shows cyclic behavior over every 180º and exhibits large variations. The maximum $C_{T,\,static}$ values are obtained at azimuth angles of 60º and 45º as around 0.625. The obtained $C_{T,\,static}$ at 60º is slightly larger than the value obtained at 45º. The minimum $C_{T,\,static}$ value is obtained at 165º as 0. A secondary peak in generated static torque values is also observed at 150º. Overall, the studied Savonius turbine can self-start at any given angle since it generates positive torque over the azimuth angles except the 165º. However, the turbine behaves like an inverted pendulum at an azimuth angle of 165º since any small rotational disturbance from this position will also result in generation of positive torque as seen in Figure 6.2.

The obtained $C_{T,\,static}$ distribution was also compared with the finding of (Hayashi et al., 2005; Kamoji et al., 2009a). Both (Hayashi et al., 2005; Kamoji et al., 2009a) experimentally studied Savonius Turbine for wind energy applications for various Re and inlet velocities in their respective research. The findings of (Hayashi et al., 2005; Kamoji et al., 2009a) regarding the static torque generation indicate that changes in Re (i.e., inlet velocity) has only marginal effects on generated $C_{T,\,static}$.

While this was the case regarding the variation in Re, to facilitate a more meaningful comparison, the results from cases with Reynolds numbers similar to that of the studied model, which is 200,000, are utilized. Therefore, the findings of (Hayashi et al., 2005; Kamoji et al., 2009a) regarding the static torque coefficient at Re of 200 00 and 150 000, respectively, are used for the comparison of obtained distributions, aligning with the Re of the studied model in this thesis. The comparison of the $C_{T,\ static}$ distributions are presented in Figure 6.3.

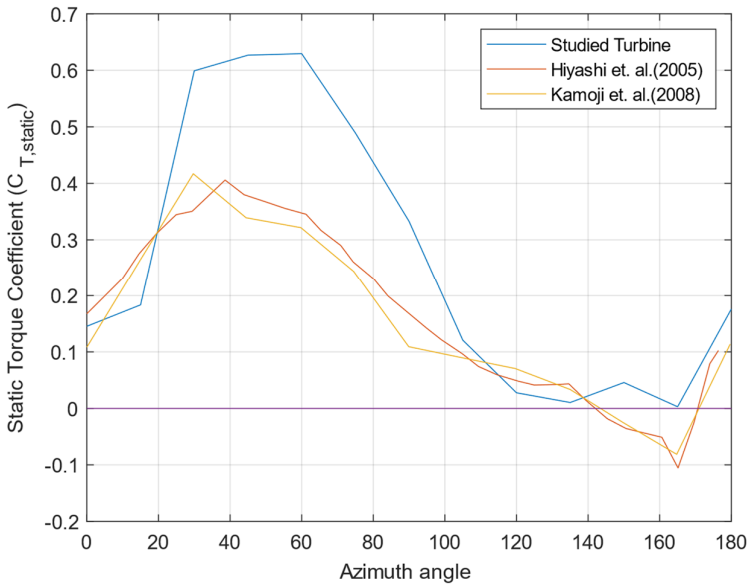
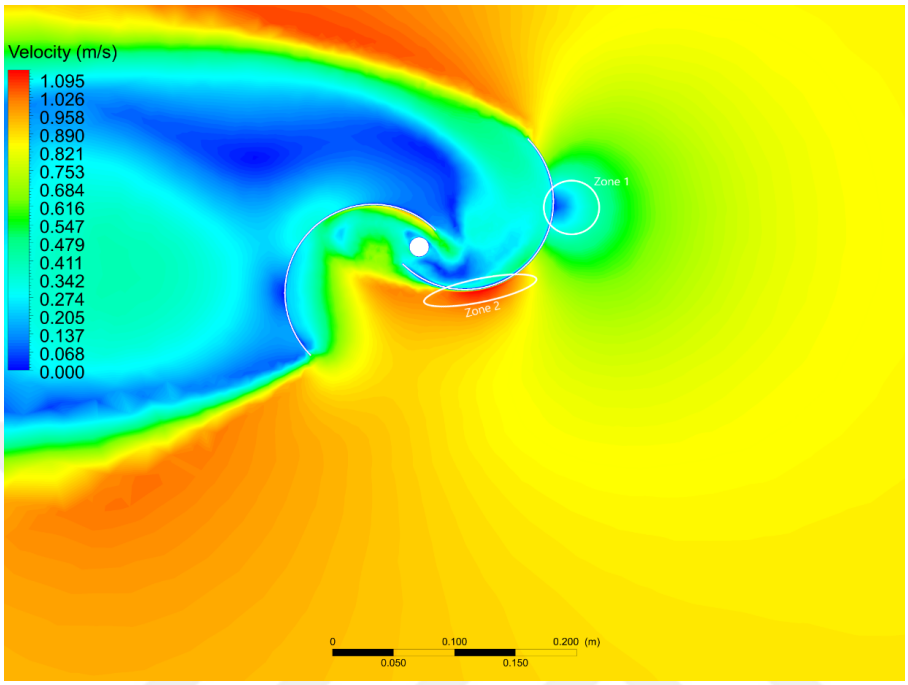


Figure 6.3. Comparison of Static Torque Coefficients

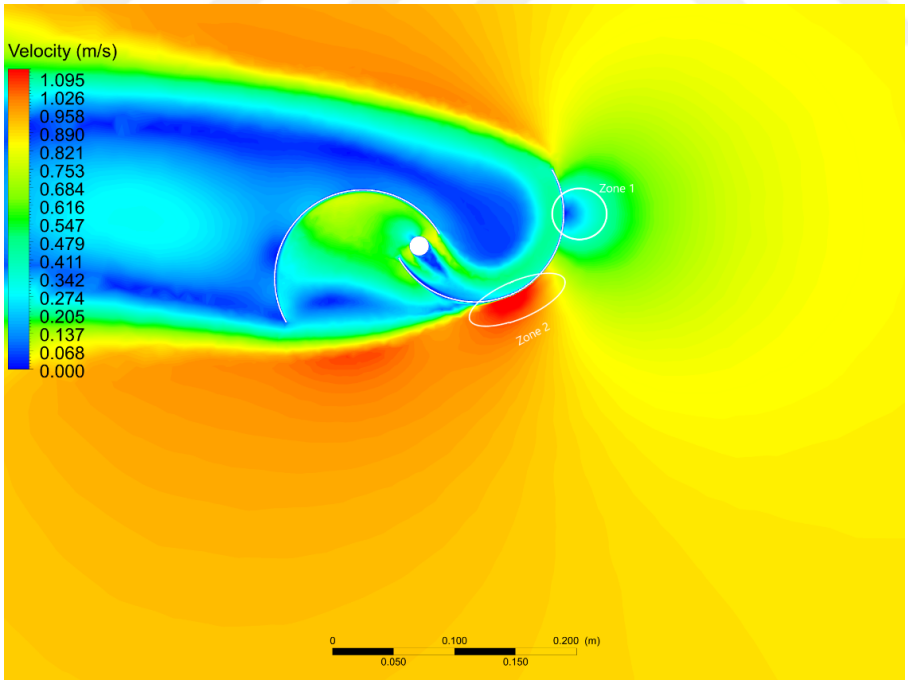
Figure 6.3 provides valuable insights into the self-starting characteristics of Savonius turbines in different flow media. As seen in Figure 2, the Savonius turbine exhibits superior self-starting characteristics in water flows when compared to the wind flows. While the Savonius wind turbines investigated by (Hayashi et al., 2005; Kamoji et al., 2009b) demonstrate an inability to generate positive torque between azimuth angles of 140-170, the hydrokinetic Savonius turbine has the ability to generated positive torque at every azimuth angle. The minimum $C_{T,\ static}$ values are consistently obtained for all three turbines at an azimuth angle of 165º. The

maximum $C_{T,\ static}$ values are observed for (Hayashi et al., 2005; Kamoji et al., 2009a)'s models at azimuth angles of 40º and 30º, respectively. (Hayashi et al., 2005) also reported a small secondary peak in generated static torque values at azimuth angle 135º, although much smaller in magnitude, similar to the observation made at azimuth angle 150 degrees for the benchmark model of SHT.

The observed increase in generated static torque at 150º is worth further investigation. In order to understand the underlying flow mechanism causing the observed peek, the velocity contours and pressure contours of azimuth angles of 135º and 150º are presented in Figure 6.4 and Figure 6.5, respectively. In both Figure 6.4 and Figure 6.5, the flow direction is from right to left on the page.

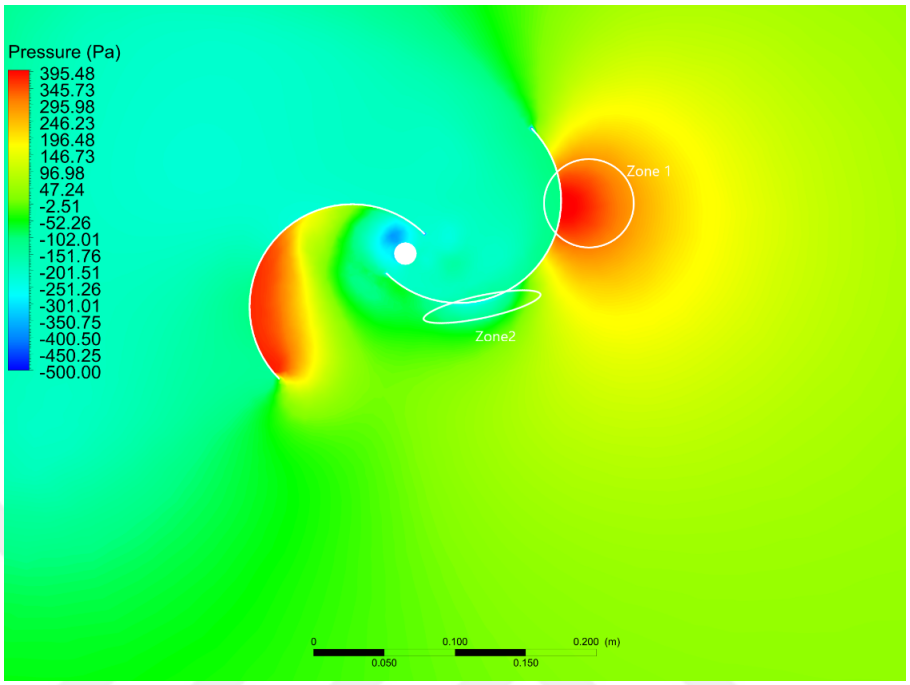


a)

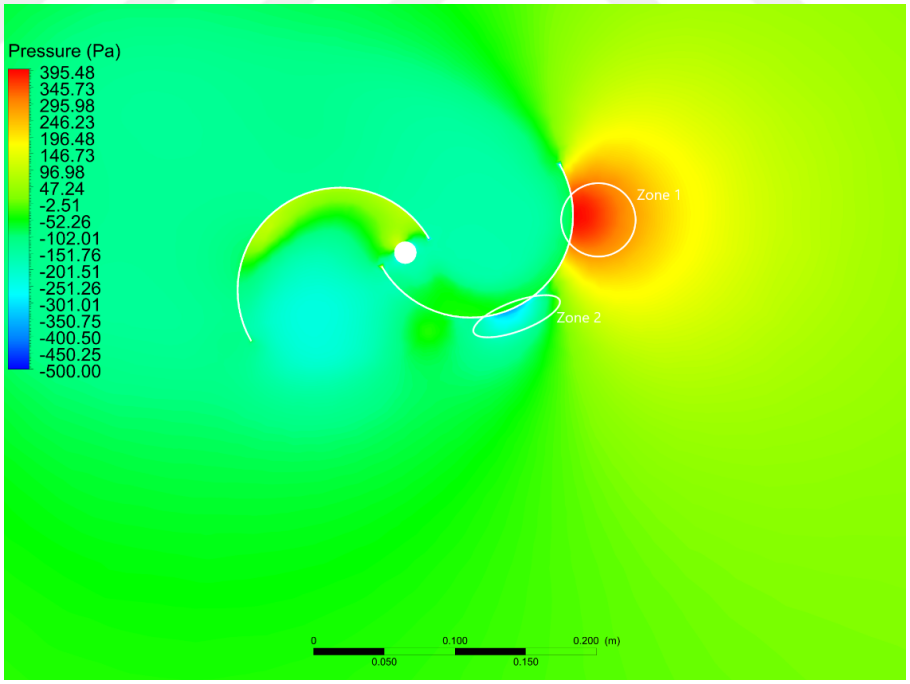


b)

Figure 6.4. Velocity Contours at Azimuth Angles of a) 135 and b) 150



a)



b)

Figure 6.5. Pressure contour at Azimuth Angles of a) 135 and b) 150

When the flow encounters the convex side of the returning blade at these large azimuth angles, two different flow zones emerge. Near the outer tip of the returning blade, the angle between the flow direction and the surface normal of the blade profile is very small. Therefore, in this zone, the blade wall effectively acts like a vertical surface which causes a drastic reduction in flow velocity as shown in Figure 6.4 and marked as Zone 1. Consequently, the pressure within this zone increases, leading to increased moment transfer from fluid flow to blade wall which is shown in Figure 6.5, marked as Zone 1.

In contrast, the angle between the surface normal and the flow increases at around the mid-section of the semicircular blade. This section of the blade behaves like the top surface of an airfoil which results in increased fluid velocity within this region as can be seen in Figure 6.4, marked as Zone 2. A pressure drop occurs on this zone due to increased velocity over the surface, which is illustrated in Figure 6.5 marked as Zone 2.

At an azimuth angle of 135º, the returning blade experiences larger velocity reduction in Zone 1 compared to the azimuth angle of 150º as seen in Figure 6.4. Consequently, the fluid flow generates higher pressure in Zone 1 at the azimuth angle of 135º as seen in Figure 6.5. At an azimuth angle of 150º, the velocity increase observed on Zone 2 is more intense than that of the azimuth angle of 135º as illustrated in Figure 6.4. Therefore, a significantly larger pressure drop occurs at this region for the azimuth angle of 150º as shown in Figure 6.5. Additionally, the location of the occurrence of these zones is important for the generated static torque values.

As shown in Figure 6.5, the horizontal distance between the rotational axis of the turbine and the location of the Zone 2 is larger at the azimuth angle of 150º. Therefore, the formation of Zone 2 results in larger positive torque generation for an azimuth angle of 150º. Furthermore, the flow is effectively re-directed by the gap between the shaft and the advancing blade towards the concave side of the returning blade at the azimuth angle of 150º as seen in Figure 3. This redirected flow

significantly reduces the pressure difference between the concave and the convex sides of the returning blade as shown in Figure 6.4b. This reduction in this pressure difference enhances the turbine's torque generation capacity at the azimuth angle of 150º. Although the advancing blade of the turbine experiences significantly larger pressure at azimuth angle of 135º as shown is Figure 6.5a, due to aforementioned flow mechanics, the turbine at azimuth angle 150º generated larger $C_{T,\,static}$ value.

6.2.2 Rotational Performance of the Benchmark Model

The results of the analysis concerning the benchmark model's rotational power generation and torque generation across TSR values of 0.6, 0.7, 0.8, 0.9, 1.0, 1.1 are presented in Figure 6.6 and Figure 6.7, respectively in terms of C_T and C_P.

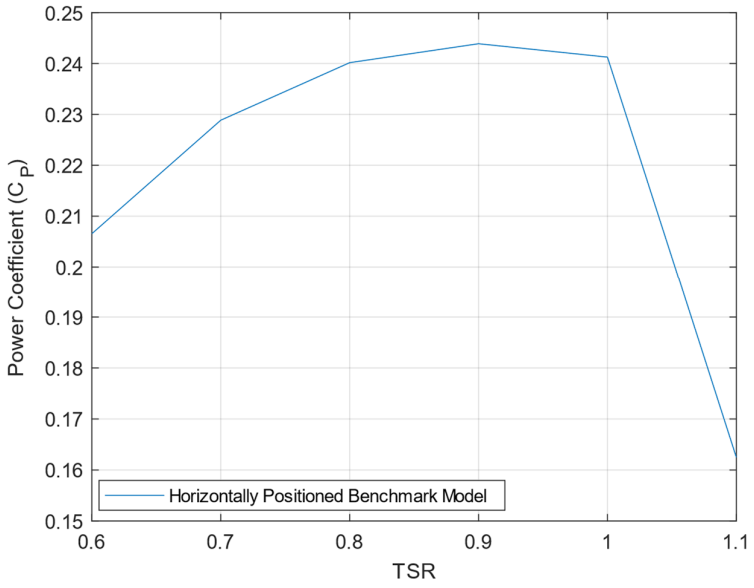


Figure 6.6. C_P Generation Curve of the Horizontally Positioned SHT

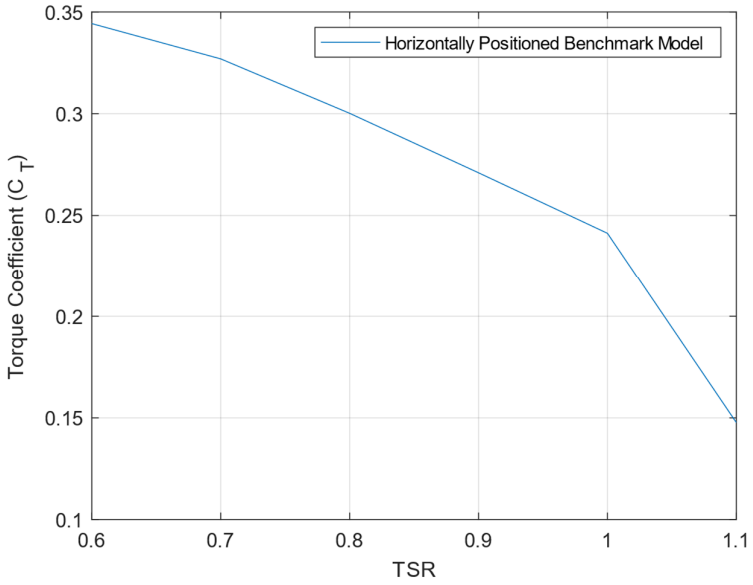


Figure 6.7. C_T Generation Curve of the Horizontally Positioned SHT

As can be seen in Figure 6.6, the highest C_p is achieved at TSR of 0.9. The highest C_T is obtained at TSR of 0.6, as seen in Figure 6.7. The turbine experiences drastic reduction in power generation beyond a TSR value of 1.0 as evident in Figure 6.6. The observed reduction in power generation can be explained by the change in relative velocity of the flow over the advancing and returning blades. At TSR values above 1.0, the relative velocity of the flow over the returning blade increases while the relative velocity of the flow over the advancing blade decreases. Consequently, there is an increase in drag force generated over the returning blade which is coupled with a decrease in drag force generated over the advancing blade. Therefore, the turbine starts to experience significant reduction in power generation capability at TSR values exceeding 1.0. Moreover, a decreasing trend in C_T is also observed as over TSR values increases. Similar to the explanation given concerning power generation, the increase in TSR reduces the relative velocity of the fluid flow over the advancing blade while increasing it on the returning blade surfaces which results in a decreasing trend in torque generation.

The torque generation of the turbine throughout a single rotation of the turbine for various TSR values are presented in Figure 6.8.

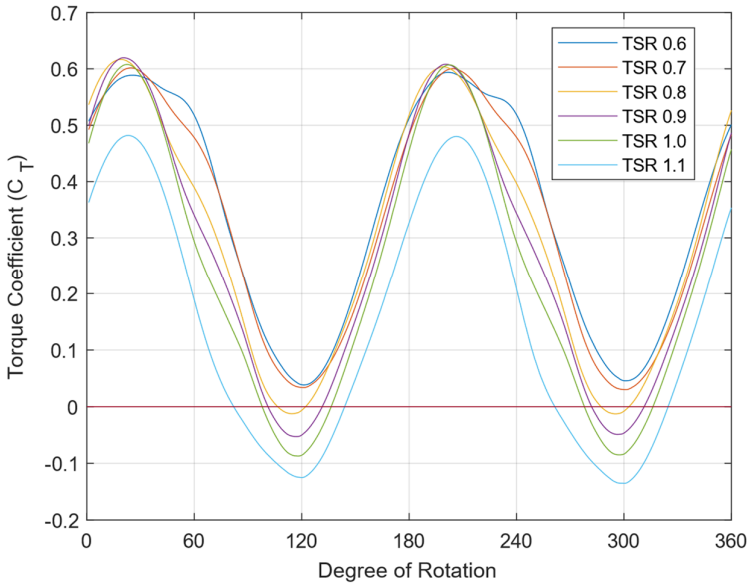


Figure 6.8. C_T Generation over a Single Rotation of the Horizontally Positioned SHT

According to the data presented in Figure 6.8, the turbine exhibits negative torque values at certain rotational degrees when the TSR exceeds 0.7. It also indicates that the increase in rotational velocity leads to a greater negative torque production.

The horizontal placement of the turbine is disscused in Section 6.1 with details. As stated in Section 6.1, the rotational direction of the turbine is strategically arranged to place the advancing blade within the region of higher hydrostatic pressure. In order to compare the performance of this combination and the vertically placed turbine, the numerical model of the validation case is re-run for TSR values of 0.6, 0.7, 0.8, 0.9, 1.0, 1.1. The obtained results are provided in Table 6.3. Table 6.3 also presents the comparison of the generated C_{PS} of horizontally and vertically placed turbines at various TSR values.

Table 6.3 Comparison of Vertical Axis Turbine and Horizontal Axis Turbine, C_P

TSR	Horizontal Axis	Vertical Axis	Performance Difference (%)
0.6	0.2066	0.2066	0.00
0.7	0.2289	0.2286	0.12
0.8	0.2402	0.2402	0.00
0.9	0.2439	0.2439	0.01
1.0	0.2413	0.2413	0.00
1.1	0.1625	0.1625	0.00

As Table 6.3 demonstrates, the vertical alignment shows nearly identical power generation capacity as the horizontally placed configuration where the rotational direction arranged to place advancing blade in higher hydrostatic pressure zone. However, this also indicates that the vertical placement of the turbine exhibited slightly better power generation performance than the scenario where the rotation of the turbine is configured to place the advancing blade into the lower hydrostatic pressure zone, considering the findings presented in Section 6.1 (Table 6.2).

6.3 Evolution of the Flow Field

The understanding of the flow field evolution around the Savonius hydrokinetic turbine is an important aspect of understanding the performance effects of the evaluated test cases. This section provides a brief description of the flow patterns around the rotating Savonius turbine.

Pressure contour and velocity contour at the mid-section of the turbine at 0º is presented in Figure 6.9.

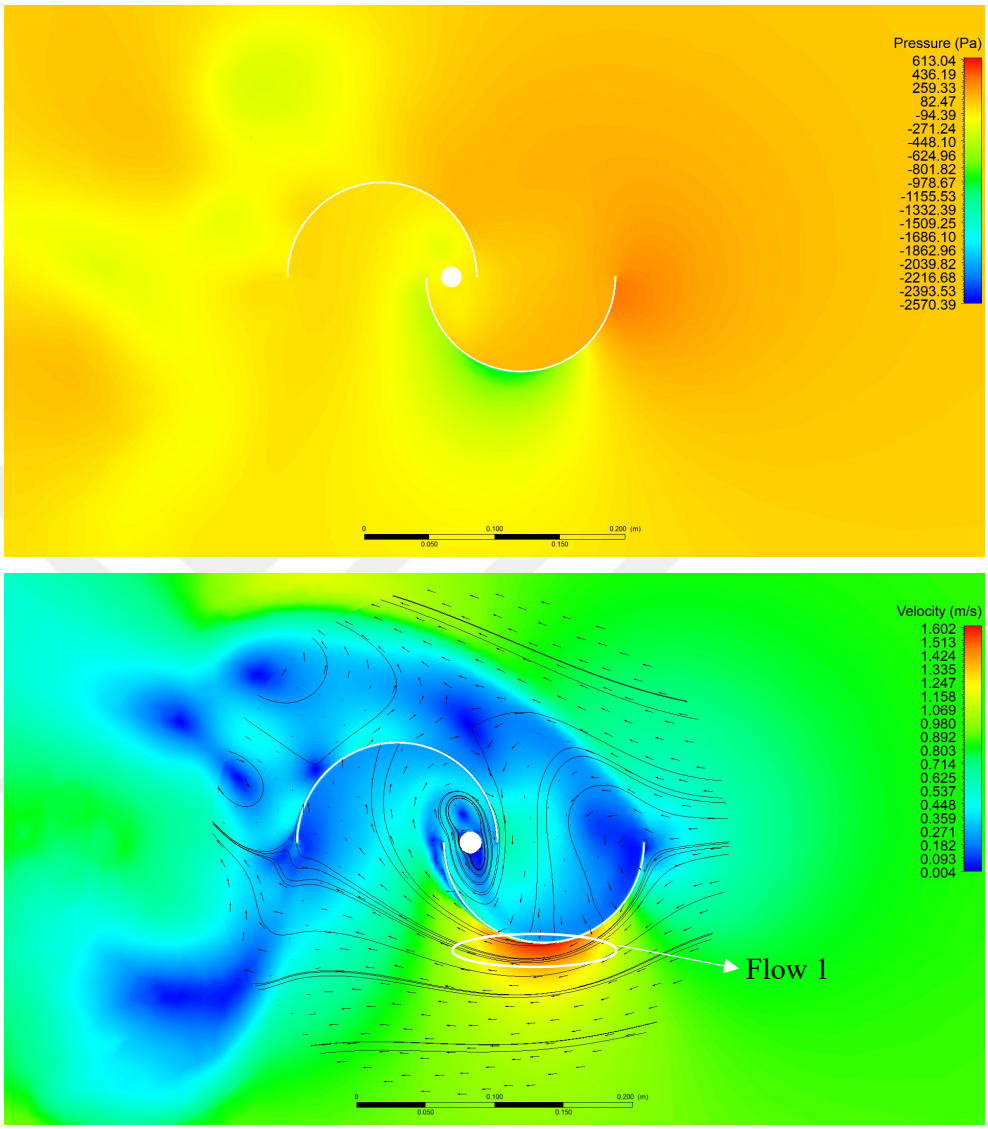


Figure 6.9. Pressure contour (Top) and Velocity contour (Bottom) at 0°

At 0°, the fluid flow initially strikes the right tip of the advancing blade, and then spreads to both concave and convex sides of the advancing blade. Along the convex side of the advancing blade, Coanda-like effect occurs, which causes the flow to follow the curvature of the blade profile. This is illustrated as 'Flow 1' in Figure 6.9 (bottom). As Flow 1 follows the curvature of the blade, a portion of the flow is directed to the concave side of the returning blade which helps to increase the pressure at that side. Simultaneously, due to this Coanda-like effect, the convex side

of the advancing blade behaves like the top section of the airfoil profile which results in reduced pressure on the convex side, as can be seen in Figure 6.9 (Top). Both effects of the Flow 1 contribute to positive torque generation at 0°.

Pressure contour and velocity contour at the mid-section of the turbine at 45º are presented in Figure 6.10.

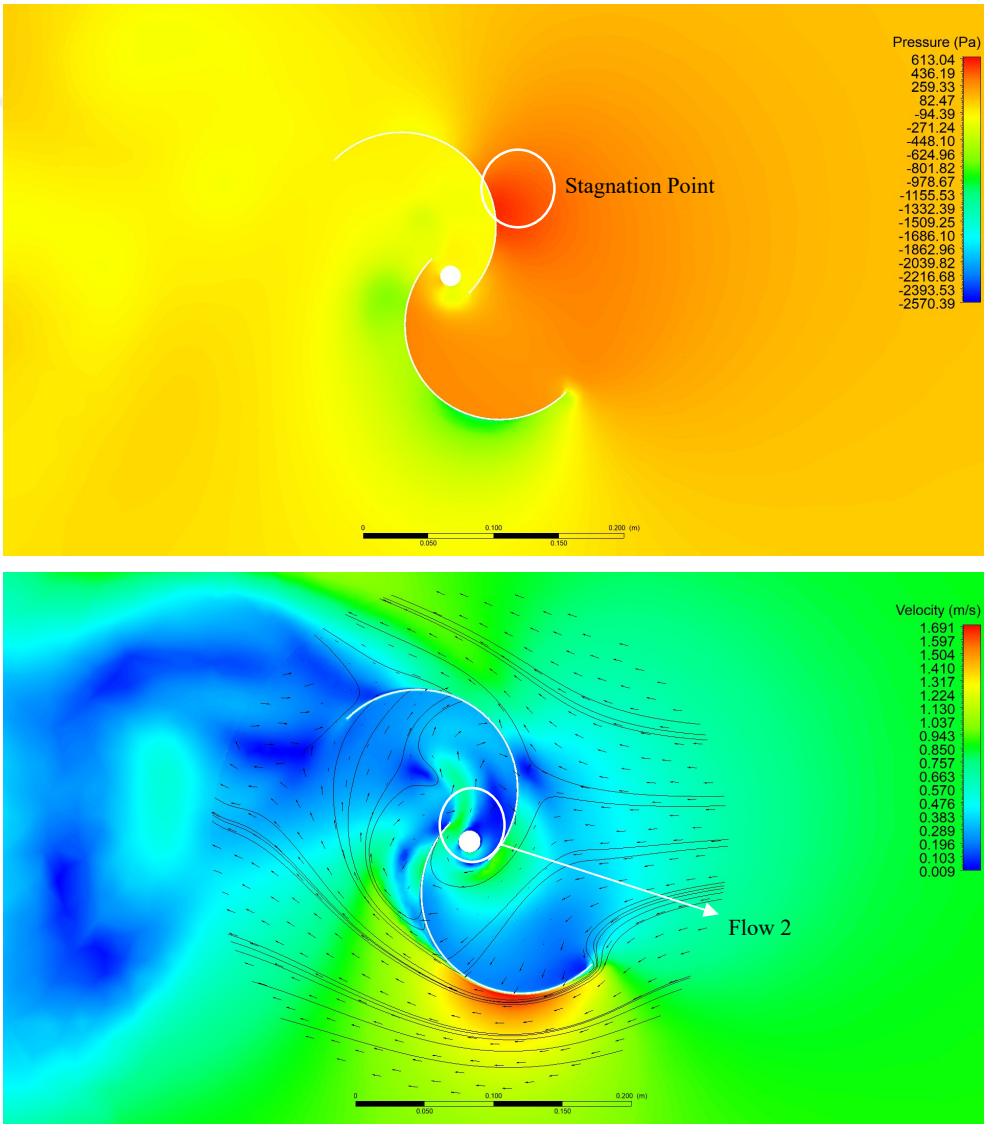


Figure 6.10. Pressure contour (Top) and Velocity contour (Bottom) at 45°

At 45°, a stagnation point emerges on the returning blade and some portion of the flow is directed to concave side of the advancing blade. At this stagnation point, the pressure on the returning blade significantly increases, which causes a significant negative torque on the turbine. The flow from the convex side of the returning blade and the concave side of the advancing blade is redirected by the gap between the shaft and blades to concave side of the returning blade, shown as “Flow 2” in Figure 6.10 (Bottom). The pressure in the concave side of the advancing blade increases as the flow hits to surface of the blade. Due to this increase in pressure in that zone, a portion of the flow cannot enter at the lower tip of the advancing blade which reduces the overall performance. The flow pattern “Flow” 1 can still be observed at 45° of the rotation of turbine and it restores the pressure at the concave side of the returning blade.

Pressure contour and velocity contour at the mid-section of the turbine at 90º are presented in Figure 6.11.

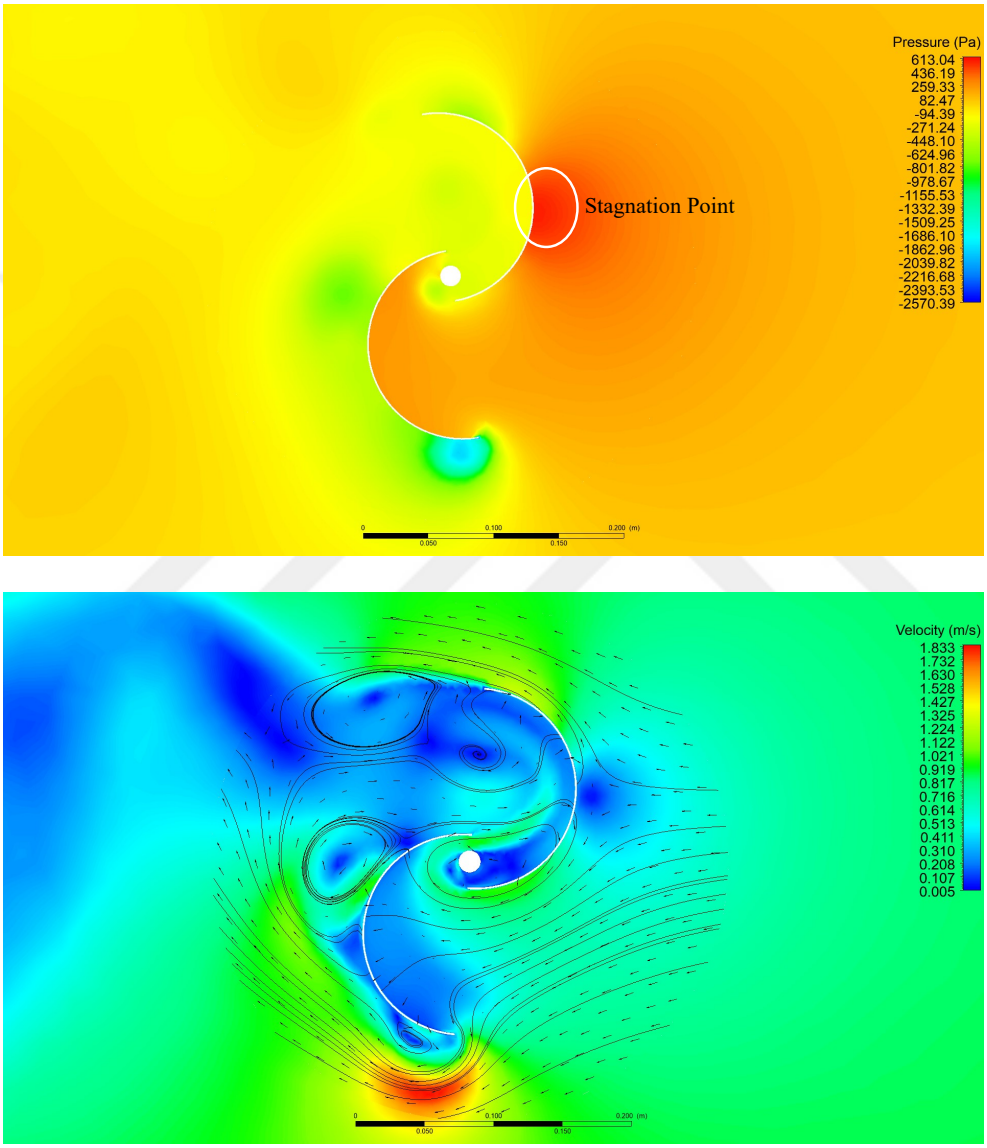


Figure 6.11. Pressure contour (top) and Velocity contour (bottom) at 90°

At 90°, a larger stagnation point occurs on the convex side of the returning blade and the turbine experiences larger negative torque due to increased pressure on the surface. The intensity of the “Flow 2” increases at this angle, which helps restore the

pressure behind the returning blade. A shedding vortex emerges at the tip of the advancing blade, which decreases pressure at the tip and prevents flow to enter concave side. At 90°, “Flow” 1 is diminished and as a result, the back of the turbine is shielded from the flow. This leads to formation of large vortices that reduce the turbine's performance.

Pressure contour and velocity contour at the mid-section of the turbine at 135º are presented in Figure 6.12.

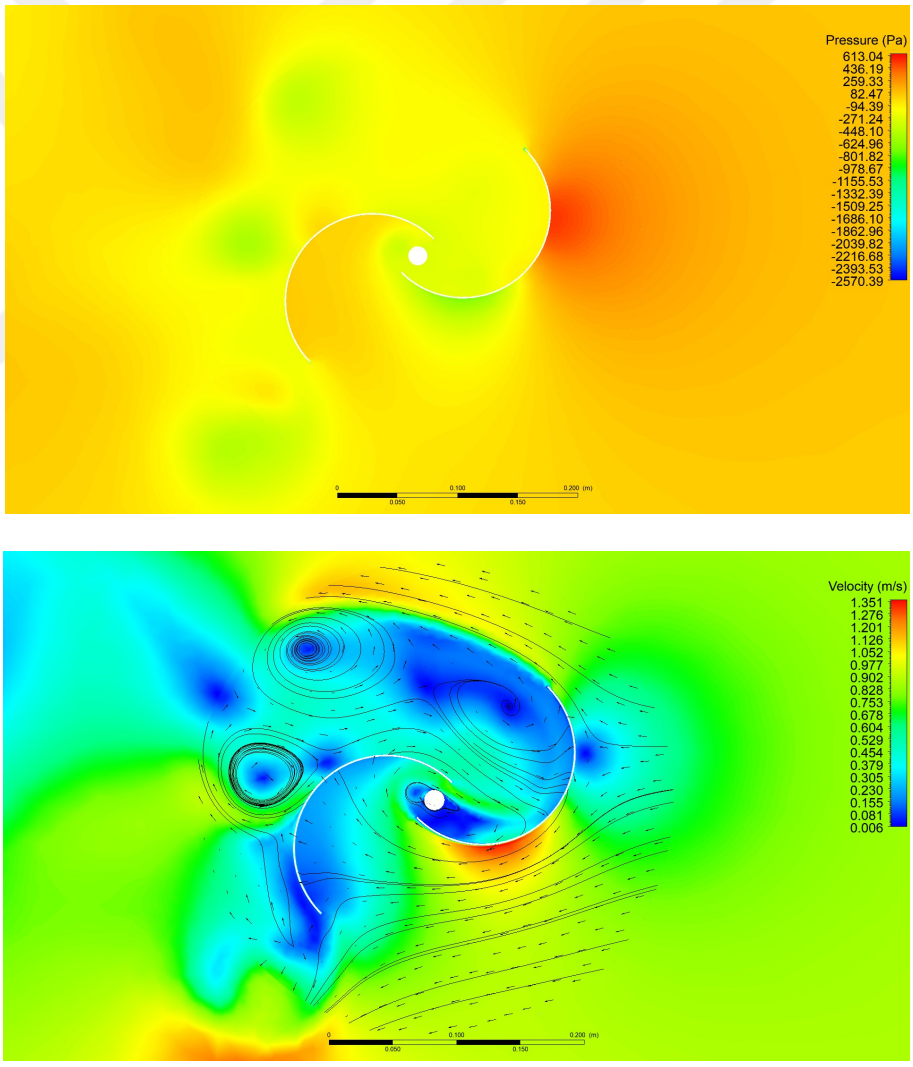


Figure 6.12. Pressure contour (top) and Velocity contour (bottom) at 135°

At 135°, the fluid flow firstly strikes the convex side of the returning blade and "Flow 1" emerges on returning blade (Figure 6.12 4 Bottom). "Flow 1" directs the flow into the concave side of the advancing blade and improves torque generation. The tip vortex is detached from the tip of the advancing blade at this angle. Moreover, the pressure at the concave side of the advancing blade is significantly reduced; therefore, torque generation of the turbine deteriorates. The pressure restoring effect of the "Flow 2" is significantly reduced at this angle and a vortex emerges near the shaft surface.

6.4 Results: Aspect Ratio

This section illustrates the findings of investigation on the effect of the increasing AR on the performance of the studied SHT model. The performances of the SHTs with different ARs are presented in terms of C_T and C_P. Then, the effect of the increasing AR on the evolution of the flow field around the SHT is presented and discussed. The specifications for the AR configurations are outlined in in Section 5.1. Additionally, the designated test IDs provided in Section 5.1 are used to refer the respective AR configuration throughout the ongoing discussions in this section.

6.4.1 Performance Analysis of the AR Configurations

The results of the studied SHTs with ARs varying from 1.0 to 1.9 are compared for TSRs ranging from 0.6 to 1.1. Figure 6.13 illustrates the variation of average C_T over studied TSRs for all ARs.

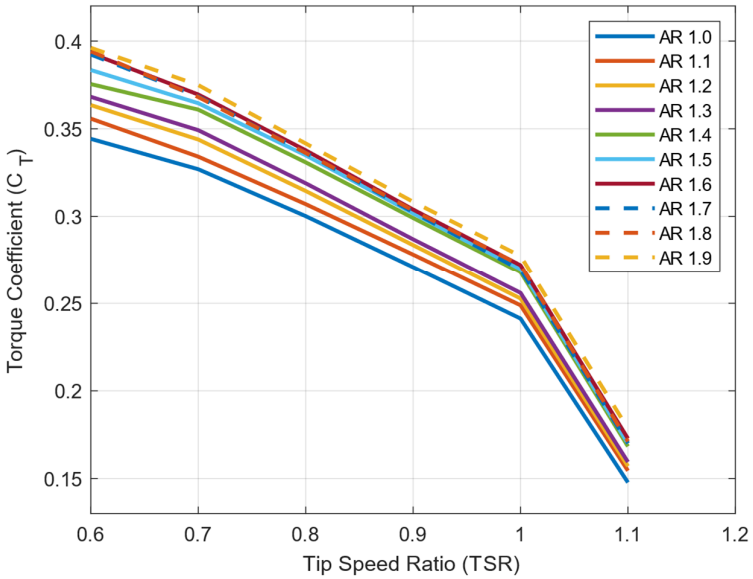


Figure 6.13. C_T vs. TSR curve of the AR configurations

As can be seen in Figure 6.13, the generated C_T increases with the rise in turbine AR at all TSRs. The peak C_T is generated at a TSR of 0.6 for all the studied ARs. As the TSR increases, the generated average C_T diminishes significantly for all turbines, with a notable reduction at TSR 1.1. This diminishing effect with increasing TSR on the torque generation capacity of the turbines can be attributed to changing relative velocity of the flow over the advancing and returning blades. This mechanism is discussed in detail in Section 6.2 . Figure 6.14 provides a visual representation of the increasing trend in C_T, specifically focusing on the maximum C_T generated at TSR 0.6 versus AR.

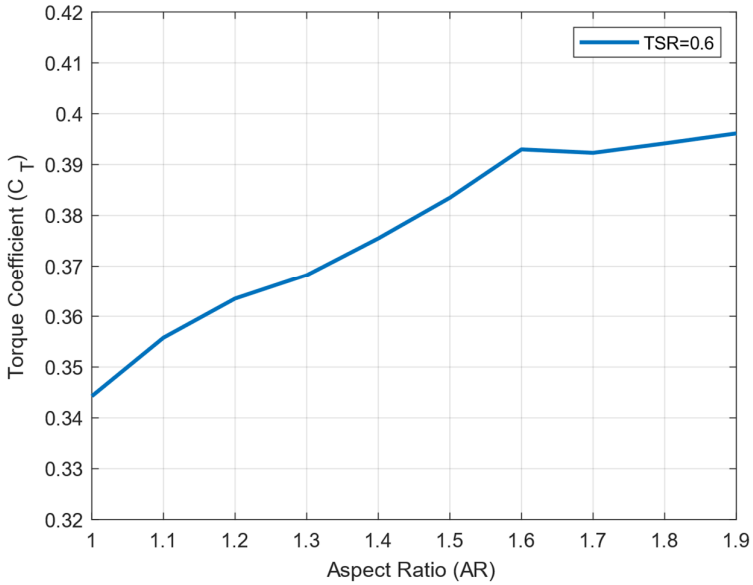


Figure 6.14. Highest C_Ts obtained by the AR configurations at 0.6 TSR

Although the peak C_T is attained as 0.396 at an AR of 1.9, the increasing trend observed in C_T generation decelerates and enters a plateau region beyond the AR of 1.6, as observed in Figure 2. This deceleration is also reflected in Figure 1, where the CT versus TSR curves for turbines with ARs beyond 1.6 converge into a narrow band. A slight reduction in C_T is noticeable for AR of 1.7. In fact, the AR of 1.6 generates C_T of 0.393 while the AR of 1.7 generates C_T of 0.392. Moreover, the AR of 1.6 exhibits 14.14% higher C_T than an AR of 1.0 while, an AR of 1.9 offers a marginal 0.17% improvement over an AR of 1.6. The variation of average C_P over studied TSRs for all ARs are presented in Figure 6.15.

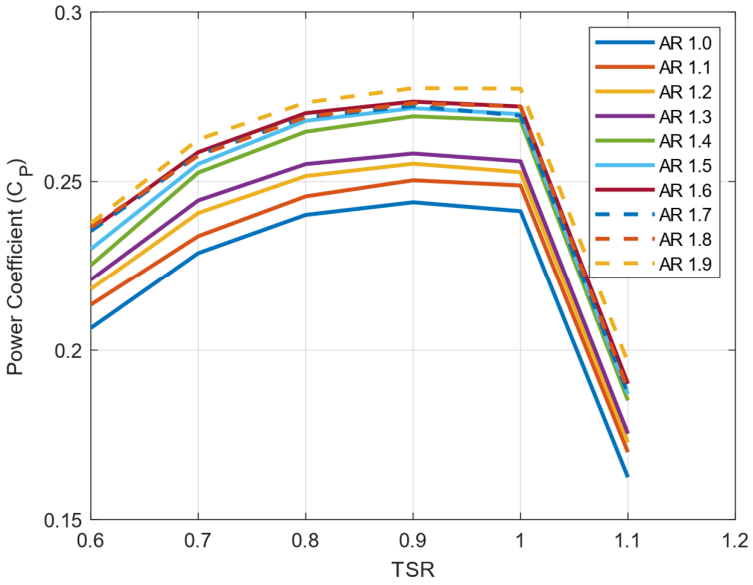


Figure 6.15. C_P vs TSR curve of the AR configurations

The exhibited C_p also demonstrates an increasing trend with the increase in AR for all TSRs up to an AR of 1.6. The peak C_{PS} are generated at a TSR of 0.9 for all the studied ARs as illustrated in Figure 6.15. The observed decrease in the torque generation with the increase in TSR does not directly translate to power generation since the C_P is also a function of TSR. However, the power generation capacity of the turbines is also reduced significantly at a TSR of 1.1. The explanation provided in Section 6.2.1 can also offer insights to this behavior. The maximum C_P generated at a TSR of 0.9 versus AR curve is presented in Figure 6.16 to provide a better visualization of the increasing trend in C_P.

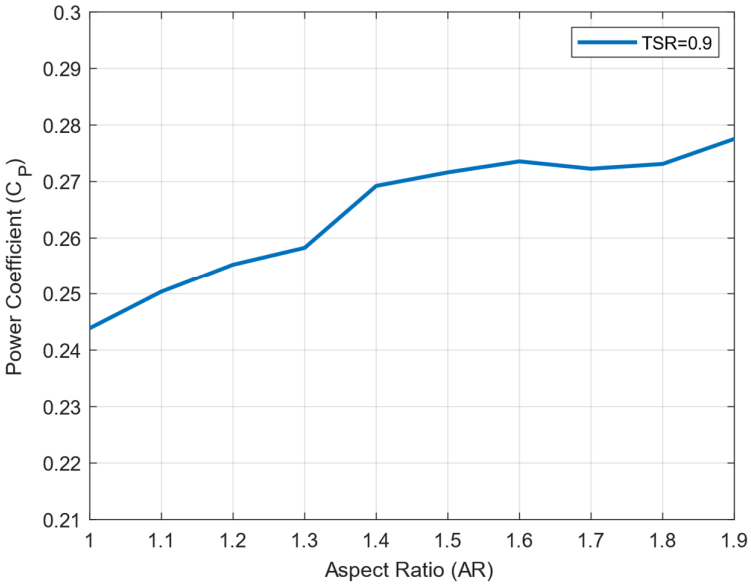


Figure 6.16. Highest C_Ps obtained by the AR configurations at 0.9 TSR

In a parallel pattern to the C_T variation at 0.6 TSR, the further increase in AR beyond 1.6 results in a slight downturn in Cp generation for AR 1.7 and AR 1.8. However, a marginal performance gain is also observed in AR1.9. The C_P generated by the AR1.9 is 1.09% larger than the C_P generated by AR1.6. AR1.6 exhibits C_P of 0.274 which is 0.72% and 0.36% higher than AR1.7 and AR1.8 respectively. When the presented C_T versus AR and C_P versus AR curves are analyzed as a whole, the performance gain from the increase in the AR of turbines has reached an optimum point at AR of 1.6. Beyond this threshold, only marginal changes are observed compared to the increase in AR. The torque generation curves of the turbines with studied ARs are presented for the single rotation of each turbine at TSR 0.9 in terms of generated torque (N.m) in Figure 6.17.

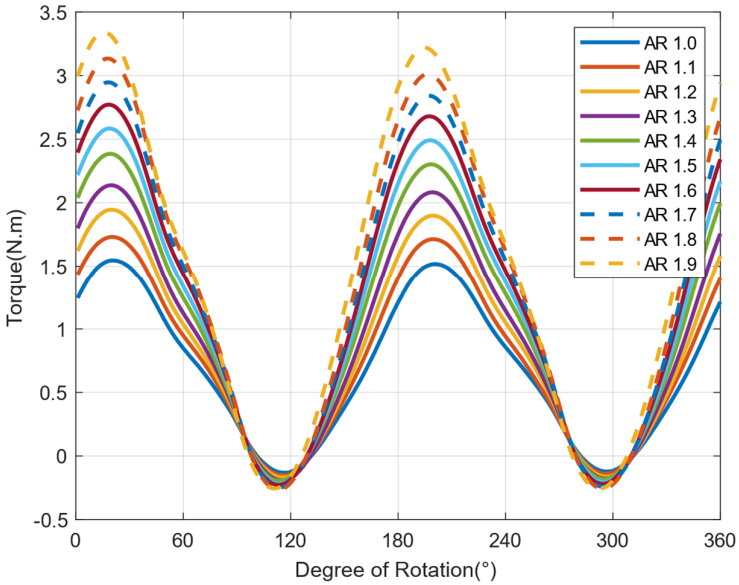


Figure 6.17. Torque generated by the AR configurations in a single rotation

As demonstrated in Figure 6.17, the increase in AR significantly amplifies the generated positive torque at around 20° and 200° of the rotation. However, a slight decrease in torque generation also occurs around angular positions of 110° and 270°. As seen in Figure 6.17, the turbine experiences an asymmetrical/uneven performance improvement through the rotation with increasing AR. Consequently, the torque fluctuations experienced by the turbine is increased with the increased AR. In fact, the standard deviations of the generated torques of AR1.0, AR1.6 and AR1.9 are 0.557, 0.997 and 1.196 respectively. As a result of the increase in torque fluctuations and AR, the produced mechanical vibrations, the subjected mechanical loads, and noise emissions are increased. The escalation in mechanical loads and vibrations poses a potential risk to the structural integrity of the turbine. Moreover, this increase in torque fluctuations may put additional stress on the voltage regulation systems that are coupled with the turbine. This increased load on the electrical components may also lead to a decrease in the overall efficiency of the system. By considering these possible adverse effects of the increased torque fluctuation, the optimum AR

of the studied turbine model can be deemed as 1.6 although the AR1.9 performance slightly better than the AR1.6.

6.4.2 Evolution of Flow Field around AR Configurations

The performance enhancement that arises from increasing AR is closely linked to effect of the endplates placed at the tip of the SHT on the flow field around the turbine. These endplates create a confined flow field between blade surfaces and themselves. This helps to increase the pressure difference between the convex and concave sides of the turbine which is an essential factor for the generation of drag force on the blade profiles. This confinement effect reaches a maximum point with the increasing AR of the turbine. The endplates additionally help to redirect the water flow towards the center of the blade, thereby enhancing the efficiency of water flow utilization. By achieving this flow redirection, the turbine's power generation capabilities can be further enhanced as it maximizes the water interaction with the blade surface.

In Figure 6.18, the pressure contours at the middle section of the turbines having AR of 1.2, 1.4, 1.6 and 1.8 are presented at a TSR of 0.6. This presentation aims to offer insights into the confinement effect resulting from the increasing AR on the pressure distribution around the turbine. The pressure contours are presented at both 30° and 60° of the rotation for the specified ARs. The pressure in front of the concave side of the advancing blade increases through AR1.0 to AR1.6 for both presented angular positions. However, this increase stops beyond AR1.6. When the pressure distributions in front of the concave side of AR1.6 and AR1.8 are compared, it can be seen that the pressure distributions are quite similar to each other especially at 60° of rotation. Additionally, the pressure drops on the convex side of the advancing blade intensify with increasing AR up to AR1.6 especially at 30° of the rotation. Beyond an AR of 1.6, the observed pressure drops remain almost constant as evident when comparing pressure contours for AR 1.6 and AR 1.8. Consequently, the pressure difference between the concave and convex side of the advancing blade

increases which results in amplified torque generation for the turbine. Moreover, when the pressure contours on the convex side of the returning blade are observed, a slight increase in high pressure, which adversely affects the performance of the turbine, is noticed. However, the observed pressure increase in front of the concave side of the advancing blade and the convex side of the returning blade shows distinct behaviors. The increased pressure on the convex side of the returning blade is focused on a very limited area and does not expand over the surface of the returning blade with increasing AR. In contrast, the high pressure occurs on the concave side of the advancing blade expands through the outer tip of the blade edge rather than focusing on a limited region. This distinction is evident when the pressure contours of AR1.0 and AR1.6 are compared at 30° of the rotation. Therefore, the overall performance of the turbine increases due to both larger increase in pressure on the concave side of the advancing blade and the augmented moment arm resulting from the expansion of high-pressure zone over the advancing blade profile.

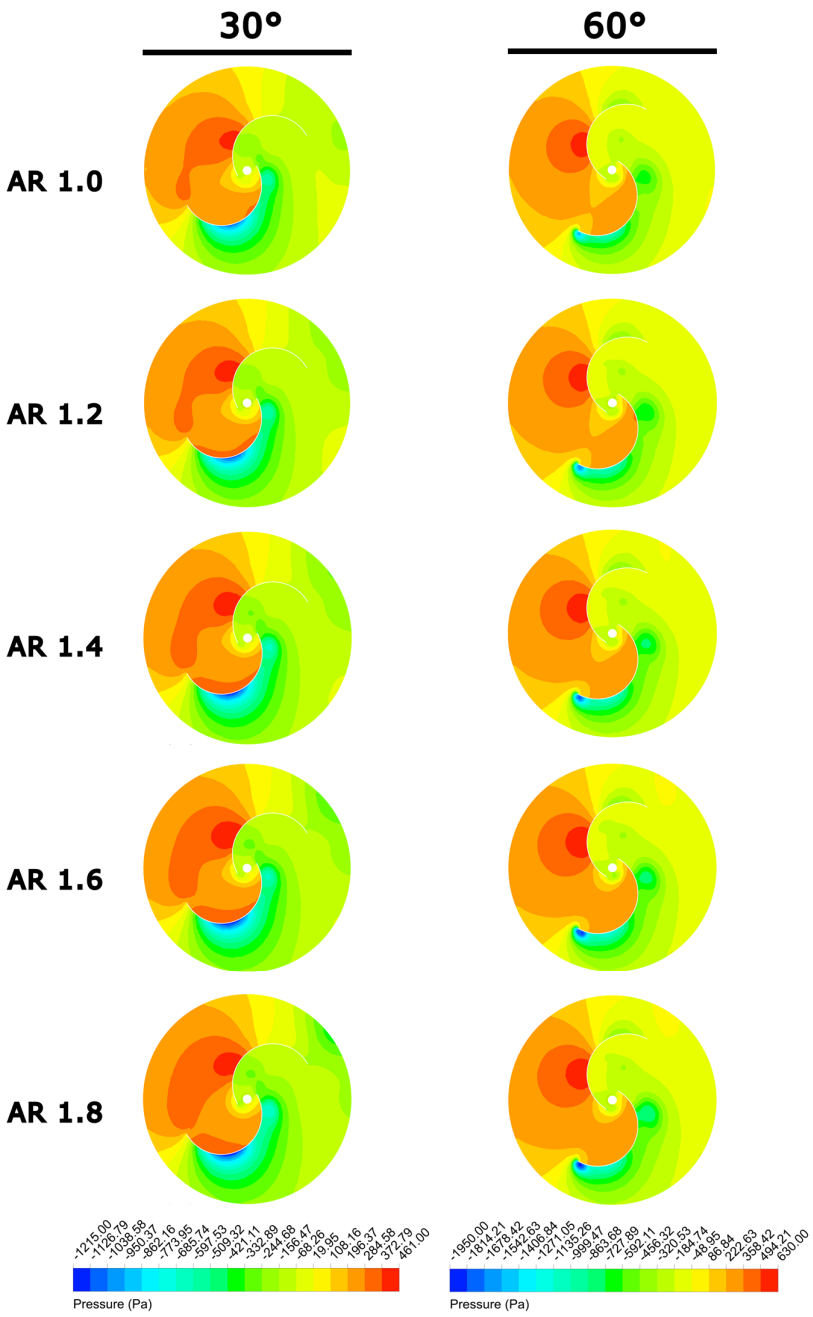


Figure 6.18. Pressure contours at the mid-sections of AR1.2, AR1.4, AR1.6 and AR1.8 at TSR 0.6

In Figure 6.19, the pressure contours along with the streamlines at the middle section of the advancing blade is presented for TSR 0.9. The cutting plane used to generate streamlines and pressure contours is also shown in the upper right corner of the Figure 6.19. The pressure in front of the advancing blade is slightly increased as the AR increases. Also, when the presented streamlines are examined, those positioned in the middle of the presented plane come at steeper angles to blade surface for all AR. However, in the region closer to the endplates, the streamlines start to deflect towards the endplates for all AR. Notably, as the AR increases, the size of the region where streamlines approach at steeper angles expands. This implies that higher AR values lead to more effective redirection of incoming water flow towards blade cores, resulting in a more even distribution of water flow across the length of the blade in SHT. Although the presence of endplates at the sides of the turbine blade redirects the flow towards center of the blades and prevents the flow from escaping at the side tips, a flow separation is also observed at the edge of endplates. This flow separation results in the formation of two vortices at the outer surfaces of the endplates for all ARs presented in Figure 6.19. A portion of the incoming water escapes from the edges of the endplates. This escaping water reduces the overall efficiency of the SHT as it does not contribute to power generation process. In Figure 6.19, the left edges of the endplates of presented turbines are aligned. Although the size of the low-pressure zone arising from the presence of end vortex expands slightly towards the flow direction with increasing AR, the vortex sizes are very similar. By considering the observations on the escaping flow and the better redirection of water with the increasing AR, the observations suggest that the proportion of the incoming water flow that exits through the endplate edges is reduced with the increasing AR.

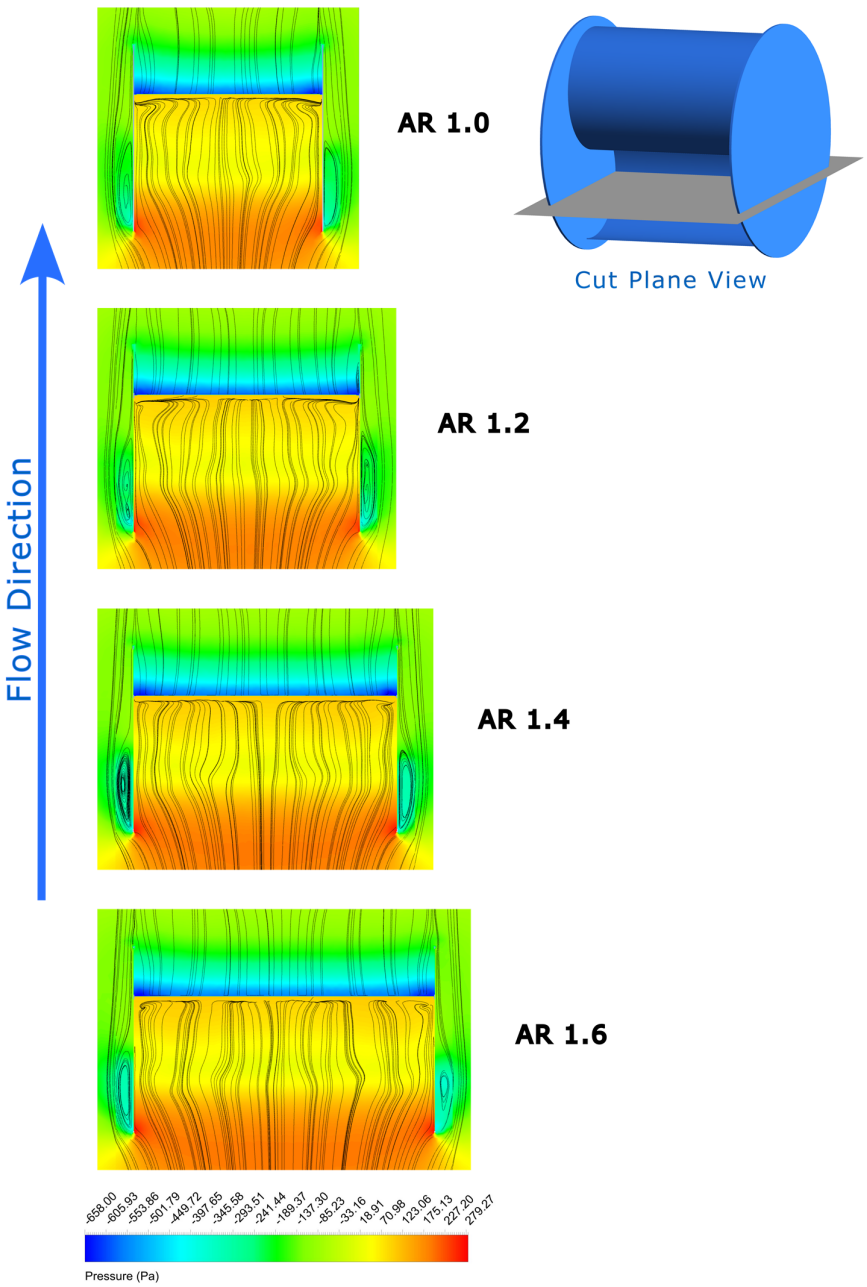
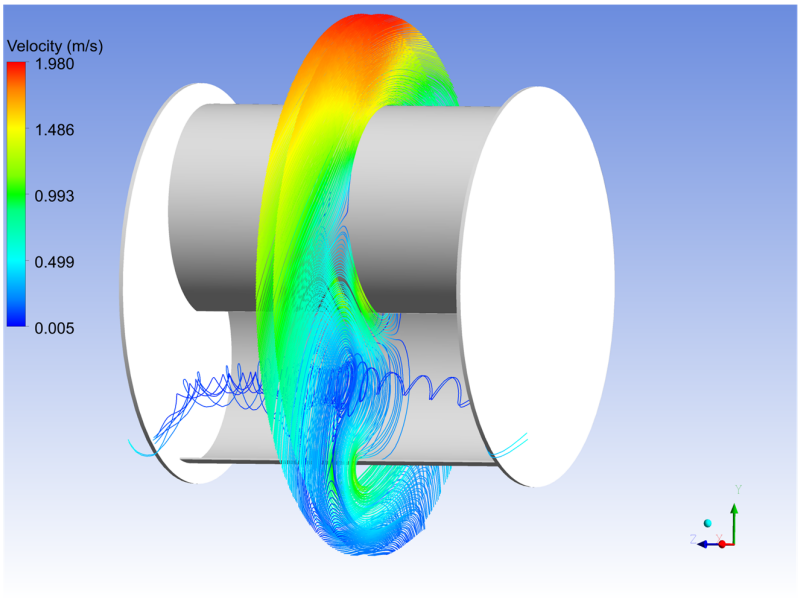
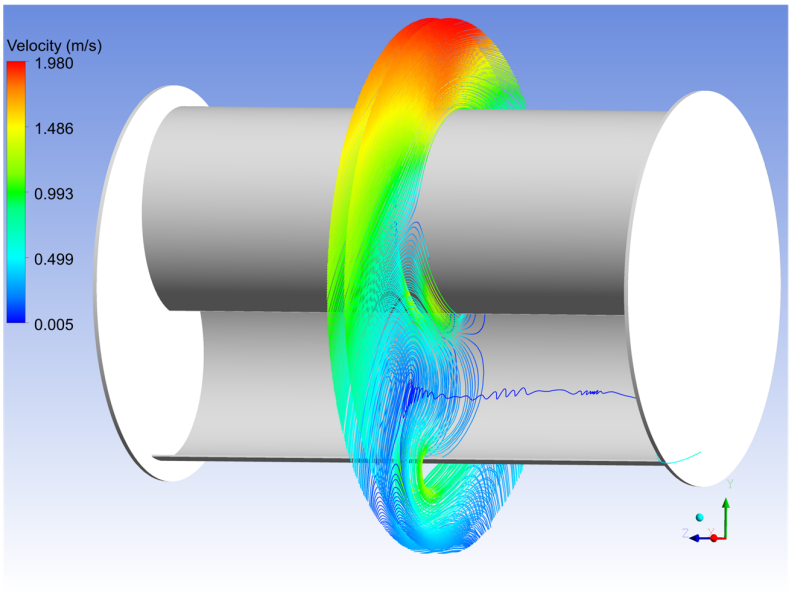


Figure 6.19. Pressure contours and streamlines presented on horizontal section of AR1.0, AR1.2, AR1.4 and AR1.6

To further investigate the observations discussed in Figure 6.19, 3D streamlines are generated in Rotational Domain at TSR 0.9. 3D streamlines generated for AR1.6 and AR1.0 are presented in Figure 6.20. For both AR1.0 and AR 1.6, two semicircular lines, 5 mm apart from the middle section, are defined over the interface of the rotational domain. These lines are utilized as seed points for the streamline generation.



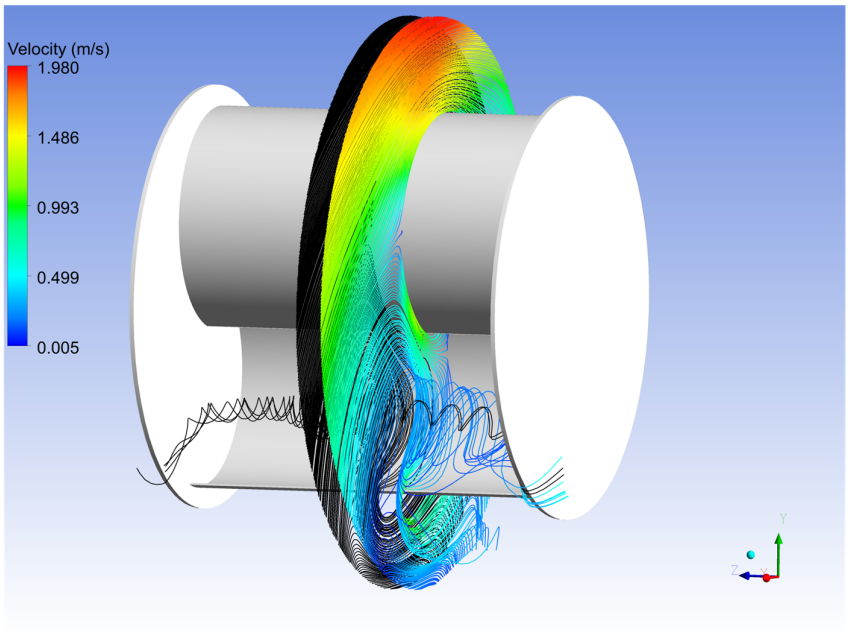
AR 1.0



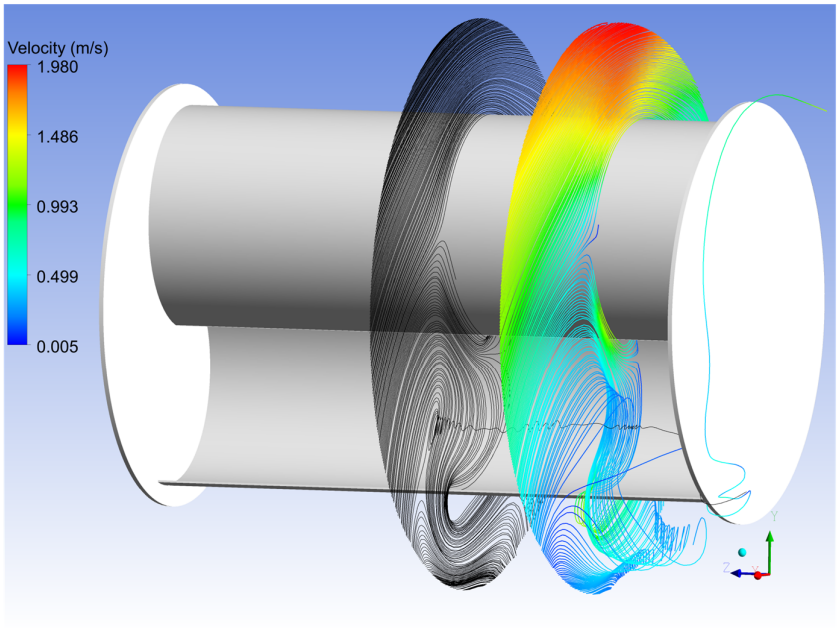
AR 1.6

Figure 6.20. 3D streamlines presented near mid-sections of AR1.0 and AR1.6

In Figure 6.20, out-of-plane vortex formations are observed just below the middle height of the advancing blade. Notably, for AR1.0, out-of-plane vortices form from both of the defined seed lines, while only one out-of-plane vortex is observed for AR1.6. In both cases, these vortices propagate towards the endplates, and some portion of the incoming water from the seed points escapes from the edges of the endplates. Moreover, the observed out-of-plane vortices on AR1.0 are considerably larger than the observed one on AR1.6. Therefore, the flow near the center of AR1.6's blades exhibits more planar motion, whereas the flow near the center of AR1.0's blades is not confined to a single plane. This indicates that the endplates better redirect the incoming flow to center of the blades with the increasing AR, resulting in higher pressure being exerted on the blade surface, as observed in Figure 6.18. To analyze the flow interactions near the endplates, another seed line is defined 10 cm apart from the endplates of AR1.0 and AR1.6. The generated 3D streamlines are presented in Figure 6.21.



AR 1.0



AR 1.6

Figure 6.21. 3D streamlines presented at 10 cm away from the endplates of AR1.0 and AR1.6

In Figure 6.21, the seed line defined 5 mm to the right of the middle sections of AR1.0 and AR1.6 was also used to generate streamlines and the resulting streamlines are presented in black. The seed lines 10 cm away from the endplates are 2.5 cm and 10 cm away from the middle sections of AR1.0 and AR1.6, respectively. As seen in Figure 6.21, although the seed points of AR1.6 are much farther away from the middle section, the disturbance on the planer motion of the fluid flow is less than of AR1.0. Moreover, the out of plane vortices propagated from the middle of the turbine occupy some portion of the volume in front of the advancing blade. This occupied volume manifests itself as a void where the streamlines at 10 cm cannot penetrate, as seen in Figure 6.21. The void in front of the advancing blade of AR1.0 is slightly larger than the one in front of AR1.6. When the propagating vortices shown as black and the void sizes are examined, it appears that more intensified vortices are formed in front of the advancing blade of AR1.0 in a much smaller distance of 2.5 cm. It may be inferred from this observation that disturbance on the planarity of the fluid flow is smaller on a larger fraction of the frontal area of AR1.6 compared to AR1.0. Consequently, the water flow interaction with turbine blade surfaces is enhanced for AR1.6, thereby increasing the incoming water flow utilization. Furthermore, the proportion of escaping water flow to incoming water flow from seed line is larger for AR1.0 as seen when the escaping streamlines compared.

6.5 Results Multi-stage

This section explores the findings of the investigation on the effect of multi-stage configurations on the performance of the studied SHT model. Two-stage and three-stage configurations are simulated with various phase differences to determine the corresponding optimum phase difference angle. In the case of the two-stage configuration, phase difference angles ranging from 15° to 90° with 15° increments are investigated. For three-stage configuration, phase difference angles ranging from 15° to 60° with 15° increments are investigated. The AR of the stages are kept

constant at 0.95 for all two-stage and three-stage configurations. Therefore, the two-stage and three-stage configurations have ARs of 1.90 and 2.85, respectively. It is noteworthy that for multi-stage configurations with a 0° phase difference, the middle plates are not included. Therefore, the three-stage configuration with 0° phase difference corresponds to the single-stage configuration with an AR of 2.85 and the two-stage configuration with 0° phase difference corresponds to single-stage configuration with an AR of 1.90.

Throughout the discussion, the test IDs provided in "Test case: Multi-stage" section will be used to refer the relevant multi-stage SHT configuration. Additionally, the benchmark model will be referred as "1S-SHT-PD0°-AR1.0".

6.5.1 Performance Analysis of Two-stage SHTs

The results of the two-stage configurations having varying phase differences from 15 to 90° and the single-stage counterpart (1S-SHT-PD0°-AR1.9) are compared for TSRs ranging from 0.6 to 1.1. Figure 6.22 illustrates the variation of average CT across all studied phase differences for the considered TSR range.

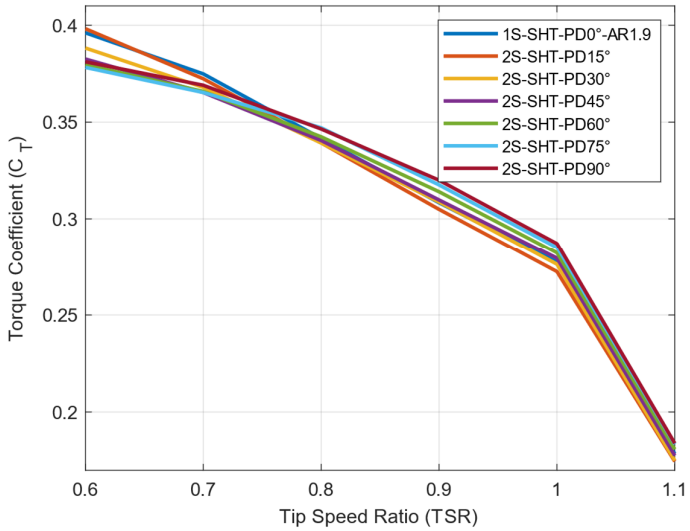


Figure 6.22. C_T vs. TSR curves of two-stage configurations

It can be clearly seen from Figure 6.22 that the peak C_Ts are generated at TSR of 0.6 for all the phase differences studied. As the TSR increases, the generated average C_T diminishes significantly for all two-stage turbines, with a notable reduction at TSR 1.1. The maximum C_T is achieved by 2S-SHT-PD15° as 0.398 at TSR of 0.6 which is 0.5% higher than 1S-SHT-PD0°-AR1.9. Beyond these observations, the presented C_T vs. TSR curves shows that the performance of the SHTs displays a non-uniform behavior with changing phase difference angles, indicating both enhancements and deteriorations at distinct TSR values for each phase difference. To better illustrate this exhibited non-uniform behavior, the generated average C_T values are presented over phase difference angles for studied TSRs in Figure 6.23.

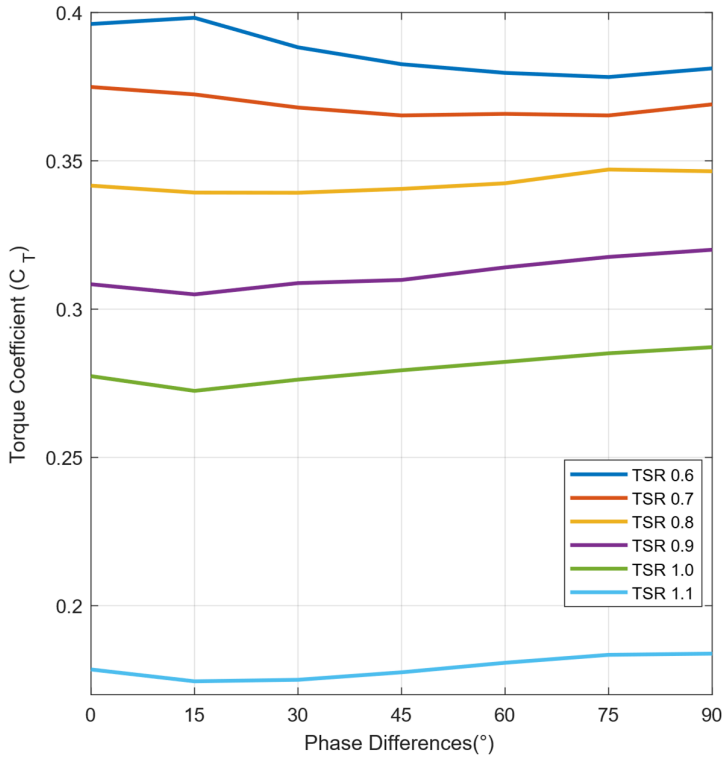


Figure 6.23. C_T vs. phase difference angle curves of two-stage configurations

As can be seen in Figure 6.23, the non-uniform impact of the angle of phase difference on the torque generation capacity of the SHT is obvious. Specifically, an increase in the phase difference angle leads to a degradation in torque generation capacity at TSRs of 0.6 and 0.7. However, this trend reverses beyond the TSR of 0.7 which results in an augmentation of the generated torque. In fact, at 0.6 TSR, 2S-SHT-PD90° exhibits 3.79% and 4.27% less C_T than 1S-SHT-PD0°-AR1.9 and 2S-SHT-PD15°, respectively. Conversely, at 0.9 TSR, 2S-SHT-PD90° generates 3.76% and 4.06% higher C_T than 1S-SHT-PD0°-AR1.9 and 2S-SHT-PD15°, respectively. The variation of average C_P over studied TSRs for all phase differences are presented in Figure 6.24.

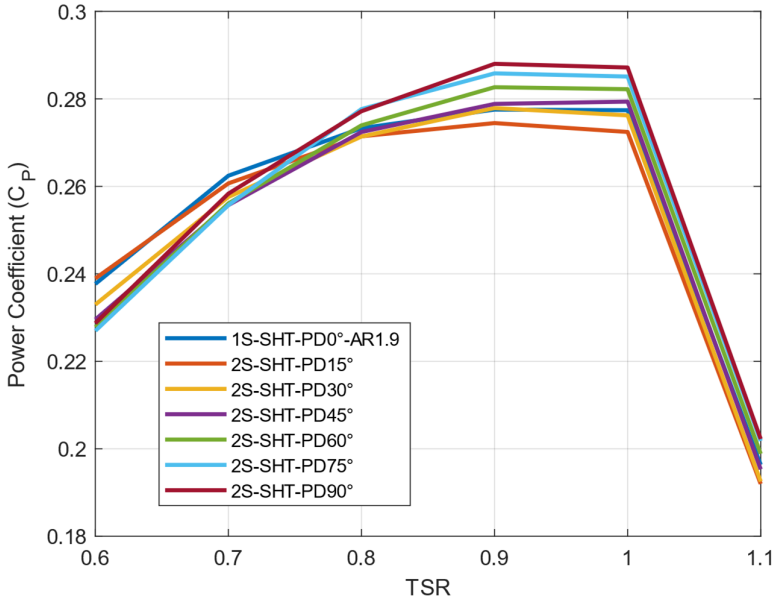


Figure 6.24. C_P vs. TSR curves of two-stage configurations

The observed non-uniform effect of increasing phase differences, as discussed in reference to Figure 6.22 and Figure 6.23, is further illustrated in Figure 6.24. As can be seen in Figure 6.24, the increased phase difference angles result in a decrease in C_P generation at TSRs of 0.6 and 0.7 However, beyond the TSR of 0.8, the increase in phase difference translates to augmented power generation capacity. The peak C_{PS} are generated at TSR of 0.9 except for 2S-SHT-PD45°. 2S-SHT-PD45° exhibits a 0.2% higher C_P at TSR 1.0 than at TSR 0.9. With the increase of phase difference, an increasing trend is observed for the generated peak C_{PS}. The power generation capacity of the turbines also reduced significantly at TSR of 1.1. The maximum C_P generated at TSR 0.9 versus phase difference angle curve is presented in Figure 6.25 to provide better visualization of the increasing trend in generated peak C_{PS}.

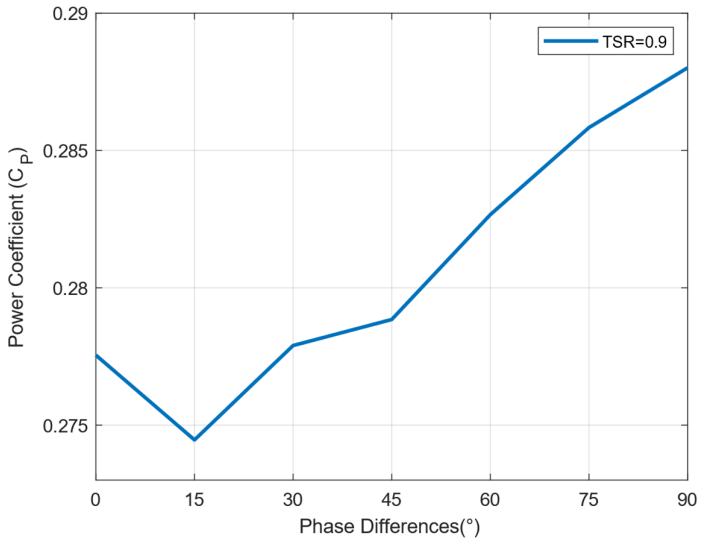


Figure 6.25. Highest C_Ps obtained by the two-stage configurations at 0.9 TSR

The increase in the phase difference angle correlates with an increased peak C_P, as shown in Figure 6.25, except for the phase difference angle of 15°. The highest C_P is achieved as 0.288 by 2S-SHT-PD90° which is 3.78% higher than 1S-SHT-PD0°-AR1.9. In Figure 6.26, the torque generation curves of the turbines with phase difference angles of 0°, 30°, 60°, and 90° are presented for the single rotation of each turbine at TSR 0.9 in terms of generated torque (N.m).

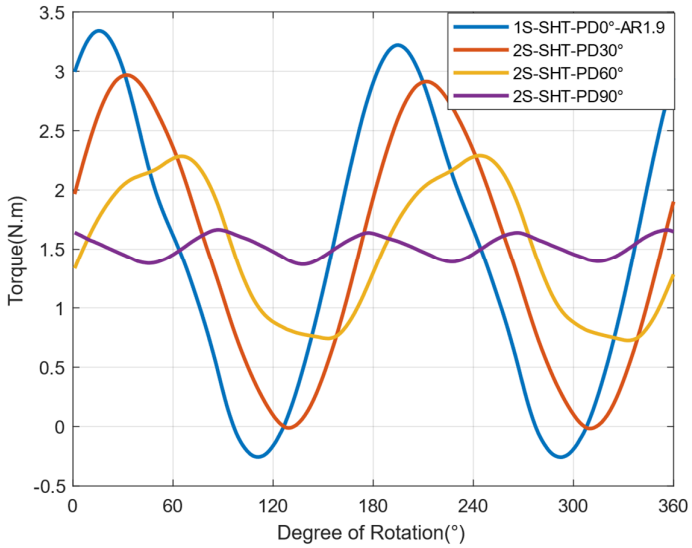


Figure 6.26. Torque generated by the two-stage configurations in a single rotation

The two-stage SHT exhibits a rotational symmetry of 90°. As shown in Figure 6.26, as the phase difference angle approaches the rotational symmetry (90°), the torque fluctuations experienced by the turbine significantly reduce. This reduction in torque fluctuations is further illustrated in Figure 6.27, where the standard deviations of the generated torques over a single rotation for each turbine are presented.

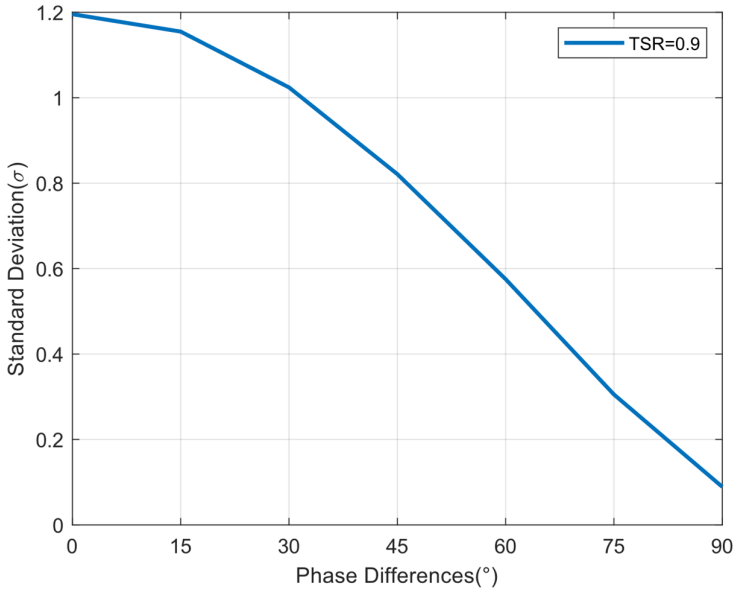


Figure 6.27. Standard deviation of torque generated by the two-stage configurations

The application of 90° phase difference leads to a remarkable 92.56% reduction in experienced torque fluctuation compared to 1S-SHT-PD0°-AR1.9. As a result of the reduction in torque fluctuations, both the produced mechanical vibrations, the subjected mechanical loads and noise emissions are decreased. Moreover, the bending moments that occur on the blade profiles are nearly halved with the inclusion of middle plates between the stages. Consequently, the structural integrity of the turbine is augmented. The reduced fluctuation in power output also alleviates the stress on the voltage regulation systems coupled with the turbine, contributing to overall operational stability and efficiency.

6.5.2 Performance Analysis of Three-stage SHTs

The results of the two-stage configurations with varying phase differences ranging from 15 to 60° are compared for TSRs ranging from 0.6 to 1.1. Figure 6.28 shows the variation of average C_T over studied TSRs for all studied phase differences.

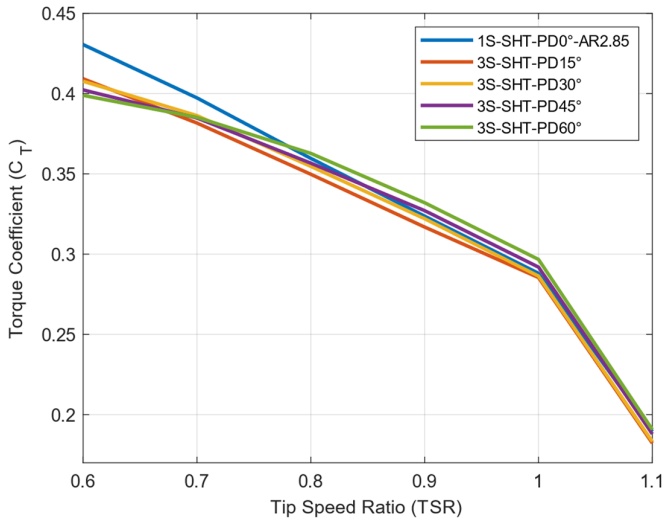


Figure 6.28. C_T vs. TSR curves of the three-stage configurations

Figure 6.28 shows that the peak C_Ts are consistently achieved at a TSR of 0.6 for all the tested phase differences. As the TSR increases, the generated average C_T decreases dramatically for all three-stage turbines, with a notable decline at TSR 1.1. 1S-SHT-PD0°-AR2.85 achieves the maximum C_T of 0.431 at a TSR of 0.6. This marks a significant 5.2% higher C_T over the top-performing three-stage turbine, which is 3S-SHT-PD15°. This contrasts with the observations in the two-stage configuration where the two-stage configuration with a 15° phase difference demonstrates superior performance in terms of generated C_T at TSR 0.6, as illustrated in Figure 6.22 and Figure 6.23. The observed contrast in performance can be attributed to the variance in application of phase differences to the stages. The phase difference represents the phase discrepancy between consecutive stages for three-stage configurations. Notably, in the case of 3S-SHT-PD30°, the actual phase difference between the first and third stages amounts to 30°. Consequently, the decrease in the projectile area facing the water flow is more pronounced for the three-stage turbine. Moreover, the impact of applied phase differences on the torque generation capacity is also non-uniform in three-stage turbines, similar to the

observed behavior in two-stage turbines in Figure 6.23. An increase in the phase difference angle leads to a degradation in torque generation capacity at TSRs of 0.6 and 0.7. Beyond a TSR of 0.7, the increased AR results in enhanced torque generation. For instance, 1S-SHT-PD0°-AR2.85 generated 7.9% more C_T at TSR 0.6 compared to 3S-SHT-PD60°. On the other hand, 3S-SHT-PD60° exhibits 3% more C_T at TSR 1.0 than 1S-SHT-PD0°-AR2.85. The variation of average C_P over studied TSRs for all phase differences regarding the three-stage configurations are presented in Figure 6.29.

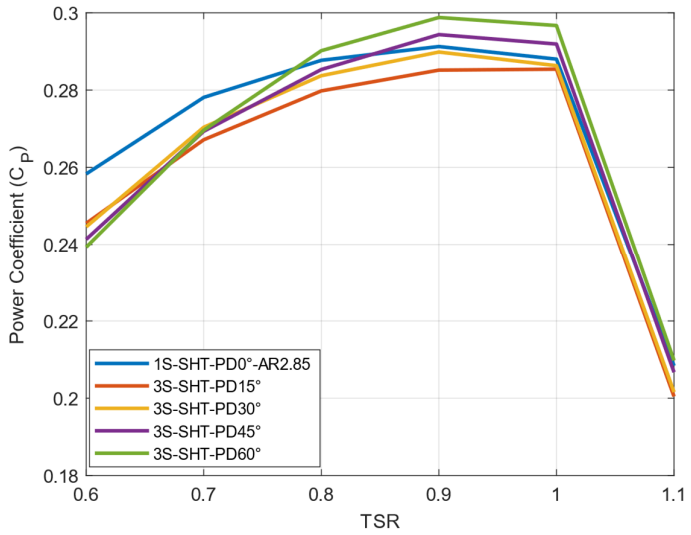


Figure 6.29. C_P vs. TSR curves of the three-stage configurations

Figure 6.29 demonstrates that the peak C_Ps are generated at a TSR of 0.9, with the exception of 3S-SHT-PD15°. At TSR 1.0, 3S-SHT-PD15° has a 0.1% greater C_P than at TSR 0.9. As can be seen in Figure 6.29, the increased phase difference angles result in a reduction in C_P generation at lower TSRs. However, beyond the TSR of 0.8, the performance of 3S-SHT-PD45° and 3S-SHT-PD60° surpasses the performance exhibited by 1S-SHT-PD0°-AR2.85. The maximum C_P generated at TSR 0.9 versus phase difference angle curve is presented in Figure 6.30 to provide better visualization of the trend in generated peak C_Ps.

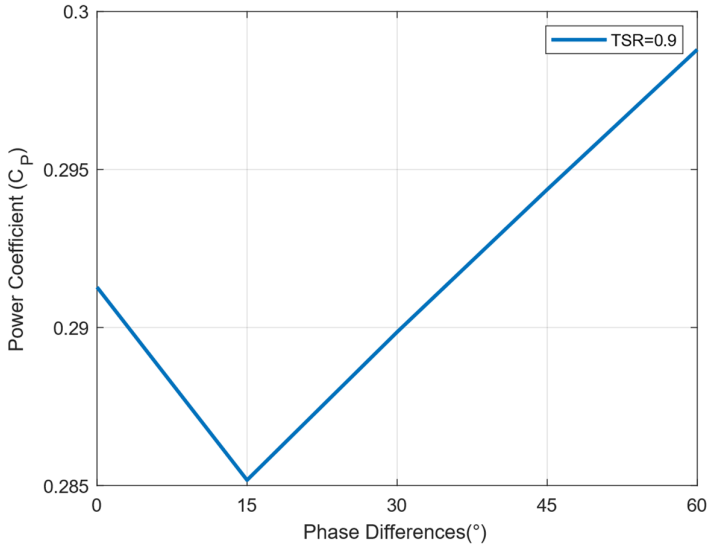


Figure 6.30. Highest C_Ps obtained by the three-stage configurations at 0.9 TSR

Figure 6.30 illustrates a significant performance reduction at the 15° phase difference angle. The 3S-SHT-PD15° exhibits a peak C_p of 0.285 which is 2.1% less than that of 1S-SHT-PD0°-AR2.85. Although a sharp increase in C_P is observed beyond the phase difference angle of 15, 3S-SHT-PD30° still generated a slightly lower C_P than the single stage counterpart. 3S-SHT-PD60° exhibits the highest C_P among the studied phase differences for three-stage configurations as shown in Figure 6.30. 3S-SHT-PD60° achieves a maximum C_P of 0.299 which is 2.75% higher than that of 1S-SHT-PD0°-AR2.85. Moreover, the performance gain at TSR 1.0 is slightly higher than the performance gain at 0.9. In fact, 3S-SHT-PD60° shows 3.02% greater performance at TSR 1.0 than 1S-SHT-PD0°-AR2.85 as can be observed in Figure 6.29. The torque generation curves of the three-stage turbines are presented for the single rotation of each turbine at TSR 0.9 in terms of generated torque (N.m) in Figure 6.31.

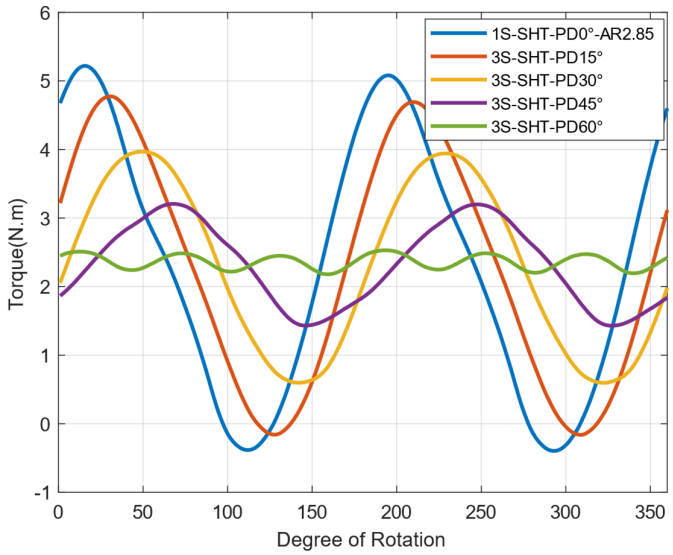


Figure 6.31. Torque generated by the three-stage configurations in a single rotation

As shown in Figure 6.31, the amplitude of the fluctuations observed on the generated torques reduces significantly with increasing phase difference angle, similar to the behavior observed in the two-stage configuration. Figure 6.32 further presents the standard deviation of the presented torque generation profiles in Figure 6.31.

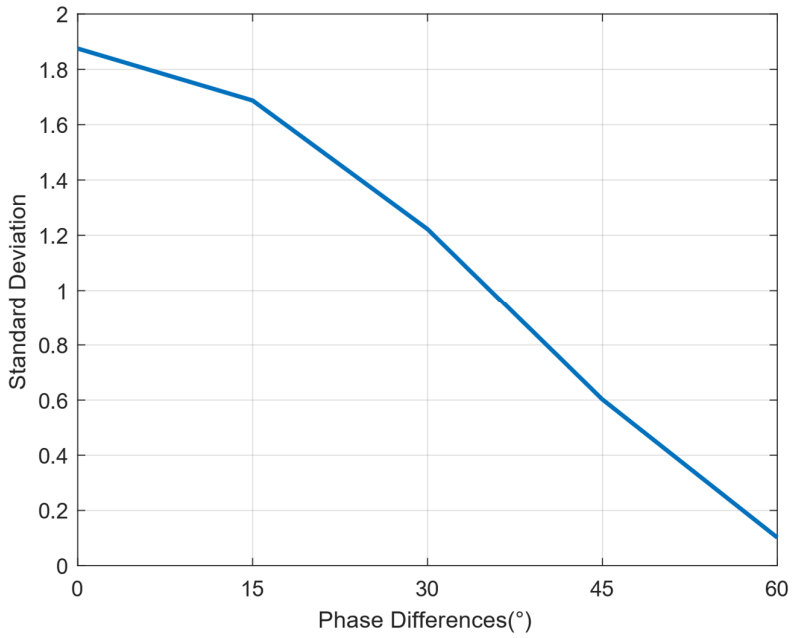


Figure 6.32. Standard deviation of torque generated by the three-stage configurations

Applying a 60° phase difference reduces torque fluctuation by 94.58%, as compared to 1S-SHT-PD0°-AR2.85. While 3S-SHT-PD60° achieves a higher percent of reduction in torque fluctuation compared to one in the two-stage configuration, an interesting contrast is observed. Although more stages contribute to the torque generation process in the three-stage configuration, 2S-SHT-PD90° has a 12% lower standard deviation of torque output compared to 3S-SHT-PD60°. Similar to the case of two-stage configuration, the reduction in torque variations reduces the produced mechanical vibrations, the subjected mechanical loads, and the noise emissions. The bending moment on the turbine blades is reduced by almost 65% with the insertion of intermediate plates between the phases. These benefits improve the structural integrity of the turbine.

6.5.3 Performance Comparison of Single-stage, Two-stage, Three-stage Turbines

This section aims to analyze the impact of adding stages to a SHT on its overall performance. To facilitate this comparison, the benchmark model with an AR of 1.0 (1S-SHT-PD0°-AR1.0) is selected as the single-stage configuration. This choice is based on the fact that the aspect ratio of the stages in the two-stage and three-stage configurations is 0.95, which is reasonably close to the benchmark model. Moreover, to facilitate the comparison, only the phase difference angles that yield the best performance are considered for the two-stage and three-stage configurations. Therefore, 2S-SHT-PD90° is selected for two-stage configuration while 3S-SHT-PD60° is chosen for the three-stage configuration. Figure 6.33 illustrates the variation of average C_T over studied TSRs for the single-stage, two-stage and three-stage turbines.

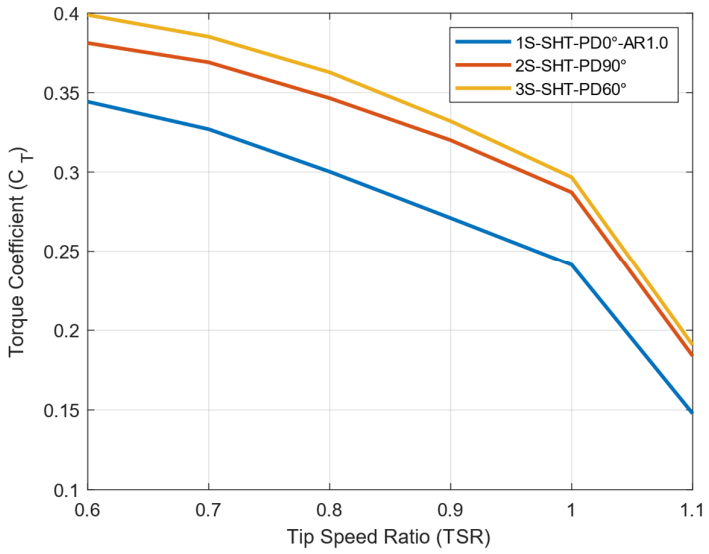


Figure 6.33. C_T vs. TSR curves of 1S-SHT-PD0°-AR1.0, 2S-SHT-PD90° and 3S-SHT-PD60°

Figure 6.33 demonstrates that the generated C_{TS}s are enhanced across all studied TSRs with an increase in number of stages from one to three. 2S-SHT-PD90° and 3S-SHT-PD60° exhibit 10.75% and 15.89% higher C_{TS}s, respectively, compared to 1S-SHT-PD0°-AR1.0 at TSR of 0.6. Also, 3S-SHT-PD60° achieves 4.64% greater C_T at TSR 0.6 compared to 2S-SHT-PD90°. The generated C_p over TSR curves of single-stage, two-stage, and three-stage turbines are presented in Figure 6.34.

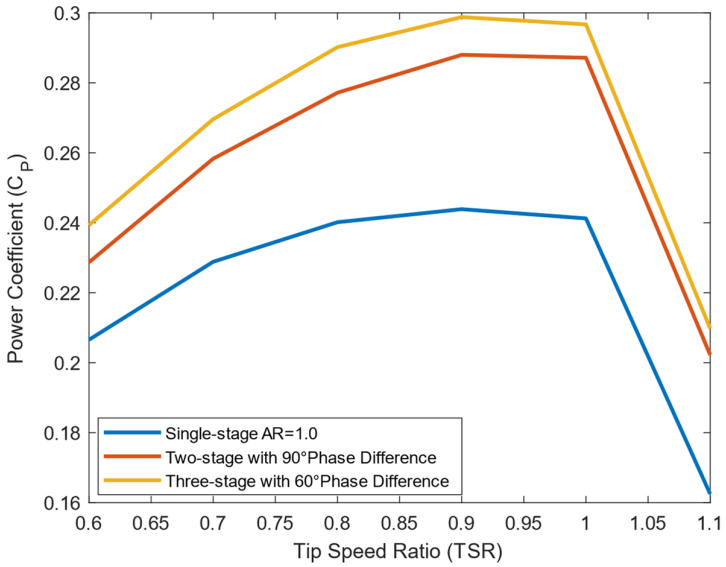


Figure 6.34. C_P vs. TSR curves of 1S-SHT-PD0°-AR1.0, 2S-SHT-PD90° and 3S-SHT-PD60°

With the increase in number of stages from one to three, the achieved C_Ps are increased for all TSR values. At a TSR of 0.9, 3S-SHT-PD60° and 2S-SHT-PD90° generated 22.50% and 18.08% greater C_P, respectively, compared to 1S-SHT-PD0°-AR1.0. Furthermore, 3S-SHT-PD60° achieves a higher C_P by 3.75% than 2S-SHT-PD90°. The observed trend in both Figure 6.33 and Figure 6.34 indicates a more significant increase in both generated C_T and C_P when increasing the stage number from one to two, compared to increasing the stage number from two to three. As discussed in Section 6.4, with the increase in AR, the fraction of the water escaping from tips of the turbine to incoming water flow is reduced. This effect reaches its

peak when the AR becomes 1.6 and beyond an AR of 1.6 only marginal performance changes observed. Since the AR of 2S-SHT-PD90° well beyond the AR of 1.6, the observed remarkable increase can be attributed to this effect discussed in Section 6.4. Furthermore, considering that 3S-SHT-PD60° turbine also has an AR that is beyond 1.6, any additional performance improvement from further increasing the AR is no longer viable. Therefore, 3S-SHT-PD60° offers milder improvements over 2S-SHT-PD90°. In Figure 6.35, the generated C_T over a single rotation of 1S-SHT-PD0°-AR1.0, 2S-SHT-PD90° and 3S-SHT-PD60° are presented.

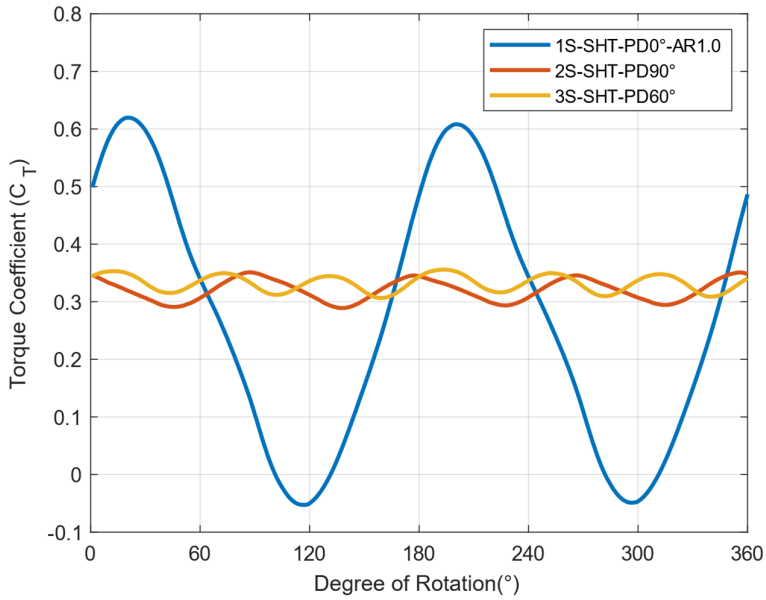


Figure 6.35. Torque generated by 1S-SHT-PD0°-AR1.0, 2S-SHT-PD90° and 3S-SHT-PD60° in a single rotation

As illustrated in Figure 6.35, the presented C_T curves of 2S-SHT-PD90° and 3S-SHT-PD60° exhibit significantly less oscillation compared to 1S-SHT-PD0°-AR1.0. However, the given curves in Figure 14 are presented in terms of C_T; therefore they do not directly convey the torque fluctuations experienced by the turbine due to different ARs of the turbines. When the standard deviation of the output torque in terms of (N.m) considered, 2S-SHT-PD90°and 3S-SHT-PD60° exhibit 84% and

82% less fluctuations compared to 1S-SHT-PD0°-AR1.0. This underlines the benefit of utilizing multi-stage configurations to stabilize the power output of the SHTs by considering that the turbine area is multiplied by two and three for two-stage and three-stage turbines. Although the single-stage turbine exhibits larger C_T values at certain degrees of the rotation, the overall performances of the two-stage turbine and the three-stage turbine are better than that of the single stage one as can be seen in Figure 6.33 and Figure 6.34.

6.5.4 Evolution of the flow field around multistage turbines

A multi-stage turbine's stages operate as parallel turbines, producing distinct torque values. Each stage contributes to the performance of the multi-stage configuration depending on its rotational position. Figure 15 presents the generated instantaneous C_T versus rotational angles curves of 3S-SHT-PD60° and its stages. The stages of 3S-SHT-PD60° are represented as “First Stage”, “Second Stage”, and “Third Stage” in Figure 6.36.

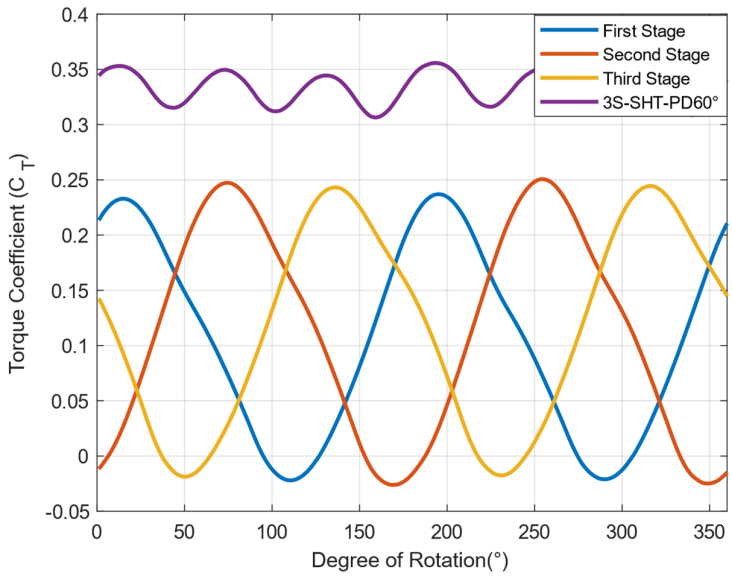


Figure 6.36. Torque generated by 3S-SHT-PD60° and its stages in a single rotation

It can be noted that when the generated torque by a stage reaches its maximum position, the other two stages exhibit a torque value closer to their minimum as seen in Figure 6.36. Consequently, the observed torque variations for three-stage turbine is significantly reduced. To illustrate, at 20° of the rotation, the first stage exhibits a torque value around its maximum; on the other hand, the second and third stages exhibit torque values closer to their minimum. Similarly, at 110° of rotation, the first stage exhibits a torque value around its minimum while, the second and third stages generate torque values closer to their maximum.

In Figure 6.37, the pressure contours at the middle section of each stage are presented at 20° and 110° of the rotation for 3S-SHT-PD60°. Additionally, the pressure contours at the centers 1S-SHT-PD0°-AR1.0 and 1S-SHT-PD0°-AR2.85 are shown in Figure 6.37.

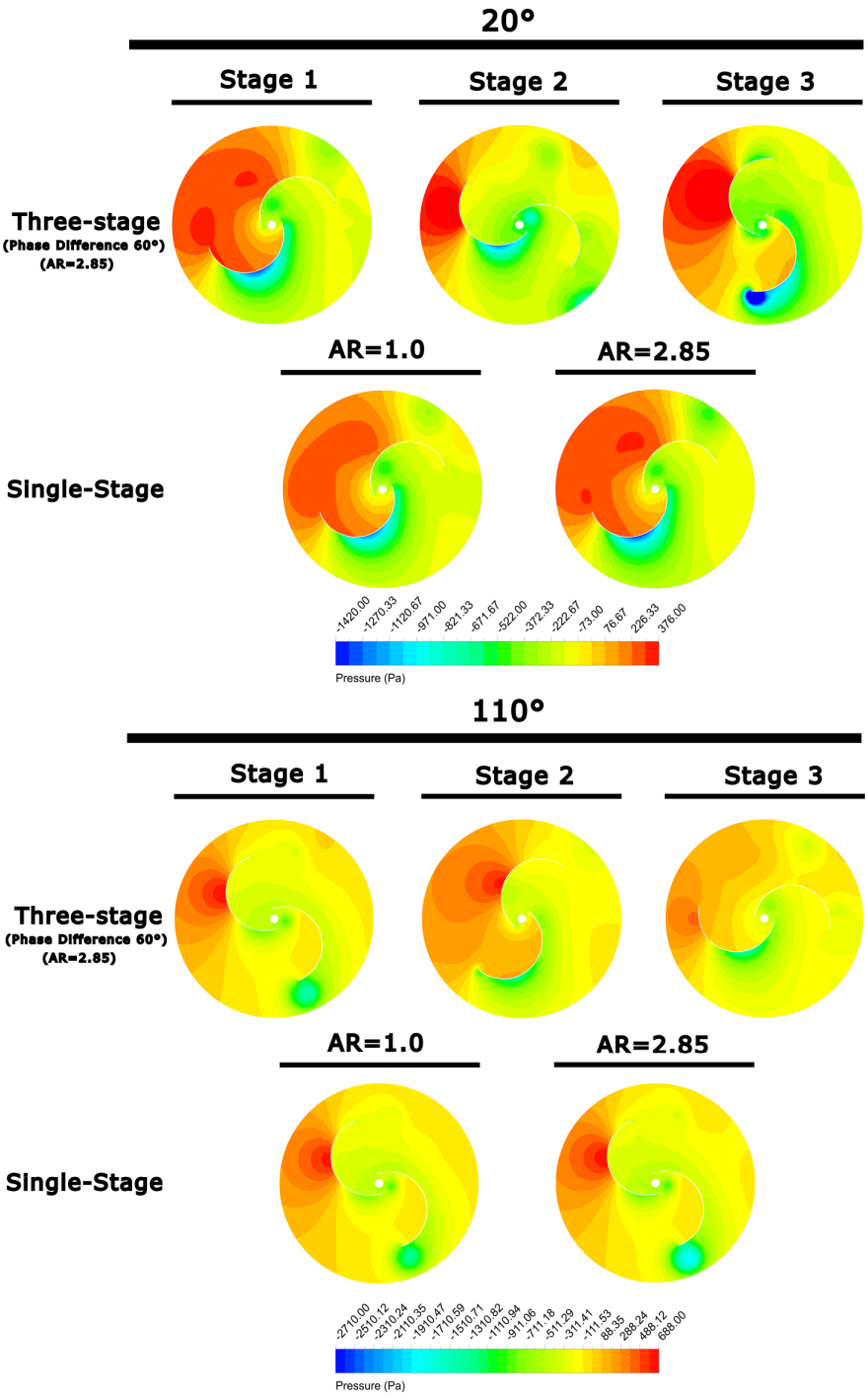


Figure 6.37. Pressure contours at mid-sections of 1S-SHT-PD0°-AR1.0, 1S-SHT-PD0°-AR2.85 and stages of 3S-SHT-PD60° at 20° and 110° of rotation

At 20° of rotation, the single-stage turbines and the first stage of 3S-SHT-PD60° are around their rotational position where turbines exhibit maximum torque as observed in Figure 6.36 for the first stage, Figure 6.35 for 1S-SHT-PD0°-AR1.0, Figure 6.31 for 1S-SHT-PD0°-AR2.85. At 20°, the advancing blade lies in front of the returning one; therefore the incoming flow first hits the concave side of the advancing blade. Consequently, the pressure over the concave side of the advancing blade significantly increases compared to the convex side of the returning blade. Moreover, a pressure drop occurs on the convex side of the advancing blade. The increased pressure differences between the concave and the convex side of the advancing blade and between the convex side of the returning blade and concave side of the advancing blade enhance the performance of the turbine. As illustrated in Figure 6.37, the pressure over the concave side of the advancing blade is significantly higher for the first stage of 3S-SHT-PD60° and 1S-SHT-PD0°-AR2.85 compared to 1S-SHT-PD0°-AR1.0. Interestingly, the first stage of 3S-SHT-PD60° is subjected to a higher pressure on the concave side of the advancing blade compared to 1S-SHT-PD0°-AR2.85. Also, a larger pressure drop is observed on the convex side of the advancing blades of the first stage and 1S-SHT-PD0°-AR2.85 compared to 1S-SHT-PD0°-AR1.0. On the other hand, the pressure on the convex side of the returning blade is significantly lower for 1S-SHT-PD0°-AR1.0 compared to the first stage of 3S-SHT-PD60° and 1S-SHT-PD0°-AR2.85.

At the second stage and the third stage of 3S-SHT-PD60°, the returning blade is positioned in front of the advancing blade, especially for the second stage. Therefore, the incoming water flow with high energy first impacts the returning blade. Consequently, a higher pressure occurs on the convex side of the returning blade. Also the concave side of the advancing blade is shielded by the returning blade, especially for the second stage. Due to these effects, the second stage and the third stage produce significantly less C_T than the first stage as can be seen in Figure 6.36. As a result, at 20° of the rotation, 1S-SHT-PD0°-AR2.85 generates significantly higher torque compared to the three-stage turbine as can be observed on Figure 6.31.

At 110° of the rotation, the single-stage turbines and the first stage of 3S-SHT-PD60° are around their rotational position where the turbines exhibit minimum torque as can be observed in Figure 6.36 for the first stage, Figure 6.35 for 1S-SHT-PD0°-AR1.0, Figure 6.31 for 1S-SHT-PD0°-AR2.85. At this angle, the incoming water flow firstly impacts the convex side of the returning blade, and the high pressure occurs on the returning blade. The advancing blade is also shielded by the returning blade. Due to these effects, the torque generation capacities of the single-stage turbines and the first stage of 3S-SHT-PD60° are deteriorated. When the pressure distribution around the blades of the single-stage turbines and the first stage of the 3S-SHT-PD60° are compared, it is evident that the distributions are very similar. This observation can be clarified through the understanding that at 110° of the rotation, the SHT generates torque values around zero, independent from of its AR. This can be observed by comparing the torque generation or C_T generation versus rotational degrees curves provided for the single stage turbines and the first stage of 3S-SHT-PD60°. At this angle, all single-stage SHTs and the first stage of 3S-SHT-PD60° generates similar values.

At 110° of the rotation, the second stage and third stage of 3S-SHT-PD60° are positioned at rotational angles of 50° and 350°, respectively. Therefore, they generate significantly higher torque compared to the first stage. Because of their substantial contribution to overall performance of 3S-SHT-PD60°, 3S-SHT-PD60° generates significantly higher torque compared to 1S-SHT-PD0°-AR2.85 at 110° of the rotation, as can be observed in Figure 6.31.

Figure 6.38 displays the pressure contours at the center of each stage in 2S-SHT-PD90° at rotation angles of 20° and 110°. Also, the pressure contours at the centers of 1S-SHT-PD0°-AR1.0 and 1S-SHT-PD0°-AR1.9 are shown in Figure 6.38. The pressure over the concave side of the advancing blades of the first stage of 2S-SHT-PD90° and 1S-SHT-PD0°-AR1.9 is substantially higher than 1S-SHT-PD0°-AR1.0. Also, the convex side of the advancing blade of 1S-SHT-PD0°-AR1.9 is subjected slightly higher pressure than the advancing blade of the first stage of 2S-SHT-PD90°. The pressure drops over the convex side of the advancing blades of 2S-SHT-PD90°'s

first stage and 1S-SHT-PD0°-AR1.9 are similar to each other and higher than 1S-SHT-PD0°-AR1.0. Moreover, the pressure over the convex side of 1S-SHT-PD0°-AR1.0's returning blade is considerably lower than the first stage of 2S-SHT-PD90° and 1S-SHT-PD0°-AR1.9.

At 20° of the rotation, the second stage of 2S-SHT-PD90° is at 110° of its rotation due to 90° phase difference. Consequently, the second half of 2S-SHT-PD90° exhibits significantly lower torque and limits the overall torque generation capacity of the two-stage turbine. As a result, 1S-SHT-PD0°-AR1.9 generates significantly higher torque at 20° compared to 2S-SHT-PD90°, as can be observed in Figure 6.26.

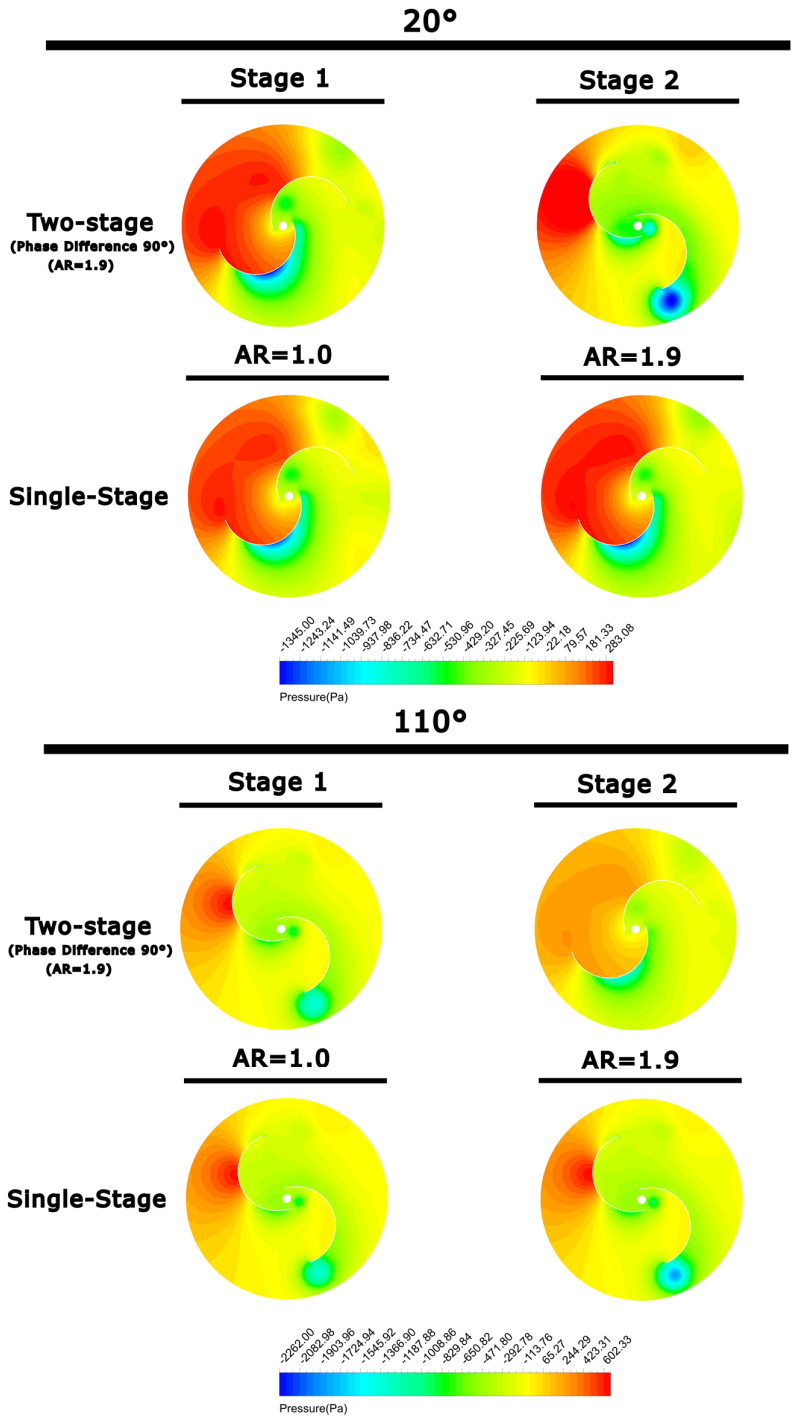


Figure 6.38. Pressure contours at mid-sections of 1S-SHT-PD0°-AR1.0, 1S-SHT-PD0°-AR1.9 and stages of 2S-SHT-PD90° at 20° and 110° of rotation

As explained in the discussion regarding the 110° of 3S-SHT-PD60°'s rotation, at 110°, the single-stage turbines and the first stage of 2S-SHT-PD90° are around their rotational position where turbines exhibit minimum torque values. The higher pressure occurs on the convex side of the returning blade for the single-stage turbines and 2S-SHT-PD90°'s first stage. The pressure field around the blades of the single-stage turbines and 2S-SHT-PD90°'s first stage is similar to each other. However, the pressure over the concave side of the advancing blades of single-stage turbines slightly higher than the first stage of the 2S-SHT-PD90°, in contrast to observation made on 3S-SHT-PD60°. Since the phase difference is 90° for the 2S-SHT-PD90°, at 110°, the second stage of 2S-SHT-PD90° is subjected to almost same pressure field as the first stage of 2S-SHT-PD90° turbine at 20° of the rotation. As a result, 2S-SHT-PD90° generates very similar torque values at 20° and 110° of the rotation, as can be seen in Figure 6.26. Moreover, both of the single-stage turbines experience substantial reduction in torque generation at 110°. Therefore, at 110°, 2S-SHT-PD90° exhibit remarkably higher torque values compared to 1S-SHT-PD0°-AR1.9.

It is observed that the given pressure contours at the first stages of 2S-SHT-PD90° and 3S-SHT-PD60° are very similar to the pressure contours of their single-stage counterparts (1S-SHT-PD0°-AR1.9, 1S-SHT-PD0°-AR2.85, respectively) in Figure 6.37 and Figure 6.38. This observation may suggest that the multi-stage configurations also benefit from the performance gain resulting from an increased AR of the turbine, even with the inclusion of middle plates between the stages. Inclusion of the middle plates does not seem to interfere with the performance gain resulted from augmentation of the AR of the turbine. To illustrate this phenomenon further, the horizontal pressure distribution in front of the advancing blades of 2S-SHT-PD90° and 3S-SHT-PD60° is presented in Figure 6.39. The pressure contour of 2S-SHT-PD90° is presented at 20° of rotation and the pressure contour regarding 3S-SHT-PD60° is presented at 50° of rotation. The cutting planes used to generate these pressure contours are illustrated at the right of the corresponding figures.

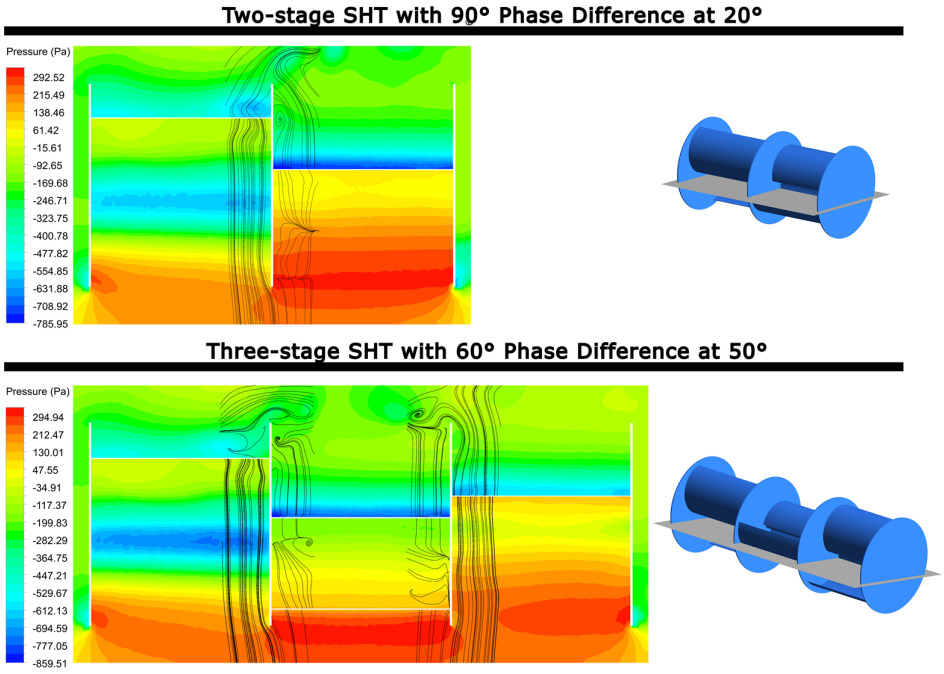


Figure 6.39. Pressure contours and streamlines in front of the advancing blades of 2S-SHT-PD90° and 3S-SHT-PD60°

Figure 6.39 reveals that, at 20°, the pressure in front of the first stage of 2S-SHT-PD90° is significantly higher than the second one that is at 110°. This can be attributed to the presence of the middle plate with right endplate since, they create a semi-confined flow field around the first stage and prevents water flow from escaping the tips of the first stage's blades to the second stage. Moreover, the middle plate between the stages causes a flow separation at the edge of it. Unlike the endplates, which allow some of the incoming flow to escape, the middle plate redirects water flow towards the second stage as evidenced by the streamlines provided for 2S-SHT-PD90° in Figure 6.39. As a result, this deflected portion of the incoming water still contributes to power generation process. Furthermore, the low-pressure zone that lies at the left of the middle plate has significantly higher pressure than the low-pressure zone at the outer side of the endplates as shown in provided pressure contours for 2S-SHT-PD90° in Figure 6.39. This observation suggests that

less portion of the incoming water is escaped from the first stage of 2S-SHT-PD90° to the second stage compared to the escaping water from the endplates. Moreover, despite the AR of stages being half of the AR of 1S-SHT-PD0°-AR1.9, Figure 6.38 also shows similar pressure distributions around the blades in the first stage of 2S-SHT-PD90° and 1S-SHT-PD0°-AR1.9. This observation made on Figure 6.38, coupled with the aforementioned pressure and flow patterns, suggests that the performance gain achieved through increased AR are preserved even in multi-stage configurations.

Figure 6.39 further reveals the pressure distribution and flow dynamics within 3S-SHT-PD60° at 50° of the rotation. It is observed that the pressure in front of 3S-SHT-PD60°'s middle stage is significantly higher than that of the other two stages. This is primarily due to the incoming flow that impacts the convex side of returning blade of 3S-SHT-PD60°'s middle stage, leading to a drastic increase in pressure in front of the convex side of the returning blade. Consequently, a portion of incoming water is re-directed to lower pressure zones in front of the advancing blades of the first and third stages of 3S-SHT-PD60°, as depicted by the streamlines provided for 3S-SHT-PD60°. The analysis of pressure distributions and flow patterns within 2S-SHT-PD90° and 3S-SHT-PD60° reveals the complex interplay between pressure gradients, blade geometry, endplates, and middle plates. These observations indicate that the middle plates placed in between the stages help prevent the flow from escaping the stages and re-direct the incoming flow to other stages. Therefore, the middle plates ultimately contribute to the maintenance of performance gains achieved through increased AR even in multi-stage configurations.

6.6 Results: Helical Blades

In this section, the results of the investigation on the impact of blade twist angle on the performance of a Helical SHT (HSHT). The model generation procedure is described in Section 5.3. Blade twist angles ranging from 0° to 90° are considered to generate helical blade profiles. It is noteworthy that the blade twist angle of 0°

presents the benchmark model in the provided results. The test IDs that are provided in Section 5.3will be used to refer relevant helical configurations.

6.6.1 Performance Analysis of Helical Blade Profiles

The obtained performance data of the helical configurations having blade twist angles ranging from 0° to 90° are compared with each other for TSRs ranging from 0.6 to 1.1. The average CT variation for the TSR range under consideration is shown in Figure 6.40 for all blade twist angles that have been analyzed.

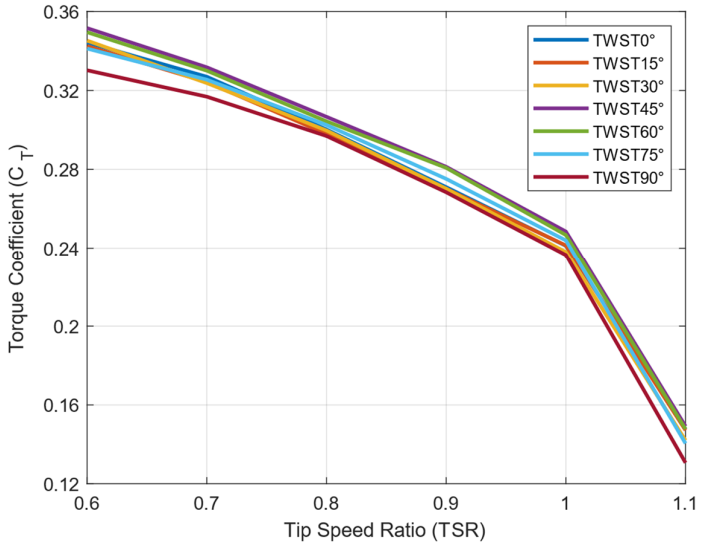


Figure 6.40. C_T vs. TSR curves of HSHT configurations

Figure 6.40 clearly shows that the highest C_{TS}s are produced at a TSR of 0.6 for all blade twist angles examined. With an increase in TSR, the average C_{TS} generated by all helical configurations decreases dramatically, particularly at TSR 1.1. The highest C_T is obtained with a blade twist angle of 45°, resulting in a value of 0.352 at a TSR of 0.6. This value is 2.12% greater than the C_T attained with a blade twist angle of 0°. Moreover, TWST45° achieved the highest C_{TS} at all TSR values. To better visualize the change of exhibited C_{TS} by the different blade angles, in Figure 6.41,

the produced average C_T values for the TSRs under study are displayed over phase difference angles.

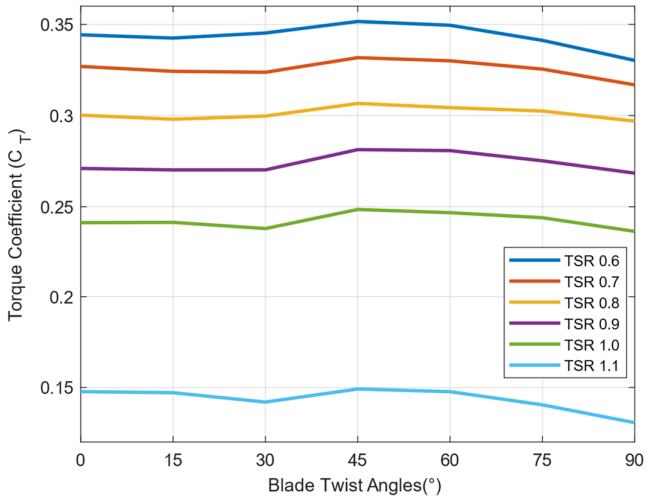


Figure 6.41. C_T vs. blade twist angle curves of HSHT configurations

The presented C_T versus twist angle curves in Figure 6.41 exhibit similar trends across the presented TSRs. TWIST15° and TWST30° achieve nearly identical C_T values as TWST0° for all considered TSRs. It is noteworthy that TWST0° attains a slightly higher C_Ts than TWST15° and TWST30° at all TSRs, except for TSR 0.6, where TWST30° generates higher C_T than TWST0°. While TWST45° and TWST60° generates comparable C_Ts, the torque generation capacity of the studied configurations consistently peaks at blade twist angle of 45° across all TSRs. It is worth emphasizing that the maximum improvement offered by TWST45° over TWST60° is a modest 1% at TSR 1.1. Beyond a blade twist angle of 60°, the torque generation capacity gradually decreases with the lowest C_Ts consistently generated by TWST 90°. Figure 6.42 illustrates the variation in average C_P across all blade twist angles for the considered TSRs.

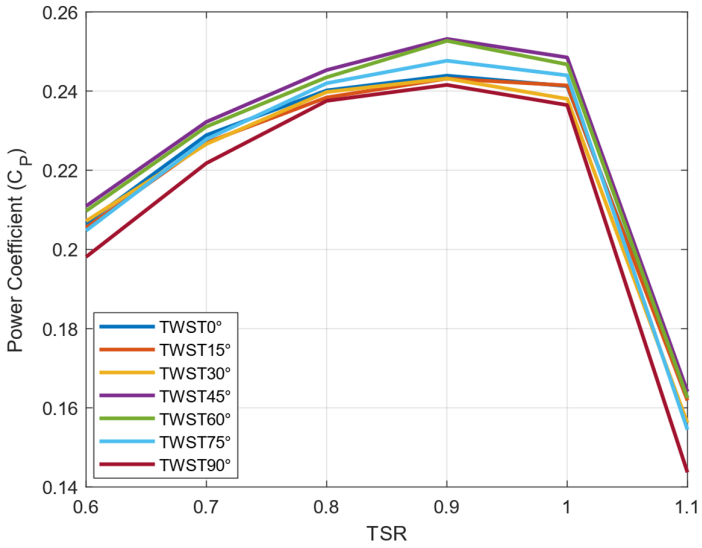


Figure 6.42. C_P vs. TSR curves of HSHT configurations

The peak C_{PS} are generated at a TSR of 0.9 by all studied helical configurations as shown in Figure 6.42. The maximum C_P is generated as 0.252 by TWST45° which is 3.81% higher than that of TWST0°. TWST45° also generates the highest C_{PS} at all TSRs among considered blade twist angles. Notably, TWST45° and TWST60° generates comparable C_{PS} for all TSRs especially for 0.9 TSR. The lowest C_{PS} are consistently generated by TWST90° at all TSRs. As illustrated in Figure 3, TWST0°, TWST15° and TWIST30° exhibit quite similar C_P values at all TSRs. Figure 6.43 shows the torque generation curves of turbines with different blade twist angles during a single rotation of each turbine at TSR 0.9 in terms of generated torque (N.m).

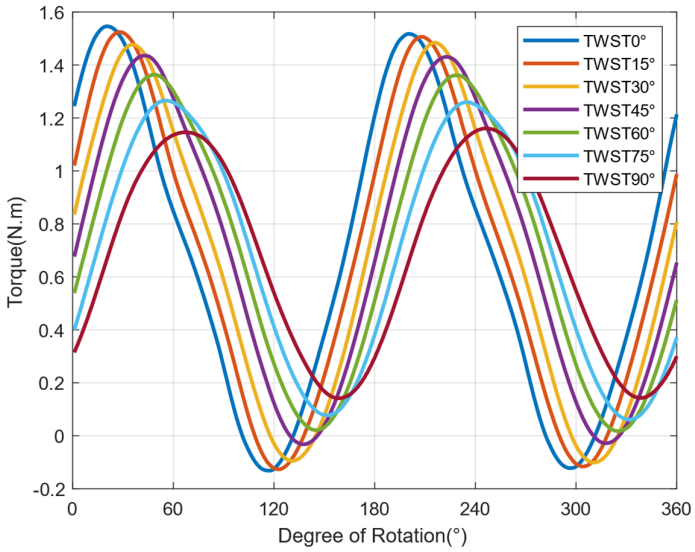


Figure 6.43. Torque generated by HSHT configurations over a single rotation

As shown in Figure 6.43, the oscillations observed on generated torque are significantly reduced. The standard deviation of TWST90°'s torque profile is 35.21% less compared to TWST0°. Although TWST45° achieved slightly better performance than TWST60°, TWST60° exhibits 7.28% less torque fluctuations compared to TWST45° as observed in Figure 4.

6.6.2 Evolution of the flow field around helical turbines

The twisted blade profiles in a helical SHT creates a continuous phase difference in the orientation of the blades along the length of the SHT. This continuous phase difference helps helical SHT distribute torque generation along the length of the blades. Therefore, the torque fluctuations are reduced as shown in Figure 6.43. To better understand this effect, the pressure contours around the blades of TWST0°, TWST45° and TWST90° are presented at 20° of rotation in Figure 6.44. Specifically, the pressure contours are presented at three different locations along the length of the turbines. These locations are shown in Figure 6.44 and named as Slice 1, Slice 2, and Slice 3.

TWST0° has straight blades; therefore, the azimuth angles of the blade cross-sections are constant at 20° along the turbine length as can be observed in Figure 6.44. On the other hand, the azimuth angles of the blade cross-sections in TWST45° and TWST90° continuously decrease due to applied blade twist as can be seen by comparing provided contours at slices in Figure 6.44. At 20° of rotation, the cross-section of blades in Slice 1 of TWST45° and TWST90 are slightly lower than 20° since Slice 1 is generated just ahead of the endplate where the blades cross-sections are at 20°.

As shown in Figure 6.44, the pressure over the concave side of TWST0°'s advancing blade is much higher than TWST45° and TWST90° at Slice 1 where the blade sections are at similar azimuth angles. At Slice 2 which presents the middle-sections of the turbines, the cross-sections presented for TWST0° and TWST45° are at significantly lower azimuth angles compared to cross-sections at Slice 1 due to phase shift. Therefore, the incoming water first impacts the convex side of the returning blades of TWST45° and TWST90°. As a result, the torque generation capacity of TWST45° and TWST90° is decreased. In contrast, the cross-section of TWST0° is exactly at 20°. The same observation can be also made for Slice 3, where the presented pressure contours are compared to each other, the high-pressure zones occur at the convex side of the returning blades of TWST45° and TWST90°. Therefore, the torque generation capacity of TWST45° and TWST90° is significantly reduced along lengths of the turbines.

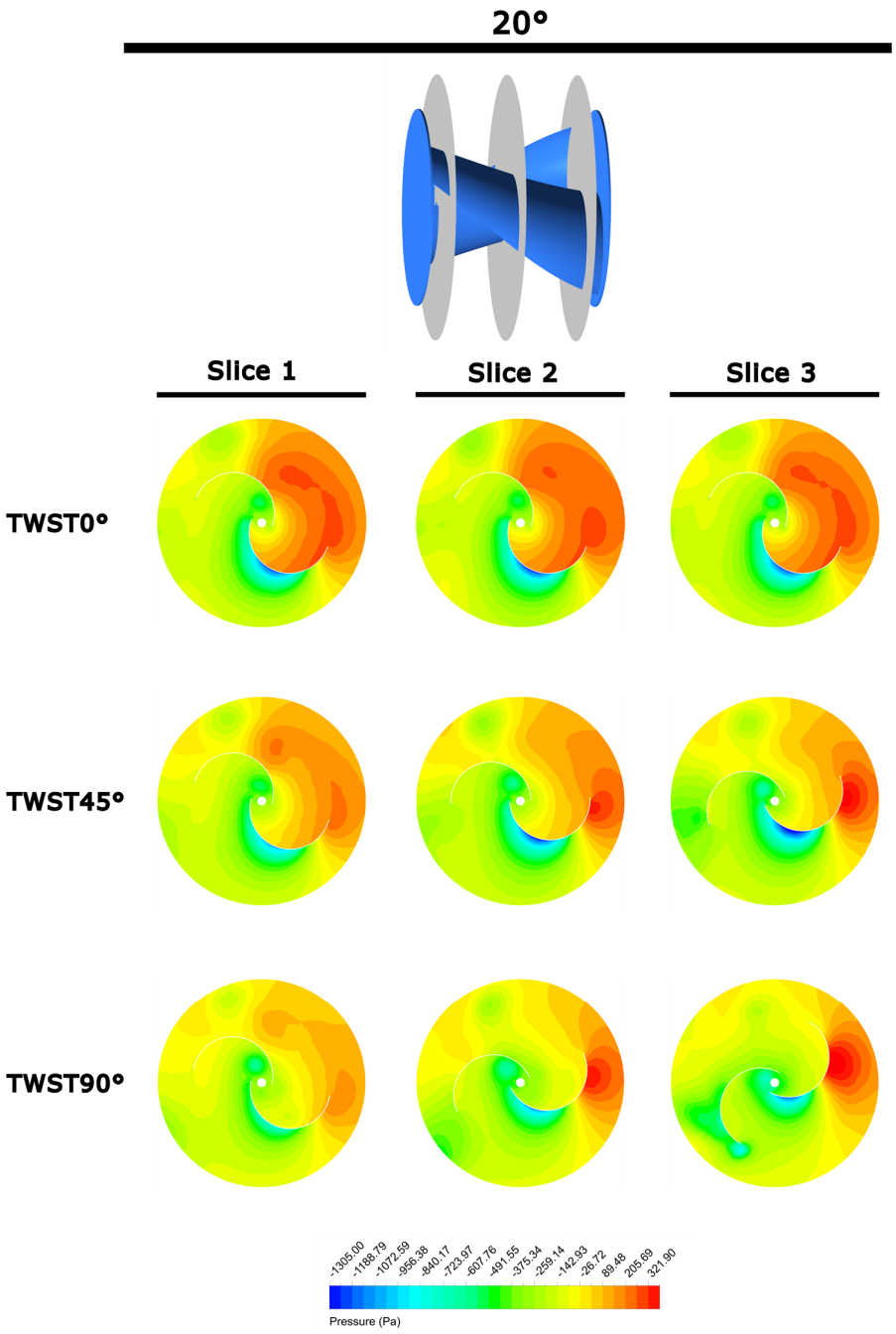


Figure 6.44. Pressure contours along the length of TWST0°, TWST45° and TWST90° at 20° of rotation

At 20°, the cross-section of standard SHT achieves maximum instantaneous torque generation as discussed many times in this thesis. Therefore, at 20°, TWST0° also achieves maximum instantaneous torque and higher torque value than TWST45° and TWST90°, as illustrated in Figure 6.43, since the blade sections of TWST0° are exactly at azimuth angle of 20° along the length of turbine. Moreover, at 20°, TWST45° exhibits a higher torque value compared to TWST90° as seen in Figure 6.43, due to lower phase difference angle than TWST90°. When the presented pressure contours of TWST45° and TWST90° at Slice 2 and Slice 3 are compared, it can be seen that the pressure on the convex side of the returning blade is higher for TWST90°. Therefore, TWST90° experiences greater negative torque compared to TWST45°. In Figure 6.45, the pressure contours of TWST0°, TWST45° and TWST90° are illustrated at 120° of rotation for same slice locations as Figure 6.44.

At 120° of rotation, the convex side of the returning blade is positioned in front of the advancing blade. Therefore, the incoming water flow first impacts the convex side of the returning blades and creates significant negative torque on the SHT. Also, the returning blade partially shields the advancing blade from the water flow at 120°. As a result, at 120°, a significant reduction in the torque generation capacity of the cross-section of SHT is occurs. As seen in Slice 1 in Figure 6.45, the presented pressure contours are very similar to each other even though the pressure on TWST45°'s returning blade is slightly higher than others. When the pressure contours at Slice 2 are compared to each other, the pressure over the concave side of the advancing blade increases with an increase in twist angle while the pressure on the convex side of the returning blades are similar. Consequently, at the middle of the turbines, TWST45° and TWST90°'s advancing blades generate higher positive torque compared to TWST0°. As can be observed in Figure 6.45, the cross-section of TWST90° presented at Slice 3 is around 30° due to 90° twist angle. Therefore, the advancing blade of TWST90° positioned in front of the returning blade. Consequently, the pressure on the advancing blade of TWST90° is much higher compared to TWST0°. Also, the pressure on the convex side of TWST90°'s

returning blade is significantly lower than TWST0°. Furthermore, the cross-section presented for TWST45° at Slice 3 is at an azimuth angle of 85° where standard SHT produces significantly higher torque compared to 110° of rotation. As a result of discussed observations, at 120° of rotation, TWST90° exhibits higher instantaneous torque than both TWST45° and TWST90° as illustrated in Figure 6.43. TWST45° also exhibits larger torque value than TWST0° at 120°.

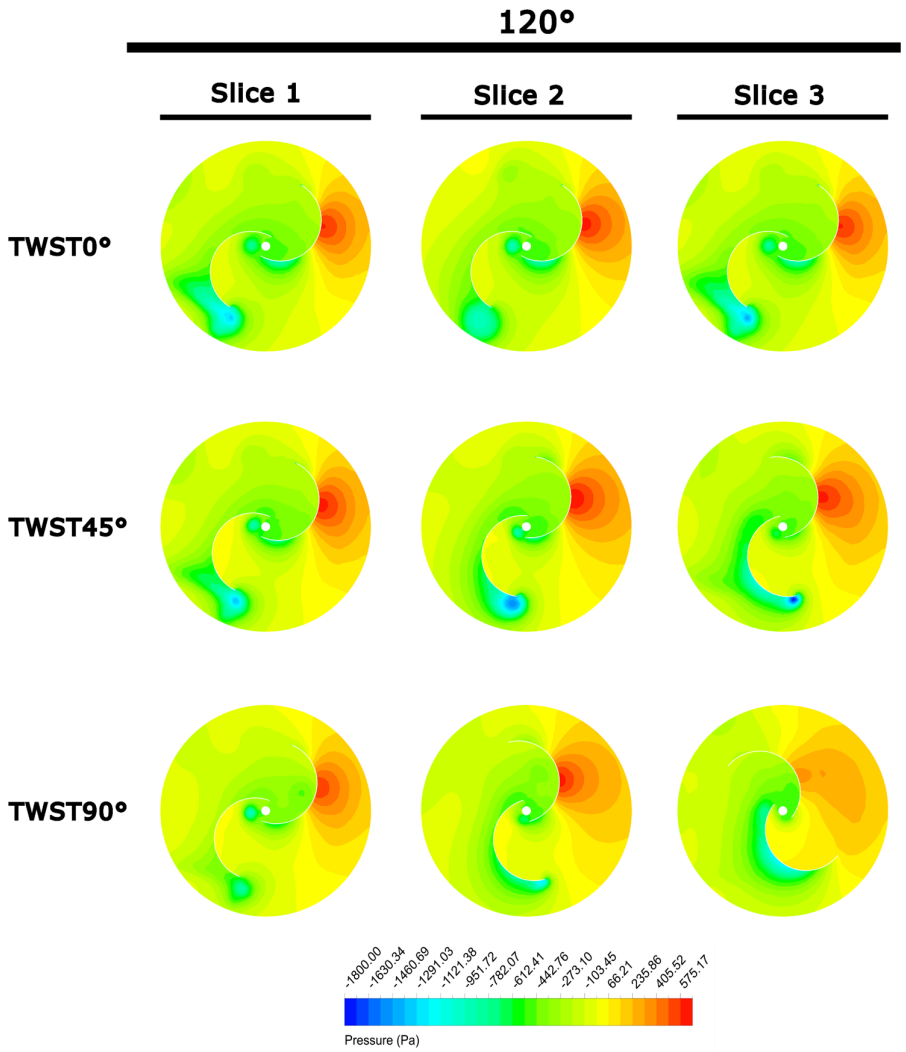


Figure 6.45. Pressure contours along the length of TWST0°, TWST45° and TWST90° at 120° of rotation

Figure 6.44 and Figure 6.45 show that along the turbine length the pressure distribution is almost uniform for the TWST0°. However, the introduction of the twisted blades significantly alters the pressure distribution over the blade profile along length of the turbine. In Figure 6.46, the pressure distributions over the blade profiles of TWST90°, TWST45° and TWST0° are presented at 90° of rotation.

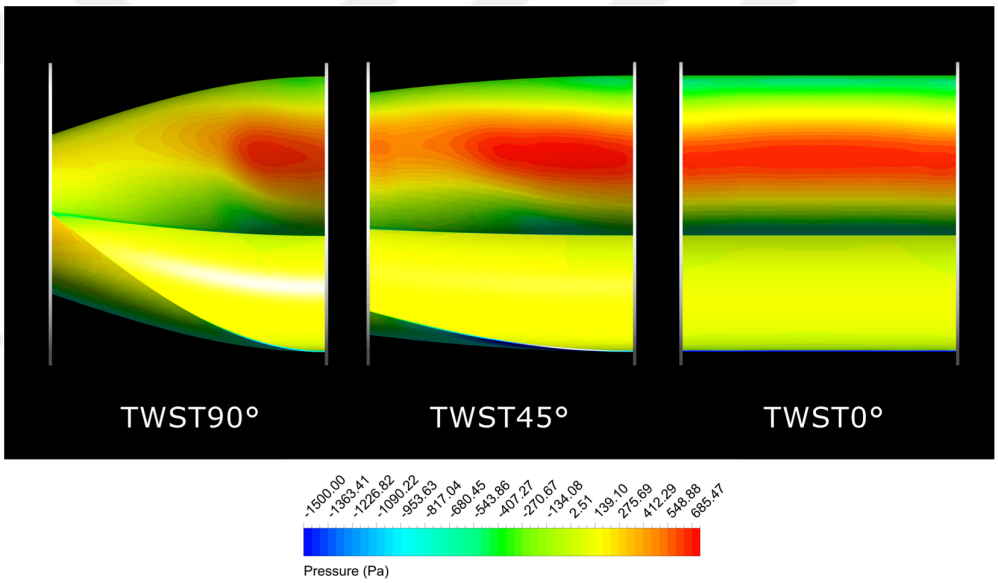


Figure 6.46. Pressure distribution over the blade surfaces of TWST0°, TWST45° and TWST90° at 90° of rotation

As shown in Figure 6.46, the pressure distribution on the blades of TWST0° is uniformly distributed. However, the pressure distributions on the blades of TWST90° and TWST45° gradually change along the length of the turbine. The regions closer to right endplates of TWST45° and TWST90° are at azimuth angles closer 90°; therefore, the pressure distribution is very similar to that of TWST0°. However, due to continuous change in azimuth angle along blade profile, the pressure distribution gradually changes and the pressure over the left side decreases.

To visualize the effect of gradually changing pressure distribution around the turbine blades on the velocity field over the blade profiles, the velocity vector distribution at just over the blade profiles is presented in Figure 6.47.

The uniform pressure distribution observed on TWST0°'s blades forces the incoming flow to more planar motion as seen in Figure 6.47 where the velocity vectors presented for TWST0° move perpendicularly to incoming velocity vector and parallel to blade surface. On the other hand, the velocity vectors of TWST45° and TWST90° show that some portion of the incoming water from the right side of the turbine, where high pressure occurs, is directed towards the left side of the turbine, where lower pressure zone is observed. Due to the gradual shift in pressure distribution, the incoming flow follows a swirling path along the blade profiles. As a result, some portion of the high energy incoming flow is redistributed towards the low-pressure zone which increases the utilization of the incoming flow and improves the efficiency.

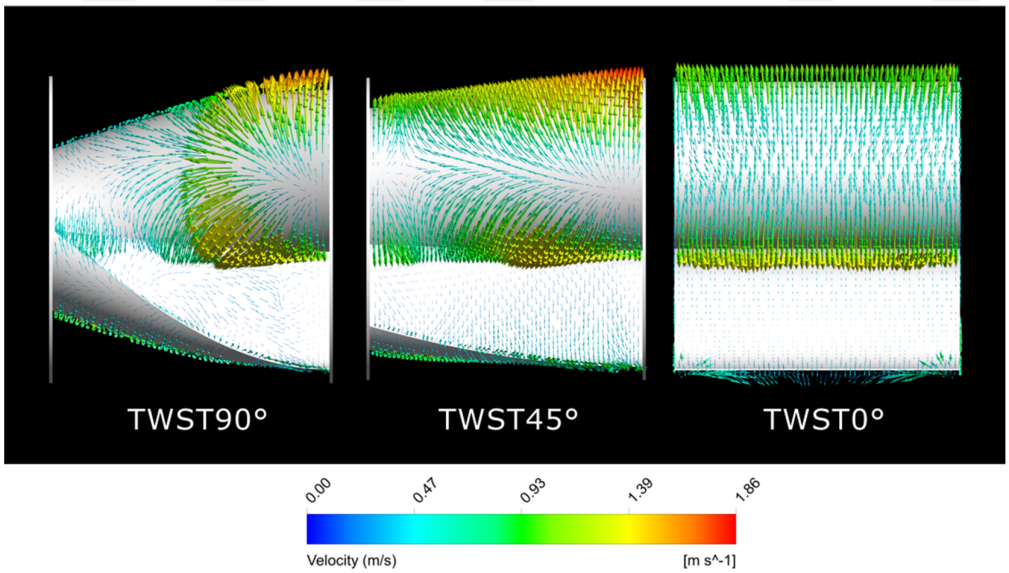


Figure 6.47. Velocity field over the blade surfaces of TWST0°, TWST45° and TWST90° at 90° of rotation

CHAPTER 7

CONCLUSION

In the scope of present thesis, the impact of several design modifications on the performance of the studied SHT are examined through CFD simulations. These design modifications includes the aspect ratio of the SHT, the multi-stage configurations of the studied SHT model and the adoptation of the helical blades in the SHT.

In the investigations of the effect of AR on the performance of the SHT, the performances of SHT models having ARs ranging from 1.0 to 1.9 are examined. The findings show that the performance of SHT is enhanced with the increasing AR. The SHT with an AR of 1.9 achieves the highest performance. However, the performance increase gained from the increasing AR significantly deteriorates beyond an AR of 1.6 for the studied SHT geometry. Specifically, the SHT having AR of 1.6 exhibits C_P of 0.274 at 0.9 TSR which is 0.72% and 0.36% higher than the SHTs having AR 1.7 and AR 1.8 respectively and 1.09% less than the SHT having AR of 1.9. Therefore, the AR of 1.6 is determined to be optimal AR of the studied SHT model by considering the additional stress on the mechanical components and the voltage regulation system resulting from increased AR.

For the multi-stage configurations, the ideal phase difference angle is investigated by simulating two- and three-stage configurations with different phase differences. For the two-stage arrangement, the study encompasses phase difference angles ranging from 15° to 90° in 15° increments, while for the three-stage arrangement, it includes angles ranging from 15° to 60° with 15° increments. The aspect ratio (AR) of the stages remains consistent at 0.95 for both two-stage and three-stage designs. Hence, the ARs of the two-stage and three-stage setups are 1.90 and 2.85, respectively. Among two-stage configurations, the two-stage SHT having 90° phase difference achieved the highest C_P of 0.288, marking a 3.78% improvement

compared to the single-stage turbine with an AR of 1.9. Moreover, the three-stage SHT having phase difference angle of 60° exhibited the highest C_P of 0.299 which is 2.75% higher than the single-stage SHT having AR of 2.85. Additionally, the findings show that the observed torque fluctuations are significantly reduced with the increasing phase difference. The top-performing two- and three-stage configurations experience 92.56% and 94.58% less torque fluctuations, respectively, compared to their single-stage counterparts with identical ARs.

In the exploration of helical blade adaptation in the SHT, the blade twist angles ranging from 0° to 90° are examined. Among these variations, the helical-bladed SHT with a blade twist angle of 45° attains the highest C_P of 0.252. This represents a notable performance improvement of 3.81% compared to the turbine equipped with classical semi-circular blades. Additionally, the findings highlight that as the blade twist angle increases, the observed torque fluctuations during the operation phase reduces. This implies that modifying the blade twist angle not only improves the turbine's average performance, but also enhances its stability in generating torque.

REFERENCES

Alexander, A. J., & Holownia, B. P. (1978). WIND TUNNEL TESTS ON A SAVONIUS ROTOB. In *Journal of Industrial Aerodynamics* (Vol. 3).

Alom, N., Saha, U. K., & Dewan, A. (2021). In the quest of an appropriate turbulence model for analyzing the aerodynamics of a conventional Savonius (S-type) wind rotor. *Journal of Renewable and Sustainable Energy*, *13*(2). https://doi.org/10.1063/5.0034362/926716

ANSYS. (2023). *Fluent Theory Guide*. https://ansyshelp.ansys.com/account/secured?returnurl=/Views/Secured/corp/v231/en/flu_th/flu_th.html

Avva, R. K., Smith, C. E., & Singhal, A. K. (1990). Comparative study of high and low reynolds number versions of k-ε models. *28th Aerospace Sciences Meeting, 1990*. https://doi.org/10.2514/6.1990-246

Badrul Salleh, M., Kamaruddin, N. M., & Mohamed-Kassim, Z. (2019). Savonius hydrokinetic turbines for a sustainable river-based energy extraction: A review of the technology and potential applications in Malaysia. *Sustainable Energy Technologies and Assessments*, *36*, 100554. https://doi.org/10.1016/J.SETA.2019.100554

Devlet Su İşleri Genel Müdürlüğü. (n.d.). Retrieved February 13, 2023, from https://www.dsi.gov.tr/Sayfa/Detay/754

Dobrev, I., & Massouh, F. (2011). CFD and PIV investigation of unsteady flow through Savonius wind turbine. *Energy Procedia*, *6*, 711–720. https://doi.org/10.1016/J.EGYPRO.2011.05.081

Douglas, C. A., Harrison, G. P., & Chick, J. P. (2008). Life cycle assessment of the Seagen marine current turbine. *Proceedings of the Institution of Mechanical Engineers Part M: Journal of Engineering for the Maritime Environment*, *222*(1), 1–12. https://doi.org/10.1243/14750902JEME94

Ferrari, G., Federici, D., Schito, P., Inzoli, F., & Mereu, R. (2017). CFD study of Savonius wind turbine: 3D model validation and parametric analysis. *Renewable Energy*, *105*, 722–734. https://doi.org/10.1016/J.RENENE.2016.12.077

Frikha, S., Driss, Z., Ayadi, E., Masmoudi, Z., & Abid, M. S. (2016). Numerical and experimental characterization of multi-stage Savonius rotors. *Energy*, *114*, 382–404. https://doi.org/10.1016/J.ENERGY.2016.08.017

Fujisawa, N. (1996). Velocity measurements and numerical calculations of flow fields in and around Savonius rotors. *Journal of Wind Engineering and Industrial Aerodynamics*, *59*(1), 39–50. https://doi.org/10.1016/0167-6105(94)00031-X

Fujisawa, N., & Gotoh, F. (1992). Visualization study of the flow in and around a Savonius rotor. *Experiments in Fluids*, *12*(6), 407–412. https://doi.org/10.1007/BF00193888/METRICS

Fundy. (2008). *The SeaGen tidal generator*. Creative Commons Attribution-Share Alike 3.0 Unported. https://commons.wikimedia.org/wiki/File:Seaflow_raised_16_jun_03.jpg

Golecha, K., Eldho, T. I., & Prabhu, S. V. (2011). Influence of the deflector plate on the performance of modified Savonius water turbine. *Applied Energy*, *88*(9), 3207–3217. https://doi.org/10.1016/j.apenergy.2011.03.025

Hadi, S., Sidiq, M., Cahyo Anindito, D., Prasetyo, A., Danardono, D., Prija Tjahjana, D., & Hadiani, R. (2019). Experimental Study of The Effects of Blade Twist on the Performance of Savonius Water Turbine in Water Pipe. *Journal of Advanced Research in Fluid Mechanics and Thermal Sciences Journal Homepage*, *57*, 202–207. www.akademiabaru.com/arfmts.html

Hayashi, T., Li, Y., & Hara, Y. (2005). Wind Tunnel Tests on a Different Phase Three-Stage Savonius Rotor. *JSME International Journal Series B Fluids and Thermal Engineering*, *48*(1), 9–16. https://doi.org/10.1299/JSMEB.48.9

Hydro Green Energy. (n.d.). Retrieved February 13, 2023, from https://hgenergy.com/projects#b73c4834-7e63-44be-8364-99179729c580

IEA. (2019). International Energy Agency. Africa Energy Outlook 2019. World Energy Outlook Special Report. *EA Publications*, 288. https://www.iea.org/reports/world-energy-outlook-2019/electricity#abstract

IPCC. (2014). Climate Change 2014. In *Climate Change 2014: Synthesis Report*. https://doi.org/10.1017/CBO9781107415324

IPCC. (2023). 2023: Summary for Policymakers. In: Climate Change 2023: Synthesis Report. Contribution of Working Groups I, II and III to the Sixth Assessment Report of the Intergovernmental Panel on Climate Change [Core Writing Team, H. Lee and J. Romero (eds.)]. *IPCC*, 1–34. https://doi.org/10.59327/IPCC/AR6-9789291691647.001

Jeong, W., & Seong, J. (2014). Comparison of effects on technical variances of computational fluid dynamics (CFD) software based on finite element and finite volume methods. *International Journal of Mechanical Sciences*, *78*, 19–26. https://doi.org/10.1016/J.IJMECSCI.2013.10.017

Kamoji, M. A., Kedare, S. B., & Prabhu, S. V. (2009a). Experimental investigations on single stage modified Savonius rotor. *Applied Energy*, *86*(7–8), 1064–1073. https://doi.org/10.1016/j.apenergy.2008.09.019

Kamoji, M. A., Kedare, S. B., & Prabhu, S. V. (2009b). Performance tests on helical Savonius rotors. *Renewable Energy*, *34*(3), 521–529. https://doi.org/10.1016/j.renene.2008.06.002

Kerikous, E., & Thévenin, D. (2020). Performance Enhancement of a Hydraulic Savonius Turbine by Optimizing Overlap and Gap Ratios. *ASME 2019 Gas Turbine India Conference, GTINDIA 2019*, *2*. https://doi.org/10.1115/GTINDIA2019-2670

Kougias, I., Aggidis, G., Avellan, F., Deniz, S., Lundin, U., Moro, A., Muntean, S., Novara, D., Pérez-Díaz, J. I., Quaranta, E., Schild, P., & Theodossiou, N. (2019). Analysis of emerging technologies in the hydropower sector. In *Renewable and*

Sustainable Energy Reviews (Vol. 113). Elsevier Ltd. https://doi.org/10.1016/j.rser.2019.109257

Kumar, A., & Saini, R. P. (2016a). Numerical Investigations on Single Stage and Multi-Stage Twisted Savonius Hydrokinetic Turbine. *In Proceedings of the 6th International and 43rd National Conference on Fluid Mechanics and Fluid Power.* Allahabad., https://www.researchgate.net/publication/311734591

Kumar, A., & Saini, R. P. (2016b). Numerical investigation and novel designing of multi-stage savonius rotor for harnessing hydro power. *12th IEEE International Conference Electronics, Energy, Environment, Communication, Computer, Control: (E3-C3), INDICON 2015*. https://doi.org/10.1109/INDICON.2015.7443835

Kumar, A., & Saini, R. P. (2016c). Performance parameters of Savonius type hydrokinetic turbine – A Review. *Renewable and Sustainable Energy Reviews*, *64*, 289–310. https://doi.org/10.1016/J.RSER.2016.06.005

Kumar, A., & Saini, R. P. (2017a). Performance analysis of a Savonius hydrokinetic turbine having twisted blades. *Renewable Energy*, *108*, 502–522. https://doi.org/10.1016/j.renene.2017.03.006

Kumar, A., & Saini, R. P. (2017b). Performance analysis of a single stage modified Savonius hydrokinetic turbine having twisted blades. *Renewable Energy*, *113*, 461–478. https://doi.org/10.1016/j.renene.2017.06.020

Kumar, A., Saini, R. P., Saini, G., & Dwivedi, G. (2020). Effect of number of stages on the performance characteristics of modified Savonius hydrokinetic turbine. *Ocean Engineering*, *217*. https://doi.org/10.1016/j.oceaneng.2020.108090

Mabrouki, I., Driss, Z., & Abid, M. S. (2014). Experimental Investigation of the Height Effect of Water Savonius Rotors. *International Journal of Mechanics and Applications*, *4*(1), 8–12. https://doi.org/10.5923/j.mechanics.20140401.02

Mahesa Prabowoputra, D., Hadi, S., Sohn, J. M., & Prabowo, A. R. (2020). The effect of multi-stage modification on the performance of Savonius water turbines under the horizontal axis condition. *Open Engineering*, *10*(1), 793–803. https://doi.org/10.1515/eng-2020-0085

Mahmoud, N. H., El-Haroun, A. A., Wahba, E., & Nasef, M. H. (2012). An experimental study on improvement of Savonius rotor performance. *Alexandria Engineering Journal*, *51*(1), 19–25. https://doi.org/10.1016/j.aej.2012.07.003

Maldar, N. R., Ng, C. Y., & Oguz, E. (2020). A review of the optimization studies for Savonius turbine considering hydrokinetic applications. *Energy Conversion and Management*, *226*, 113495. https://doi.org/10.1016/J.ENCONMAN.2020.113495

Maldar, N. R., Ng, C. Y., Patel, M. S., & Oguz, E. (2022). Potential and prospects of hydrokinetic energy in Malaysia: A review. *Sustainable Energy Technologies and Assessments*, *52*, 102265. https://doi.org/10.1016/J.SETA.2022.102265

Menter, F. R. (1992). *Improved two-equation k-omega turbulence models for aerodynamic flows*.

Menter, F. R. (1994). Two-equation eddy-viscosity turbulence models for engineering applications. *AIAA Journal*, *32*(8), 1598–1605. https://doi.org/10.2514/3.12149

Modi, V. J., & Fernando, M. S. U. K. (1989). On the performance of the savonius wind turbine. *Journal of Solar Energy Engineering, Transactions of the ASME*, *111*(1), 71–81. https://doi.org/10.1115/1.3268289

Mosbahi, M., Ayadi, A., Chouaibi, Y., Driss, Z., & Tucciarelli, T. (2019). Performance study of a Helical Savonius hydrokinetic turbine with a new deflector system design. *Energy Conversion and Management*, *194*, 55–74. https://doi.org/10.1016/J.ENCONMAN.2019.04.080

Mosbahi, M., Elgasri, S., Lajnef, M., Mosbahi, B., & Driss, Z. (2021). Performance enhancement of a twisted Savonius hydrokinetic turbine with an upstream deflector. *International Journal of Green Energy*, *18*(1), 51–65. https://doi.org/10.1080/15435075.2020.1825444

Murai, Y., Nakada, T., Suzuki, T., & Yamamoto, F. (2007). Particle tracking velocimetry applied to estimate the pressure field around a Savonius turbine. *Measurement Science and Technology*, *18*(8), 2491. https://doi.org/10.1088/0957-0233/18/8/026

Nag, A. K., & Sarkar, S. (2020). Experimental and numerical study on the performance and flow pattern of different Savonius hydrokinetic turbines with varying duct angle. *Journal of Ocean Engineering and Marine Energy*, *6*(1), 31–53. https://doi.org/10.1007/s40722-019-00155-6

NAKAJIMA, M., IIO, S., & IKEDA, T. (2008). Performance of Double-step Savonius Rotor for Environmentally Friendly Hydraulic Turbine. *Journal of Fluid Science and Technology*, *3*(3), 410–419. https://doi.org/10.1299/jfst.3.410

Nasef, M. H., El-Askary, W. A., AbdEL-hamid, A. A., & Gad, H. E. (2013). Evaluation of Savonius rotor performance: Static and dynamic studies. *Journal of Wind Engineering and Industrial Aerodynamics*, *123*, 1–11. https://doi.org/10.1016/J.JWEIA.2013.09.009

Patel, V., Bhat, G., Eldho, T. I., & Prabhu, S. V. (2017). Influence of overlap ratio and aspect ratio on the performance of Savonius hydrokinetic turbine. *International Journal of Energy Research*, *41*(6), 829–844. https://doi.org/10.1002/er.3670

POWERMAG. (2009). *Hydrokinetic Plant Piggybacks on Existing Hydro Plant*. https://www.powermag.com/hydrokinetic-plant-piggybacks-on-existing-hydro-plant/

Prabowoputra, D. M., Prabowo, A. R., Hadi, S., & Sohn, J. M. (2021). Assessment of turbine stages and blade numbers on modified 3D Savonius hydrokinetic turbine performance using CFD analysis. *Multidiscipline Modeling in Materials and Structures*, *17*(1), 253–272. https://doi.org/10.1108/MMMS-12-2019-0224

Products | Waterotor Energy Technologies. (n.d.). Retrieved March 16, 2023, from https://waterotor.com/products/

Rahimian, M., Walker, J., & Penesis, I. (2018). Performance of a horizontal axis marine current turbine– A comprehensive evaluation using experimental, numerical, and theoretical approaches. *Energy*, *148*, 965–976. https://doi.org/10.1016/j.energy.2018.02.007

Ridgill, M., Lewis, M. J., Robins, P. E., Patil, S. D., & Neill, S. P. (2022). Hydrokinetic energy conversion: A global riverine perspective. *Journal of Renewable and Sustainable Energy*, *14*(4). https://doi.org/10.1063/5.0092215

Ridgill, M., Neill, S. P., Lewis, M. J., Robins, P. E., & Patil, S. D. (2021). Global riverine theoretical hydrokinetic resource assessment. *Renewable Energy*, *174*, 654–665. https://doi.org/10.1016/J.RENENE.2021.04.109

Roy, S., & Saha, U. K. (2013a). *INVESTIGATIONS ON THE EFFECT OF ASPECT RATIO INTO THE PERFORMANCE OF SAVONIUS ROTORS*. http://www.asme.org/about-asme/terms-of-use

Roy, S., & Saha, U. K. (2013b). Review on the numerical investigations into the design and development of Savonius wind rotors. *Renewable and Sustainable Energy Reviews*, *24*, 73–83. https://doi.org/10.1016/J.RSER.2013.03.060

Saad, A. S., Elwardany, A., El-Sharkawy, I. I., Ookawara, S., & Ahmed, M. (2021). Performance evaluation of a novel vertical axis wind turbine using twisted blades in multi-stage Savonius rotors. *Energy Conversion and Management*, *235*, 114013. https://doi.org/10.1016/J.ENCONMAN.2021.114013

Saad, A. S., Ookawara, S., & Ahmed, M. (2022). Influence of Varying the Stage Aspect Ratio on the Performance of Multi-Stage Savonius Wind Rotors. *Journal of Energy Resources Technology, Transactions of the ASME*, *144*(1). https://doi.org/10.1115/1.4050876

Şahin, Ü. A., Onat, B., & Ayvaz, C. (2019). *Climate Change and Greenhouse Gases in Turkey* (pp. 201–214). https://doi.org/10.1007/978-3-319-95888-0_17

Savonius, Helsingfors, & Finland. (1931). The S-Rotor and Its Applications. *Mechanical Engineering*, *53*(5), 335–338.

Shigetomi, A., Murai, Y., Tasaka, Y., & Takeda, Y. (2011). Interactive flow field around two Savonius turbines. *Renewable Energy*, *36*(2), 536–545. https://doi.org/10.1016/J.RENENE.2010.06.036

Simav, Ö., & Şeker, D. Z. (2013). *KIYI ETKİLENEBİLİRLİK GÖSTERGESİ İLE TÜRKİYE KIYILARI RİSK ALANLARININ TESPİTİ*.

Subhra Mukherji, S., Kolekar, N., Banerjee, A., & Mishra, R. (2011). Numerical investigation and evaluation of optimum hydrodynamic performance of a horizontal axis hydrokinetic turbine. *Journal of Renewable and Sustainable Energy*, *3*(6), 063105. https://doi.org/10.1063/1.3662100

Talukdar, P. K., Sardar, A., Kulkarni, V., & Saha, U. K. (2018). Parametric analysis of model Savonius hydrokinetic turbines through experimental and computational investigations. *Energy Conversion and Management*, *158*, 36–49. https://doi.org/10.1016/j.enconman.2017.12.011

T.C. Enerji ve Tabii Kaynaklar Bakanlığı. (2023). *Elektrik Enerjisi*. https://enerji.gov.tr/bilgi-merkezi-enerji-elektrik

Thiyagaraj, J., Rahamathullah, I., & Prabu, P. S. (2016). Experimental investigations on the performance characteristics of a modified four bladed Savonius hydro-kinetic turbine. *International Journal of Renewable Energy Research*, *6*(4), 1530–1536. https://doi.org/10.20508/IJRER.V6I4.4798.G6943

Torres, S., Marulanda, A., Montoya, M. F., & Hernandez, C. (2022). Geometric design optimization of a Savonius wind turbine. *Energy Conversion and Management*, *262*. https://doi.org/10.1016/j.enconman.2022.115679

TUİK. (2023, March 29). *Sera Gazı Emisyon İstatistikleri, 1990-2021*. https://data.tuik.gov.tr/Bulten/Index?p=Sera-Gazi-Emisyon-Istatistikleri-1990-2021-49672

U.S Department of Energy. (2015). Quadrennial Technology Review 2015 - Marine and Hydrokinetic Power - Chapter 4: Technology Assessments. *Quadrennial Technology Review 2015* . https://www.energy.gov/sites/prod/files/2015/12/f27/QTR2015-4N-Marine-and-Hydrokinetic-Power.pdf

Vermaak, H. J., Kusakana, K., & Koko, S. P. (2014). Status of micro-hydrokinetic river technology in rural applications: A review of literature. *Renewable and Sustainable Energy Reviews*, *29*, 625–633. https://doi.org/10.1016/J.RSER.2013.08.066

Yaakob, O., Suprayogi, D., Abdul Ghani, M., & Tawi, K. (2013). Experimental Studies on Savonius-type Vertical Axis Turbine for Low Marine Current Velocity. *International Journal of Engineering*, *26*(1), 91–98. https://doi.org/10.5829/idosi.ije.2013.26.01a.12

Yaakob, O., Tawi, K., & Sunanto, D. T. (2010). Computer Simulation Studies on the Effect Overlap Ratio for Savonius Type Vertical Axis Marine Current Turbine. *International Journal of Engineering*, *23*(1), 79–88. https://www.ije.ir/article_71836.html

Yadav, P. K., Kumar, A., & Jaiswal, S. (2023). A critical review of technologies for harnessing the power from flowing water using a hydrokinetic turbine to fulfill the energy need. *Energy Reports*, *9*, 2102–2117. https://doi.org/10.1016/J.EGYR.2023.01.033

Yao, J., Li, F., Chen, J., Yuan, Z., & Mai, W. (2019). Parameter Analysis of Savonius Hydraulic Turbine Considering the Effect of Reducing Flow Velocity. *Energies 2020, Vol. 13, Page 24*, *13*(1), 24. https://doi.org/10.3390/EN13010024

Yuce, M. I., & Muratoglu, A. (2015). Hydrokinetic energy conversion systems: A technology status review. *Renewable and Sustainable Energy Reviews*, *43*, 72–82. https://doi.org/10.1016/J.RSER.2014.10.037

Zhou, Z., Benbouzid, M., Charpentier, J. F., Scuiller, F., & Tang, T. (2017). Developments in large marine current turbine technologies – A review. *Renewable and Sustainable Energy Reviews*, *71*, 852–858. https://doi.org/10.1016/J.RSER.2016.12.113

Zullah, M. A., Prasad, D., Choi, Y. Do, & Lee, Y. H. (2010). Study on the performance of helical savonius rotor for wave energy conversion. *AIP Conference Proceedings*, *1225*, 641–649. https://doi.org/10.1063/1.3464913